A Study of Morphing Wing Effectiveness in Fighter Aircraft using Exergy Analysis and Global Optimization Techniques

Jeffrey Robert Butt

Thesis submitted to the Faculty of the
Virginia Polytechnic Institute and State University
in partial fulfillment of the requirements for the degree of

Master of Science
In
Mechanical Engineering

Dr. Michael von Spakovsky, Chair
Dr. Harry Robertshaw
Dr. Walter O'Brien
Dr. David Moorhouse

December 9, 2005
Blacksburg, Virginia

Keywords: exergy, morphing wing, optimization

A Study of Morphing Wing Effectiveness in Fighter Aircraft using Exergy Analysis and Global Optimization Techniques

by Jeffrey Robert Butt

Abstract

This thesis work presents detailed results of the application of energy- and exergy-based methods to the integrated synthesis/design of an Air-to-Air Fighter (AAF) aircraft with and without wing-morphing capability. In particular, a morphing-wing AAF is compared to a traditional fixed-wing AAF by applying large-scale optimization using exergy- and energy-based objective functions to the synthesis/design and operation of the AAF which consists of an Airframe Subsystem (AFS-A) and Propulsion Subsystem (PS). A number of key synthesis/design and operational decision variables are identified which govern the performance of the AFS-A and PS during flight, and detailed models of the components of each of the subsystems are developed. Rates of exergy destruction and exergy loss resulting from irreversible loss mechanisms are determined in each of the AAF vehicle subsystems and their respective components.

Multiple optimizations are performed on both types of AAF for a typical fighter aircraft mission consisting of 22 segments. Four different objective functions are used in order to compare exergy-based performance measures to the more traditional energy-based ones. The results show that the morphing-wing AAF syntheses/designs outperform those for the fixed-wing aircraft in terms of exergy destroyed/lost and fuel consumed. These results also show that the exergy-based objectives not only produce the "best" of the optimal syntheses/designs for both types of AAF in terms of exergy destroyed/lost and fuel consumed but as well provide details of where in each subsystem/component and how much specifically each source of irreversibility contributes to the optimal syntheses/designs found. This is not directly possible with an energy-based approach.

Finally, after completion of the synthesis/design optimizations, a parametric study is performed to explore the effect on morphing-wing effectiveness of changing the weight and energy penalties used to model the actuations required for morphing. The results show that the morphing-wing AAF exhibits significant benefits over the fixed-wing aircraft even for unrealistic weight and energy penalties.

Acknowledgements

This thesis is the product of much hard work and dedication by many people. I would like to thank my advisor Dr. Michael von Spakovsky for presenting me with the opportunity to perform this research, for his confidence in my abilities, and for his acceptance of the decisions that were made with respect to this research. Secondly, I'd like to thank Dr. Walter O'Brien, Dr. Harry Robertshaw, and Dr. David Moorhouse for serving on my committee, for the input that they provided throughout the duration of my research, and for taking the time to review and provide input on my thesis draft.

This work was conducted under the sponsorship of the Air Force Research Laboratories (AFRL) during two summer internships at the Wright Patterson Air Force Base in Dayton, OH. I would like to thank Dr. David Moorhouse, Dr. Jose Camberos and many others at the AFRL for their valuable help and guidance on this project. I would also like to show my appreciation to Kyle Markell and Keith Brewer for their advice and suggestions as I began my thesis research.

I am also grateful for the MooLENI optimization software that was provided by the Laboratory of Industrial Energy Systems (LENI) at Ecole Polytechnique Federale de Lausanne (EPFL).

I thank the Department of Education for providing the loans necessary for me to go to graduate school.

I would like to show my appreciation to all my friends in Blacksburg and around the country who always managed to keep my spirits high when the pressures of graduate school got me down. I would also like to show my gratitude for my girlfriend Ginalyn for her support, for keeping me focused, and for bringing me food and coffee as I diligently worked on my thesis on the nights and weekends around my full time work schedule.

Finally, I'd like to thank my parents, Robert and Genevieve Butt, for encouraging my decision to further my education. Without their constant support, both financially and emotionally, none of this would have been possible.

Jeffrey Robert Butt

Table of Contents

List of Figures

List of Tables

Nomenclature

a	Speed of sound	K_1	Induced Drag Factor
AAF	Air-to-Air Fighter	K_{dw}	Delta Wing Factor
$AFS\text{-}A$	Airframe Subsystem-Aerodynamics	K_{vs}	Wing Sweep Factor
AR	Aspect Ratio	L	Lift, Fuselage Length
BCA	Best Cruise Altitude	$\dot{m}$	Mass Flow Rate
BCM	Best Cruise Mach Number	M	Mach Number
C_L	Lift Coefficient	mil	Military
$C_{L\alpha}$	Slope of the List Curve	N	Number of Turns
C_D	Drag Coefficient	N_z	Ultimate Load Factor
C_{Do}	Parasitic Drag Coefficient	n	Load Factor
C_{Di}	Induced Drag Coefficient	$PPAY$	Permanent Payload
C_{Dwave}	Wave Drag Coefficient	PR	Pressure Ratio
D	Drag, Fuselage Diameter	PS	Propulsion Subsystem
Ex	Exergy	q	Dynamic Pressure
$EPAY$	Expendable Payload	$\dot{Q}$	Heat Transfer Rate
f	Fuel-to-Air Ratio	Re	Reynolds Number
F_N	Normal Force	RFP	Request for Proposal
g	Acceleration due to Gravity	S	Wing Planform Area
G	Vector of Inequality Constraints	SL	Sea Level
h	Altitude	SFC	Specific Fuel Consumption
H	Vector of Equality Constraints	S_{csw}	Control Surface Area

$S_{exposed}$	Exposed Wing Area
t	Time
T	Thrust
T_{SL}	Sea-Level Installed Thrust
t/c	Thickness-to-Chord Ratio
$TSFC$	Thrust Specific Fuel Consumption
V	Velocity
W	Weight, Fuselage Width
W_E	Empty Weight
W_{TO}	Gross Take-off Weight

Greek

α	Angle of Attack
β	Weight Fraction
θ	Temperature Ratio
γ	Ratio of Specific Heats
λ	Taper Ratio
Λ_{LE}	Leading Edge Sweep Angle
$\Lambda_{1/4}$	Quarter Chord Sweep Angle
Λ	Wing Sweep Angle
Π	Weight Ratio
π	Turbine Pressure Ratio

Subscripts

f	Fuel, Final
i	Initial
o	Reference Value
0	Ambient Value
ref	Reference
$comp$	Compressor
$TURB$	Turbine
$COMB$	Combustor
aft	afterburner
t	Tip
r	Root

Chapter 1

Introduction

A collection of new technologies are being developed that may allow aircraft to readily change their shape during flight. The recent advances in adaptive structures and smart materials have created much interest in aircraft applications of these technologies. In particular, one of the areas of high interest of these applications is a "morphing wing" aircraft, which would be able to change its wing shape over multiple, dissimilar flight segments. Allowing the wing to change its geometry and shape over different mission segments could maximize the efficiency and performance of that aircraft over the entire mission considered. Therefore, it is important to investigate the possible advantages that an aircraft with a morphing wing could gain over a conventional fixed wing aircraft.

The main focus of this thesis work is to examine the benefits of allowing the geometry of an aircraft's wing to change during flight while taking into account other aircraft subsystem interactions. The term "Morphing wing" generally describes an aircraft wing or structure that can change size and shape during flight to enable the aircraft to drastically change its standard performance or characteristics. For aircraft, performance usually implies cost (energy or monetary), weight, and maneuverability. Classic aircraft wings have a fixed geometry and are designed to suit all mission segments, but do not achieve a favorable airframe configuration for any of the individual mission segments. With morphing wing technology it may be possible to overcome this less than optimal design by allowing the wing to "morph" from one configuration to another during a mission to achieve the best overall configurations for each flight segment. Of course, wing morphing comes with penalties that must be taken into account. There will be added weight and energy consumption by the overall aircraft system due to the addition of actuators that are used to physically morph the wing. So naturally, one of the objectives of this research is to determine if and to what extent the improved aerodynamics created by wing morphing offsets the associated penalties.

The morphing aircraft models used in this research were designed/developed following the synthesis/design analysis of Raymer (1999) and Rancruel (2003) and are comprised of two different subsystems, i.e. a propulsion subsystem (PS) and an airframe subsystem-aerodynamics (AFS-A). Two different aircraft models were created for this analysis; the first is of a traditional, fixed-wing aircraft that is to be used as a baseline case, and the second is of a morphing wing aircraft that allows the wings to change shape during flight within a set of geometric constraints. These two models are identical in every way (fuselage, fixed parameters, basic weights, etc.) except that the morphing model is allowed to change shape and contains weight and fuel penalties to account for the actuator and actuation needed for the morphing. Due to the complexities, interrelations, and nonlinearities of these subsystems, it is useful to evaluate these systems using large-scale system optimization. The objective functions or figures of merit that are used for this optimization problem are based on exergy, energy, and fuel weight. The effects which each has on the final aircraft synthesis/design and operation is examined.

1.1 General Background/History of Morphing Aircraft

1.1.1 Morphing Technology: Past-to-Present

From a biological point of view, birds are a natural example of wing morphing at work. It would be negligent for scientists and engineers to overlook birds for motivations on morphing wing designs (Bowman, Sanders and Weisshaar, 2002). Birds are able to fold, sweep, twist, and change the cross-section of their wings during flight. The aspect of particular interest with regards to these wing mechanisms is that they are highly integrated in terms of structure and function. For example, a bird's wing is able to lift and propel while providing the necessary forces and moments to trim (i.e. balance). Different configurations that birds use for different flight conditions are shown in Figure 1.1. This figure shows that the bald eagle extends his wings to maximize his wing span and wing area. This configuration minimizes the amount of effort required (i.e. power) to soar at low speeds (i.e. loiter). Conversely, the bald eagle tucks his wing to minimize his wing span and wing area in order to reduce drag. This configuration allows for higher speed flight (i.e. dash).

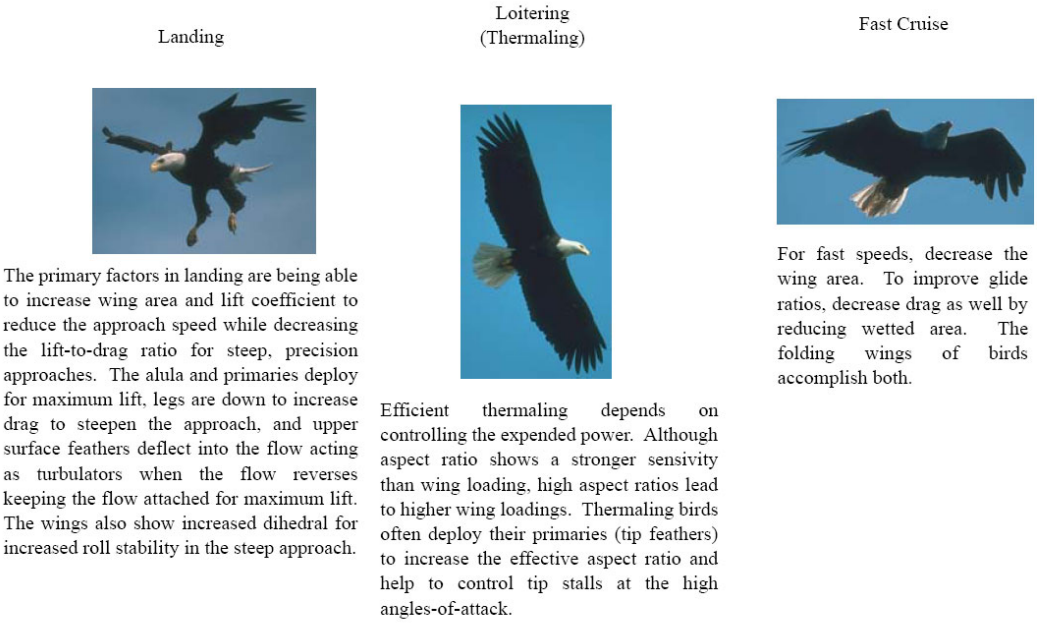

Figure 1.1: Summary of bird flight conditions and geometry changes (Bowman, Sanders, and Weisshaar, 2002).

The concept of changing the geometry or shape of an aircraft's wing or other components during flight has been around since the beginning of controlled flight (Moorhouse et al., 2005; Bowman, Sanders, and Weisshaar, 2002). The Wright brothers used wing twisting techniques for roll control when flight was in its infancy. Other early morphing technologies included retractable landing gears for reduced drag and foldable wings for increased transportability. Trailing edge flaps and fowler flaps have been used to change the wing camber and area during flight, typically at low speed segments such as takeoff and landing, thrust vectoring has also provided benefits during takeoff and landing segments, in addition to increasing an aircraft's maneuverability. Variable sweep angle wings have also been used on a number of aircraft configurations to account for the optimal geometry contrasts between subsonic and supersonic flight conditions. A timeline of when different morphing capabilities were introduced is presented in Figure 1.2.

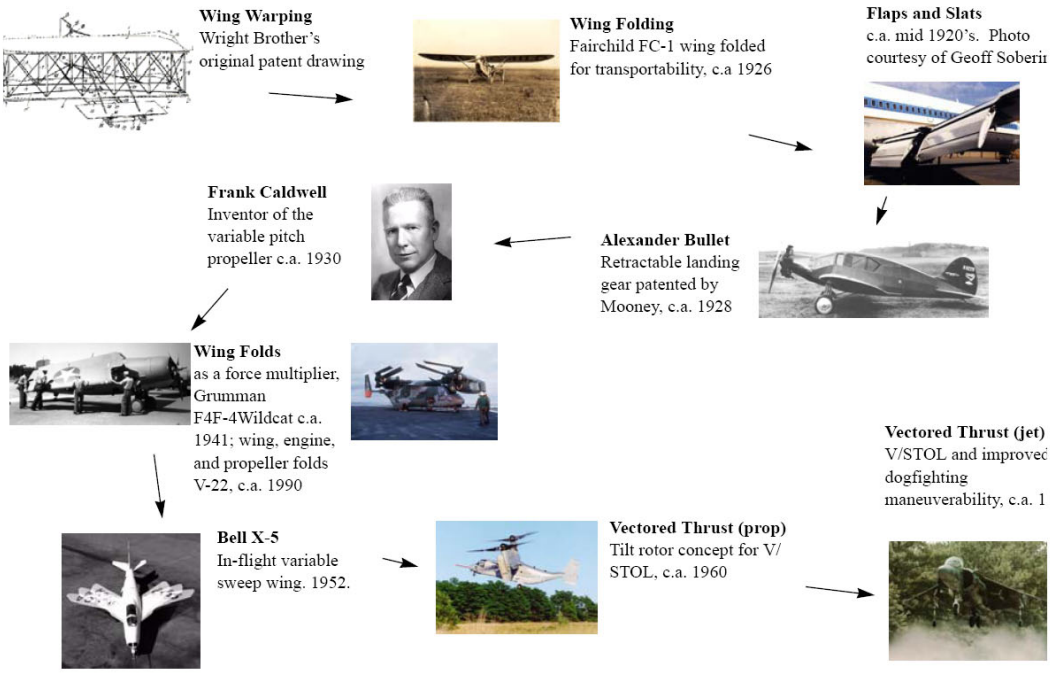

Figure 1.2: History of aircraft morphing technologies (Bowman, Sanders, and Weisshaar, 2002).

1.1.2 The Future of Morphing Technology

Currently, several research programs are underway to further understand the potential for morphing wing technologies such as hinge-less control surfaces, variable wing twist, and seamless variable camber. These new technologies could provide drastic changes in an aircraft wing's shape and size, which could produce an abundance of different performance benefits. The scope of all of the possible advantages that a morphing wing could provide has yet to be truly realized. NASA's Aircraft Morphing Program and DARPA's Morphing Aircraft Structures program are currently engaged in large-scale coordinated efforts for the development of morphing wing aircraft (Roth and Crossley, 2003).

One of the more interesting examples to come out of the DARPA Morphing Aircraft Structures Program is the Lockheed Unmanned Air Vehicle (UAV) with in-flight wing folding capability. The main performance improvements that morphing provides this aircraft come from its variable wing area, wetted area, and aspect ratio, which allow efficient operation at both high and low speeds and altitudes. The Lockheed UAV

folding wing concept combines desirable attributes from several different types of aircraft platforms, as shown in Figure 1.3. This new design combines the aircraft services of reconnaissance, loiter, attack, and stealth (i.e. low observability). The combination of these attributes allows the Lockheed UAV to perform a hunter-killer mission (i.e. to search and destroy a specified target). Generally a "package" or group of aircraft with different functions is required to perform this type of mission, but the Lockheed UAV concept can conduct this type of mission solo. This in turn reduces the amount of aircraft, ground support, and overall cost required to perform such a mission.

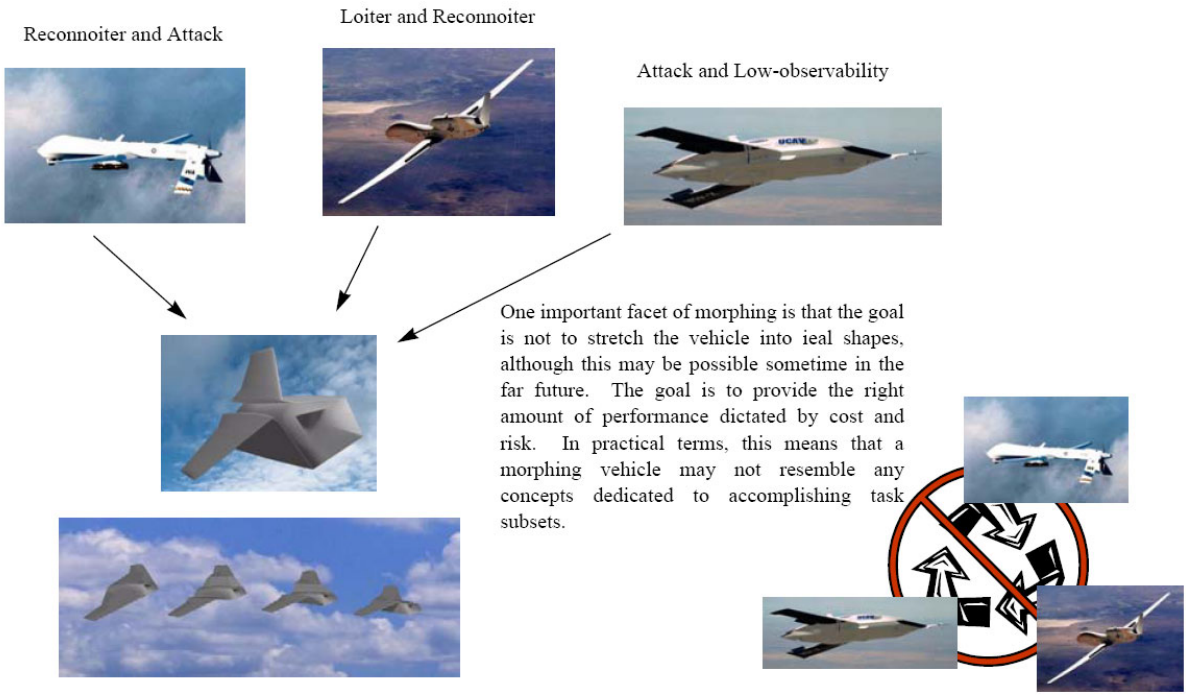

Figure 1.3: DARPA morphing aircraft structures Lockheed hunter-killer aircraft concept (Bowman, Sanders, and Weisshaar, 2002).

1.2 Aircraft Synthesis/Design Approach

The synthesis/design of an aircraft system is based on the requirements of the consumer, the development of new or future concepts, and the capability of the subsystems present in the aircraft system. According to Raymer (1999) and Rancruel

(2002) the synthesis/design process should be divided into three design phases, specifically, conceptual synthesis, preliminary synthesis/design, and detailed design. These three design phases are detailed in Figure 1.4.

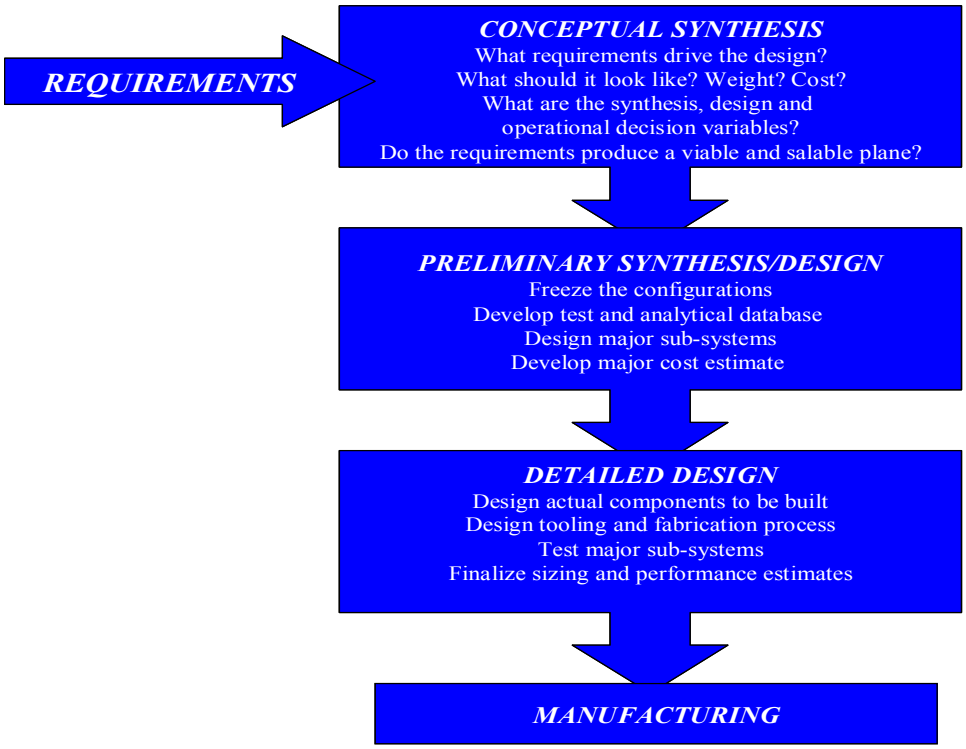

Figure 1.4: Aircraft synthesis/design stages (Raymer, 1999; and Rancruel, 2002).

The conceptual synthesis phase requires the development of numerous configurations of the system, its components, and their interrelations based on customer requirements and system design specifications. The fundamental purpose for this phase is to determine the basic configuration arrangement, size, weight, and performance of the aircraft considered. This is a highly flexible stage that allows for the incorporation of new concepts and the evaluation of possible improvements to the configurations which conceptually define the system. Today's computer technologies have made it easier to more accuratly to model these complex systems. Faster and more powerful computer algorithms and processing capabilities allow one to consider a larger number of concepts than is possible by relying simply on trial and error and rule-of-thumb methods.

Following the conceptual synthesis phase is the preliminary synthesis/design phase. At this point in the synthesis/design process, the base configuration (synthesis)

has been set and no more major changes will be made. In this phase, each of the separate structures of the airframe (wing, landing gear, engine, tail, fuselage, etc.) are assigned to different synthesis/design groups where more detailed synthesis/design can take place. A key activity during this phase is "lofting". Lofting refers to a mathematical modeling process that ensures proper fitting and packaging of the separate structures of the airframe since they are synthesized/designed by different groups and at different locations.

The last phase of the synthesis/design process of the aircraft is the detailed design phase where the aircraft enters full-scale development. This is the phase of the process where the actual pieces of the aircraft that will be fabricated are designed. An important aspect of the detailed design is called production design. This is the design stage where specialists decide on fabrication methods usually finding the easiest or cheapest way of manufacturing an item while still allowing that item to meet the original requirements. This is also the design phase where vigorous testing occurs making sure that every part is properly designed.

1.3 The Need for Large-scale Optimization using Genetic Algorithms (GAs)

As mentioned earlier the morphing wing aircraft presented in this work is composed of two subsystems; a PS and an AFS-A. The combination of these two subsystems can be simply viewed as an energy conversion system (i.e. fuel is converted into kinetic and potential energies). These systems generally contain a large number of independent variables, which can make optimization through trial and error trade-off analysis and hand calculations difficult, if not impossible. Therefore, a means of computational optimization is extremely beneficial for developing and analyzing these systems in order to find the optimum synthesis/design.

Unfortunately, most energy conversion systems have a number of characteristics that make them especially difficult to optimize (Leyland, 2002). Furthermore, energy conversion systems, like the one presented in this thesis work, are highly nonlinear and, therefore, require relatively robust optimizing tools for proper optimization. Energy

conversion system models often exhibit discontinuous or disjointed behavior. Thus, the optimal surface does not have smooth derivatives (the surface contains a number of jumps) creating several completely different feasible regions, each having its own optimum and with no easy route for passing from one region to another. Also, due to a lack of vision of the processes occurring in the model, derivatives of the outputs with respect to the inputs are generally unavailable. Traditional optimization methods, such as gradient-based techniques, require that the optimization surface be smooth and continuous and furthermore such methods have the tendency due to the high non-linearity of the problems to get stuck at local optimums. Genetic Algorithms (GAs), on the other hand, can overcome this impasse by means of specialized search schemes. These types of algorithms specialize in performing a complete search of the entire synthesis/design space for possible solutions. This process is more laborious and takes longer than a gradient-based approach, but the likelihood of closing in on a global optimum is considerably improved.

1.4 The Use of Exergy Analysis

As an alternative to mathematical optimization or for purposes of providing further insights into the synthesis/design results generated by such an optimization, an exergy-based synthesis/design analysis approach can be used. Such an approach can improve existing analysis and optimization methods by, for example, relating every system component and subsystem to the overall system requirements in a framework of common metrics. This analysis method is reasonably mature for the synthesis/design of stationary power and cogeneration systems. Exergy analysis has also been used as a potential method for aircraft system synthesis/design analysis and optimization. The advantages of exergy-based methods come from their ability to support all required levels of synthesis/design activity in a unified fashion aiding the search for system-level, optimized syntheses/designs. This approach can streamline the analysis and optimization process for component, subsystem, and overall system synthesis/design, minimize testing, and reduce certification time and costs.

Exergy, which is also called availability or available energy (Gyftopolous and Beretta, 1991), is a non-conserved thermodynamic property that provides insight into

understanding the loss mechanisms present in mechanical, thermal, and chemical processes. Unlike energy which provides no information on such mechanisms since it can neither be created nor destroyed, exergy quantifies the quantity and the quality of the energy present in the system relative to some "dead state" reference value, thus, allowing one to track of losses or irreversibilities present in a system. In this way, an exergy analysis makes it possible to audit all subsystem components regardless of type (e.g. a wing versus a turbine versus a compact heat exchanger) and identify the components that produce the most losses (i.e. destroy the most exergy) and which can benefit the most from synthesis/design improvements.

One of the objectives of this research is to perform an exergy analysis on the mechanical, thermal, and chemical processes that occur in the subsystems of a morphing wing fighter aircraft system and to optimize the system by minimizing the total amount of exergy destroyed within the overall system. The results obtained from the exergy analysis and optimization are then compared with optimum results obtained by a traditional energy approach. Since the primary focus of this research is to determine the benefits, if any, of morphing wing aircraft with respect to traditional, fixed wing aircraft, an exergy analysis provides an additional tool for measuring such benefits if present.

1.5 Thesis Objectives

As presented in this introductory chapter, there are a large number of possibilities for morphing wing aircraft in the future of flight and aircraft synthesis/design. The primary goal of this thesis research is to quantitatively determine the possible performance benefits that a morphing wing aircraft could have over that of to a traditional, fixed-wing aircraft of essentially the same design (minus morphing capabilities, of course). Since the models presented in this thesis are viewed as energy conversion systems, the means by which performance can quantitatively be assessed is energy consumption over the entire aircraft mission. Therefore, the objective used in optimizing aircraft synthesis/design for a given mission is that of minimizing the total amount of energy consumed. One obvious way to do this is to minimize the amount of fuel consumed over the mission, which is the first objective function chosen for this thesis work. Another way is to maximize the efficiency of energy conversion into useful

work by minimizing the destruction of exergy and the loss of fuel exergy out the back end of the aircraft. This results in the second and third objectives chosen here. A fourth objective which is that of maximizing thrust efficiency is an energy-based metric chosen for comparison purposes which minimizes energy consumption while at the same time maximizing thrust.

These four objectives will be used here to help quantify potential morphing aircraft benefits. However, in order to do so, a number of objectives must be met. They are as follows:

- Through literature study and evaluation gain a fundamental understanding of aircraft synthesis/design and aircraft morphing concepts to be used in a synthesis/design process.
- Understand the fundamentals of the operation of an advanced fighter aircraft system as a whole (i.e. the sum of its subsystems). The two subsystems considered for this research are the airframe subsystem (AFS) and the propulsion subsystem (PS).
- Develop thermodynamic, aerodynamic, geometric, and physical models of the subsystem components and identify the interactions between them. Consider the off-design performance of the components to more accurately model the aircraft system.
- Develop a complete mission for an advanced fighter aircraft based on Mattingly et al. (2002)
- Determine the irreversible loss mechanisms in each component and develop accurate methods to calculate the entropy generated or exergy destroyed for each loss mechanism.
- Define and choose appropriate geometric parameters that affect the aerodynamic properties of the wing for use as morphing variables.
- Define and use an appropriate optimization tool to be coupled with the aircraft computer models to find a set of values for the decision and operational variables that optimize a set of desired objective functions.

- Define a set of four optimization problems for each of the aircraft models, including objective functions, decision variables, operational variables, and constraint values.
- Document and analyze the results for the exergy analyses and the various optimizations made of the morphing and fixed wing aircraft systems.
- Compare the results obtained for the morphing wing aircraft model to the fixed-wing aircraft model and draw appropriate conclusions on morphing wing performance benefits.

Chapter 2

Literature Review

A lot of useful research is being produced on the value of aircraft morphing structures as well as on applications of exergy analysis and optimization for aircraft system synthesis/design and operation. This chapter will look at a sampling of all of those which have appeared in the literature. We begin first with a look at the effect of morphing structures on aircraft synthesis/design and performance.

2.1 The Impact of Morphing Technologies on Aircraft Performance – (Bowman, Sanders, and Weisshaar, 2002)

An example of the ongoing research that demonstrates the potential benefits of morphing principles in aircraft vehicles is presented in Bowman, Sanders, and Weisshaar, (2002). The authors present a mathematical evaluation of different morphing mechanisms in order to gain an understanding of the effect that they can have on an aircraft. Special importance is given to the ability to morph and control the wing shape in planform and profile. The effects of morphing on vehicle kinematics are demonstrated for a turn radius. At a system level, the effects of variable lift-to-drag ratio and specific fuel consumption (both of which can be varied through wing morphing) were examined for a cruise mission.

The first objective of this reference was to identify the different morphing mechanisms that needed to be considered. This process starts by identifying a figure of merit (e.g. turn radius) that is deemed important to the customer and applying a decomposition process to it so that the morphing parameters can be identified. An example of this decomposition process is demonstrated in Figure 2.1 using turn radius as the figure of merit.

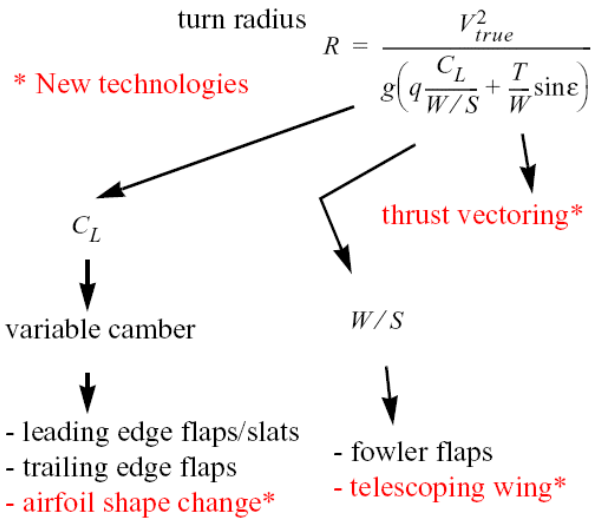

Figure 2.1: Several levels of functional decomposition applied to a turn radius requirement (Bowman, Sanders, Weisshaar, 2002).

In Figure 2.1, V_{true} represents the actual aircraft speed, W/S is the wing loading, and T/W is the thrust-to-weight ratio. As shown in this figure, the turn radius expression contains three technology parameters: wing area (S), lift coefficient (C_L), and the thrust gimble angle (ε). Thus, the physical morphing mechanisms such as flaps, airfoil shape change, and telescoping wings appear.

The authors investigated the effects of changing the lift-to-drag ratio, L/D, and the specific fuel consumption, SFC, for cruising flight with takeoff gross weight, W_{TO}, as the figure of merit. The aircraft L/D and SFC were determined to be direct functions of morphing mechanisms so that an indirect relationship between W_{TO} and morphing exists at a system level. The gross takeoff weight of an aircraft was estimated as

$$W_{TO} = \frac{b + W_{Payload}}{\beta - m} \tag{2.1}$$

where the constants m and b depended on the type of aircraft being considered, and β is the aircraft weight ratio (W/W_{TO}). An estimate for the empty weight of an aircraft was made based on historical data such that

$$W_E = AW_{TO}^{C+1} \tag{2.2}$$

where A and C are coefficients defined by aircraft type. The aircraft's weight change, SFC, and L/D were then all related through the Breguet Range equation given by

$$\frac{W_{i+1}}{W_i} = \exp\left(\frac{-R \times SFC}{aM(L/D)}\right) \tag{2.3}$$

where R is the range distance, M is the vehicle Mach number, and a is a coefficient defined by aircraft type. To see the effect of changes in L/D and SFC on the W_{TO}, the logarithmic derivative of equation (2.3) can be taken in terms of equations (2.1) and (2.2) and yields the following equation:

$$\frac{\partial W_{TO}}{W_{TO}} \frac{L/D}{\partial L/D} = \frac{\partial W_{TO}}{W_{TO}} \frac{SFC}{\partial SFC} = \left(\frac{R \times SFC}{aM(L/D)}\right) \frac{\beta}{\beta - m} \tag{2.4}$$

Equation (2.4) suggests that the change in W_{TO} with L/D or SFC is less when the range is small, L/D is high, or SFC is low. It also says that when the empty weight is sensitive to the gross take-off weight (high values of m), L/D and SFC have a larger impact on W_{TO}. Figure 2.2 shows typical empty weight-to-takeoff weight and gross take-off weight-to-L/D (or SFC) sensitivities.

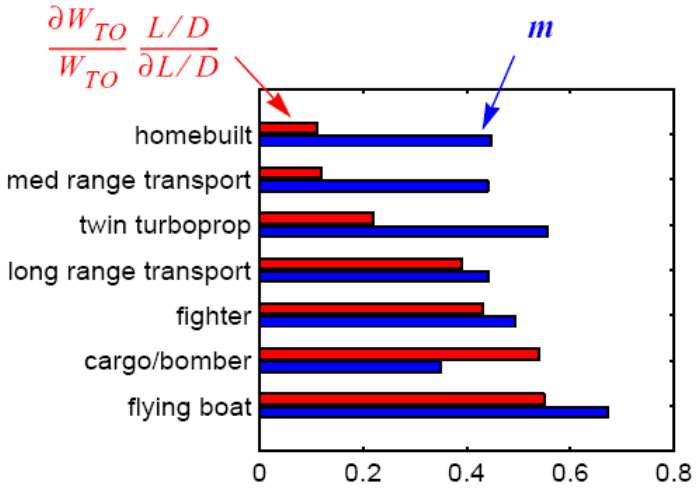

Figure 2.2: Empty and takeoff gross weight sensitivities of typical aircraft (Bowman, Sanders, Weisshaar, 2002).

Although the cargo aircraft has the lowest empty weight to gross take-off weight sensitivity, a long range requirement makes the aircraft particularly sensitive to L/D and SFC. A twin turboprop has high empty weight to gross take-off weight sensitivity but is used as a short range commuter aircraft making its L/D and SFC sensitivity relatively low.

The authors also look into how morphing affects the aircraft kinematics with a turn radius example. Figure 2.3 shows a portion of an aircraft constraint diagram for two different turning radius conditions (500 ft and 700 ft). If an aircraft is flying in mountainous terrain during an attack, a more stringent turn radius may be necessary.

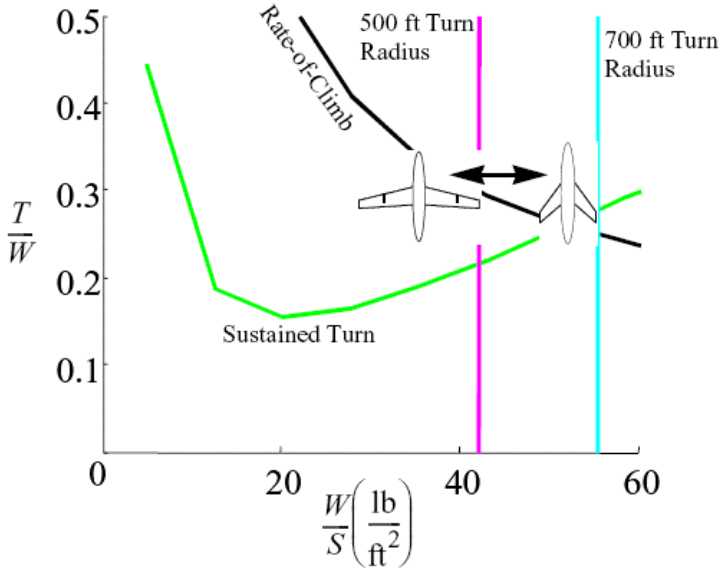

Figure 2.3: Morphing to meet the turn radius requirement and keep the wing loading (*W/S*) high (Bowman, Sanders, Weisshaar, 2002).

Figure 2.1 shows that the turning radius can be decreased with a decrease in the wing loading, *W/S*, which requires an increase in the wing planform area, *S*. The turning radius of the aircraft can drop from 700 ft to 500 ft with a 20% increase in wing area through telescoping wings and reducing the sweep angle. For this configuration, however the rate-of-climb constraint is no longer satisfied, but this is of no concern since the wing's geometry change is only temporary and can change back to an acceptable geometry during the climb segment of the mission.

In conclusion, the authors of this reference brought to light several possible benefits of morphing aircraft capabilities by demonstrating how wing morphing can allow performance advantages over non-morphing aircraft. This work specifically showed improvements in aircraft range and turning radius over those attainable in traditional non-morphing aircraft.

2.2 Application of Optimization Techniques to the Conceptual Design of Morphing Aircraft (Roth and Crossley, 2003)

Roth and Crossley (2003) present another study on the benefits of morphing aircraft. In this work, the authors used a computer simulation of a model of a morphing aircraft flown over a fixed mission. A fixed-geometry aircraft model was also created as a baseline case for comparison. A set of geometric wing features that could be varied during flight were chosen as the morphing variables. By including morphing variables that describe the aircraft's geometry for each mission segment, the aircraft's weight, size, and performance were all functions of the morphing. For this reason, the authors refer to this approach as "morphing as an independent variable". The different sizing and corresponding morphing variables are presented in Table 2.1, with the latter corresponding to each of the mission segments listed in Table 2.2 and depicted in Figure 2.4.

Table 2.1: Basic sizing variables and corresponding morphing variables (Roth, Crossley 2003).

Basic Sizing Variable	Morphing Variables
W/S	$(W/S)_{TOL}$, $(W/S)_{cr1}$, $(W/S)_{loiter}$, $(W/S)_{dash}$, $(W/S)_{cr2}$
AR	AR_{TOL}, AR_{cr1}, AR_{loiter}, AR_{dash}, AR_{cr2}
Λ	Λ_{TOL}, Λ_{cr1}, Λ_{loiter}, Λ_{dash}, Λ_{cr2}
t/c	$(t/c)_{TOL}$, $(t/c)_{cr1}$, $(t/c)_{loiter}$, $(t/c)_{dash}$, $(t/c)_{cr2}$
T/W	

The subscripts of each of the morphing variables presented in Table 2.1 are further described in Table 2.2. In order to account for the affects of morphing, the aircraft is flown through the mission presented in Figure 2.4. The morphing variables in Table 2.1 correspond to each mission segment presented in Figure 2.4.

The primary goal of this work was to design a morphing aircraft that could fly the set mission at a gross takeoff weight lower than that of an aircraft of fixed geometry. Due to the large number of variables that resulted from morphing the aircraft during each mission segment, an optimization technique was needed to find the combination of

variables that met all the mission requirements for the lowest possible gross takeoff weight.

Table 2.2: Listing and subscript designation of mission segments.

Mission Segment	Subscript
Takeoff and Landing	TOL
Cruise 1	cr1
Loiter	loiter
Dash	dash
Cruise 2	cr2

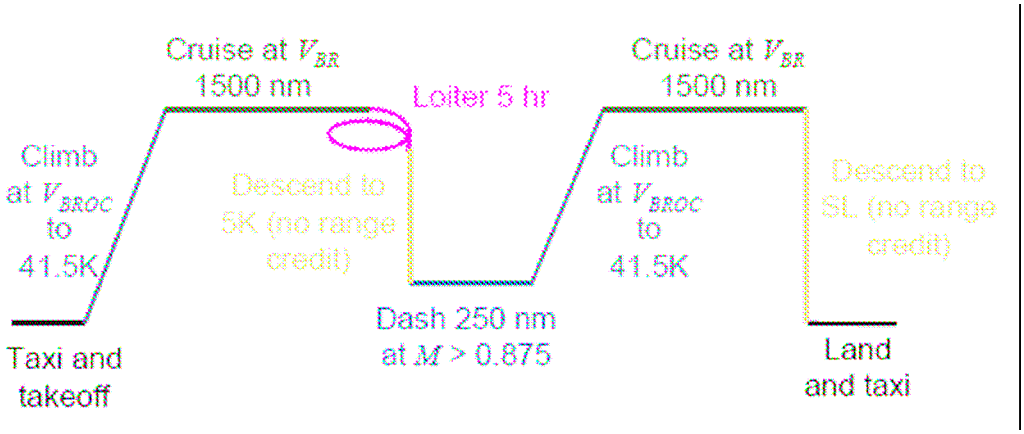

Figure 2.4: Notional morphing aircraft mission (Roth, Crossley 2003).

A genetic algorithm (GA) was used to perform this optimization due to its superior global search scheme over the more common gradient-based optimization tools. A drawback of using this type of optimization approach was that it was computationally expensive.

The GA was first used to generate an optimum fixed-geometry aircraft design that represented the lowest possible gross takeoff weight that could complete the mission shown in Figure 2.4. Only five decision variables appeared in this problem formulation; thrust loading (T/W), wing loading (W/S), aspect ratio (AR), thickness-to-chord ratio (t/c), and wing sweep (Λ). The results of the GA for the fixed-wing case are presented in Table 2.3 and a planform sketch of the optimum fixed wing geometry is shown in Figure 2.5.

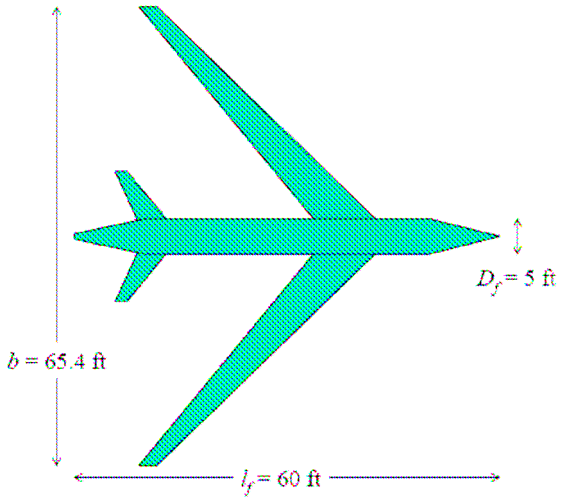

Figure 2.5: Planform sketch of best GA-generated fixed-geometry design (Roth and Crossley, 2003).

Table 2.3: Optimum design decision variable values for best GA-generated fixed-geometry aircraft (Roth and Crossley, 2003).

Design Variable	Value
T/W	0.363
W/S [lb/ft^2]	76.2
AR	10.6
t/c	0.10
Λ [deg]	44

The GA was then used to generate an optimum morphing wing aircraft design that represented the lowest possible gross takeoff weight that could complete the given mission. The bounds on the morphing parameters allowed to change during the mission were based on a percent deviation from the fixed-wing parameters shown in Table 2.3. The decision variables for the morphing wing problem formulation were the same as the set used in the fixed-wing problem with different values for each mission segment. This gave the morphing wing GA run a total of 22 decision variables. The results of the GA for the morphing wing case are presented in Table 2.4 and planform sketches of the optimum wing geometries for the dash and loiter mission segments are shown in Figure 2.6.

Table 2.4: Optimum GA-generated design for morphing wing aircraft (Roth and Crossley 2003).

Design Variable	Value	Design Variable	Value
T/W	0.319	AR_{loiter}	15.2
W/S [lb/ft^2]	108	AR_{dash}	9.1
AR	15.2	AR_{cr2}	15.2
t/c	0.119	Λ_{cr1} [deg]	15.0
Λ [deg]	15.0	Λ_{loiter} [deg]	15.0
$(W/S)_{cr1}$ [lb/ft^2]	67.3	Λ_{dash} [deg]	44.75
$(W/S)_{loiter}$ [lb/ft^2]	67.3	Λ_{cr2} [deg]	15.0
$(W/S)_{dash}$ [lb/ft^2]	108	$(t/c)_{cr1}$	0.119
$(W/S)_{cr2}$ [lb/ft^2]	67.3	$(t/c)_{loiter}$	0.093
$(W/S)_{TOL}$ [lb/ft^2]	67.3	$(t/c)_{dash}$	0.138
AR_{cr1}	15.2	$(t/c)_{cr2}$	0.119

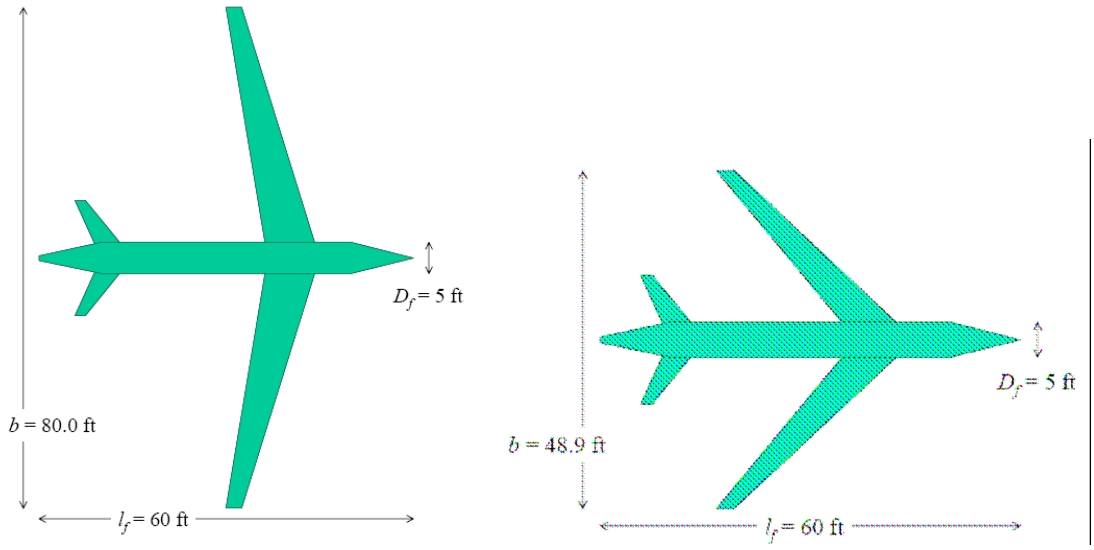

Figure 2.6: Planform sketches of morphing aircraft for loiter (left) and dash (right) mission segments (Roth and Crossley 2003).

The results of the two cases show a clear potential for improved performance of the morphing wing aircraft over the fixed-geometry aircraft. The gross takeoff weight of the best morphing aircraft produced is 7.7% lower than that of the best fixed-geometry aircraft (28,355 lb vs. 30,706 lb). Additionally, the morphing aircraft has a lower thrust-to-weight ratio (12% lower than the fixed-geometry aircraft) and a correspondingly lower installed thrust requirement (19% lower total installed thrust). This reduction in engine size implies a lower cost engine to complete the same mission. We next look at the application of exergy analysis and optimization to the synthesis/design of aircraft.

2.3 A Method for Propulsion Technology Impact Evaluation via Exergy Analysis (Roth and Mavris, 2000)

As an example of what exergy analysis can produce, Roth and Mavris (2000) present a comparison between a traditional analysis method commonly used in cycle technology trade studies and exergy analysis methods. Both methods were applied to the analysis of a known aircraft, a Northrop F-5E powered by J85-GE-21 engines. A set of engine cycle technologies were defined so that both the traditional and exergy analysis methods could be applied. This allowed the authors to quantify the impact of the various engine and airframe combinations considered. The mission used was a 225 nautical mile radius subsonic area intercept. The range of values permitted for the turbine inlet temperature (TIT) were from 2200 R to 2600 R, and the range of acceptable values for the cycle pressure ratio (OPR) were from 8 to 14. The design-point efficiencies and cooling flow rates were held constant for all of the cases considered.

The results for 12 engine cycles (four values of OPR and three of TIT) using the trade study approach showed that the TIT has a strong affect on both the specific thrust (ST) and the specific fuel consumption (SFC) as shown in Figure 2.7. An increase in the TIT produces strong increases in the ST and moderate increases in the SFC. Increases in the TIT also lead to improved heat transfer and materials. Conversely, increases in the OPR produce significant drops in the SFC, while only having minimal effects on the ST values depending on the TIT.

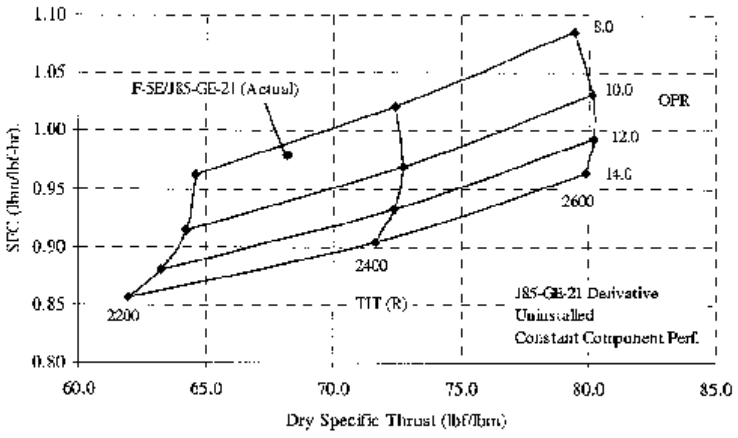

Figure 2.7: Trade study results of the effects of TIT and OPR variations on ST and SFC. The F-5E is operating at full military power (Roth and Mavris 2000).

The trends and results presented by the trade study in this figure are typical. However, the question remains, how close to the ideal cycle are these engines cycles? Without this information, the designer has no idea about how much, if at all, these engine cycles can be improved. Also, no guidance is available with regards to the sources and magnitudes of the losses occurring inside of the engine. This lack of knowledge can be overcome by applying an exergy analysis on the engine system for each of the twelve cycles. The results of this sort of analysis are shown in Figure 2.8.

From this figure, it is clear that an increase in the OPR leads to a decrease in exergy destruction primarily due to a decrease in residual heat and combustion irrevesibilities. It is also apparent that an increase in the TIT reduces exergy losses due to a decrease in combustion irreversibilities in the afterburner as well as a decrease in exhaust heat exergy loss, which is counterintuitive from the standpoint of a typical Brayton cycle. This decrease is caused by the fact that a higher TIT requires a smaller engine, which results in a net benefit at the overall system level.

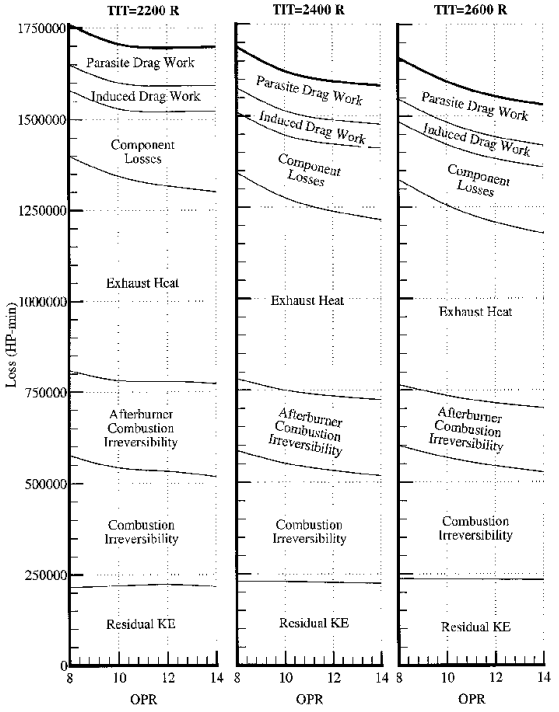

Figure 2.8: Exergy usage for a F-5E subsonic area intercept mission as a function of cycle pressure ratio (OPR) and turbine inlet temperature (TIT) (Roth and Mavris 2000).

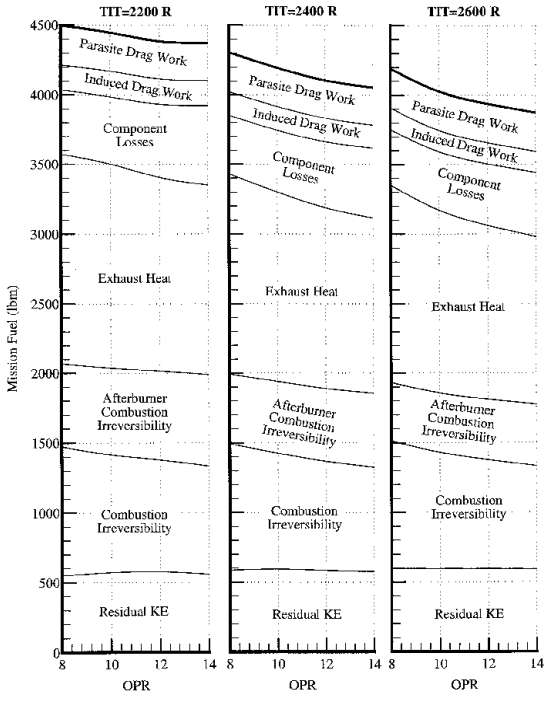

Figure 2.9: Mission fuel usages for a F-5E subsonic area intercept mission as a function of cycle pressure ratio (OPR) and turbine inlet temperature (TIT) (Roth and Mavris 2000).

Figure 2.8 also shows that about 60 % of the system losses occur due to exergy lost through the exhaust heat and irreversibilities in the combustor and afterburner. Thus, development of new technologies could create the most benefit in these three loss sources. The data presented in Figure 2.8 can also be expressed in terms of chargeable mission fuel, as shown in Figure 2.9. This figure shows the same trends as before, but the losses are expressed in terms of fuel mass rather than exergy loss. The information contained in this figure can be used as a means of cost accounting in vehicle economic analysis. For instance, since it is possible to analytically calculate the fuel weight associated with component losses, it is also possible to estimate mission fuel costs chargeable to specific component losses. This is information that cannot be obtained through conventional vehicle analysis techniques.

2.4 The Thermodynamic Continuum of Jet Engine Performance: The Principle of Lost Work due to Irreversibility in Aerospace Systems (Riggins, 2003)

Another application of exergy analysis to aerospace systems is that of Riggins [13]. In this work, Riggins uses an exergy analysis to characterize the performance of all single-stream jet engines (turbo-jets, ram/scramjets, and inverse-cycle engines) and the results are displayed on 3-D surface plots in terms of specific impulse (SI) and non-dimensional specific thrust (ST). The axes of these plots are the non-dimensional energy added in a heat interaction to the total free-stream enthalpy (Q/C_PT_{ti}), the work interaction between the engine flow and the total free-stream enthalpy, and the non-dimensional entropy generation due to irreversibilities (S_{irr}/R).

Results from the exergy analysis are shown in Figures 2.10 and 2.11. Figure 2.10 shows SI and total temperature contours for scramjet performance (i.e. no work interactions) using hydrogen fuel at a fixed flight Mach number of 8 and an area ratio of unity across the engine. It can be seen from this figure that the maximum SI occurs when the entropy generation due to irreversibilities and the head added are both very low. For an operational scramjet at Mach 8 operating close to stoichiometric, a realistic value for entropy generation of 4 to 5 and a SI of 2000 is very reasonable. As energy added in a

heat interaction is decreased, the most dominate irreversibilities for injection, mixing, and combustion also decrease without a significant decrease in SI.

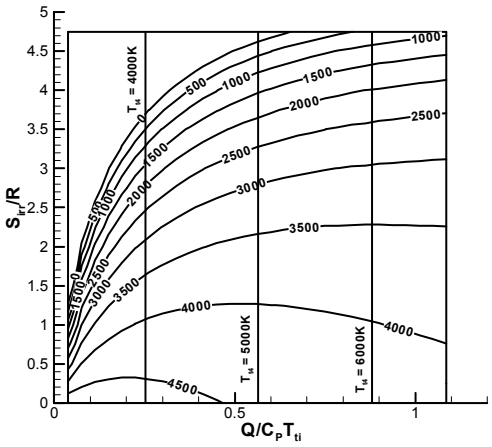

Figure 2.10: Specific impulse contours for the ram/scramjet performance plane (flight Mach = 8, hydrogen fuel, ratio of exit to inlet area = 1.0) (Riggins, 2003).

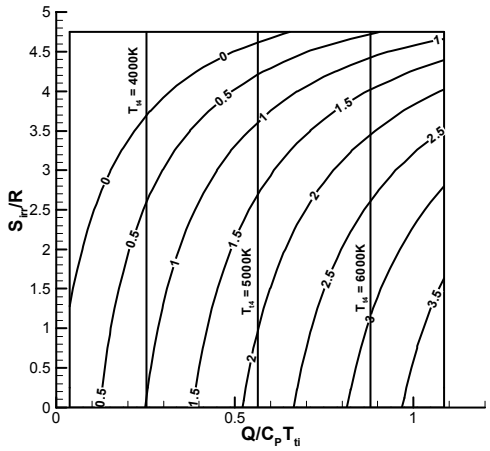

Figure 2.11: Non-dimensional specific thrust contours for the ram/scramjet performance plane (flight Mach = 8, hydrogen fuel, ratio of exit to inlet area = 1.0) (Riggins, 2003).

Figure 2.10 also shows the possible growth potential as well as the limitations for high-temperature materials when considering both the SI and total temperature contours. The use of high-temperature materials may not be justified in this case if the cost of flow irreversibilities in reaching those temperatures is too large causing the performance to decline. Figure 2.10 indicates that this becomes more challenging as technology is improved since the SI reaches a plateau as the energy added in a heat interaction increases at high exit temperatures.

Figure 2.11 shows additional results from the exergy analysis, except this figure contours the ST, which is a measure of delivered thrust to engine size. In contrast to the SI trends in figure 2.10, figure 2.11 shows that the maximum ST occurs at high values of Q/C_PT_{ti} and low values of S_{irr}/R.

The exergy analysis of ram/scramjet engines that is summarized in figures 2.10 and 2.11 provides information not available from a traditional trade study. The exergy analysis shows both quantitatively and qualitatively the diminishing influence of additional energy transfer due to heat interactions to the free-stream on scramjet engine performance. This is due to the asymptotic nature of the energy release resulting from a heat interaction in a scram combustor caused by fuel mixing and chemical kinetics and to

the fact that entropy generation due to irreversibilities remains significant even as the energy release diminishes in the latter part of the combustor. This exergy analysis reveals that significant additional thermodynamic effect, which drives the design to ever shorter combustor lengths. The impact on scramjet engine performance of an energy release due to a heat interaction is negligible with respect to SI and small with respect to ST, a trend that significantly worsens as engine irreversibilities mount. Furthermore, this analysis demonstrates the critical impact on scramjet synthesis/design of correctly assessing the trade off between irreversibilities and combustion heat release.

2.5 Parametric Exergy Analysis from Investigation of the Effects of Different Objective Functions/Figures of Merit on the Analysis and Optimization of High Performance Aircraft System Synthesis/Design (Periannan, 2005)

Another application of exergy analysis in aerospace applications is in the work of Periannan. In this work, Periannan performs a parametric exergy analysis on an air-to-air fighter aircraft (AAF) vehicle that focuses on the propulsion subsystem (PS). This analysis identifies the behavior of some of the key system quantities for different aircraft flight segments with changes in compressor pressure ratio, fan bypass ratio, and the turbine inlet temperature for the PS.

The results of this exergy analysis show a number of interesting trends with regards to the exergy destruction rate and the specific thrust. Given a compressor pressure ratio of 8 and a given specific thrust value, the rate of exergy destruction in the PS decreases for all flight segments with decreasing by-pass ratios and turbine inlet temperatures as shown in Figure 2.12. Thus, with regards to exergy analysis, a better, more efficient PS will be created for designs that minimize both the engine by-pass ratio and the turbine's inlet temperature.

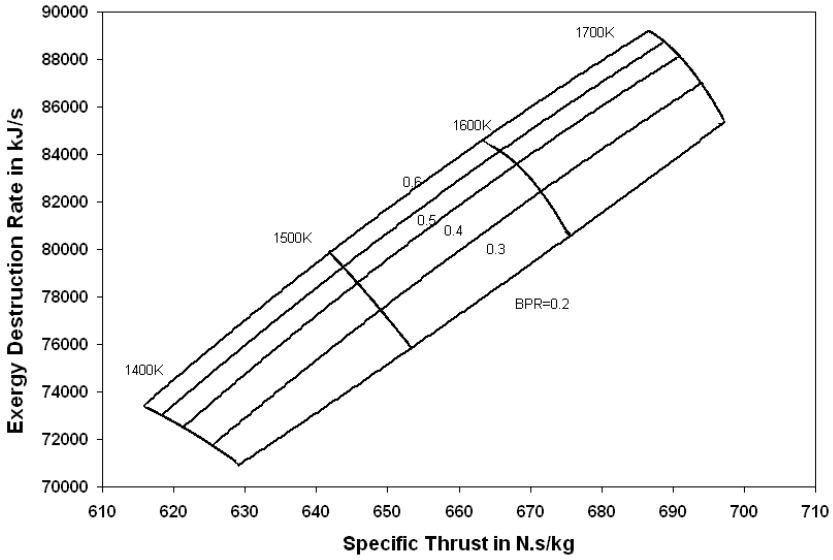

Figure 2.12 Variation of vehicle specific thrust and exergy destruction rate with fan bypass ratio and turbine inlet temperature for a fixed compressor pressure ratio of 8 (mission segments 1 and 2 : Warm-up/Take off Acceleration).

Also, for a fixed turbine inlet temperature of 1700K, increasing the compressor pressure ratio causes both an increase in the specific thrust and a rapid decrease in the rate of exergy destruction at all flight segments as shown in Figure 2.13.

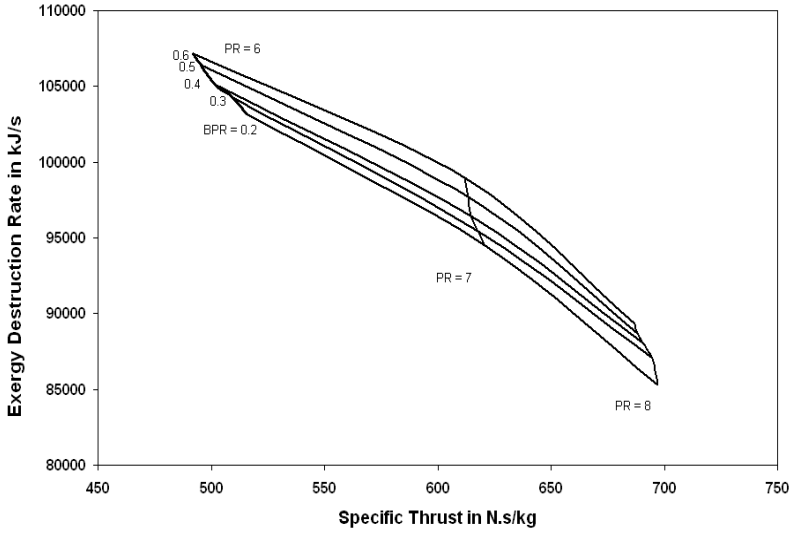

Figure 2.13: Variation of vehicle specific thrust and exergy destruction rate with fan bypass ratio and compressor pressure ratio for a fixed turbine inlet temperature of 1700 K (mission segments 1 and 2: Warm-up/Takeoff Acceleration).

Therefore, high compressor pressure ratios in addition to low engine by-pass ratios contribute to a more efficient PS design. Another discovery of this exergy analysis is that the rate of variation of the exergy destruction rate with the turbine inlet temperature is higher during flight segments that require acceleration and climb than constant speed cruise slight conditions.

Exergy analysis was also explored with respect to the exergy destruction rate of the PS and the specific fuel consumption. For a given compressor pressure ratio of 8 and a fixed value of the specific fuel consumption, the rate of exergy destruction in the PS again decreases with decreasing engine by-pass ratios and turbine inlet temperatures. As shown previously, lower by-pass ratio engines and lower turbine inlet temperatures tend to result in better, more efficient PS designs with respect to thermodynamics. Also, for a given turbine inlet temperature of 1700 K, increasing the compressor pressure ratio in turn decreases the rate of exergy destruction in the PS and decreases the specific fuel consumption. This further solidifies the idea that lower engine by-pass ratios and turbine inlet temperatures, and higher compressor pressure ratios result in better, more efficient engine designs (i.e. lower rates of exergy destruction and specific fuel consumption).

2.6 Exergy Methods for the Generic Analysis and Optimization of Hypersonic Vehicle Concepts (Markell, 2005)

Another example of the application of exergy analysis found in aerospace research is the M.S. thesis work of Markell (2005). This work uses an exergy analysis method for optimization and compares it with the traditional energy-based methods for the synthesis/design and operational optimization of a hypersonic vehicle. Multiple optimizations are performed on the combustor, the scram jet engine, and the entire vehicle system (engine and airframe).

In this work, Markell performs a parametric exergy analysis on the scramjet vehicle to determine the performance effects of the different design decision variables. The parameters used to track the performance effects are the specific thrust, which is the thrust divided by the mass flow rate of the air passing through the engine, and the specific rate of exergy destruction, which is the rate of exergy destruction divided by the mass flow rate of air passing through the engine. The design decision variables that are used in

this parametric study are the first inlet ramp length, X_{ramp1}, the forebody angle, θ_{fb}, the nozzle expansion angle, θ_{nozz}, the combustor length, L_{comb}, and the percent cowl, $\%_{cowl}$.

The performance parameters are first explored by changing the X_{ramp1} and θ_{fb} while keeping all other design variables fixed. This configuration shows that an increase in X_{ramp1} produces an increase in the specific thrust as well as a appreciable increase in the rate of specific exergy destruction. Also, for large values of X_{ramp1} increasing the θ_{fb} results in a decrease in the rate of specific exergy destruction. However, as X_{ramp1} decreases, increasing the θ_{fb} results in an increase in the rate of specific exergy destruction. These results show that the largest achievable specific thrust does not produce the highest rate of specific exergy destruction.

Next, the performance effects of the design variables of combustor length, nozzle expansion angle and percent cowl are explored while keeping all other variables fixed. This configuration shows that increasing the combustor length causes a substantial increase in the specific exergy destruction and a moderate increase in the specific thrust. Increases in the nozzle expansion angle lead to increases in the specific thrust, but have little effect on the specific exergy destruction. A decrease in the percent cowl leads to increases in the specific thrust and also shows little effect on the specific exergy destruction. These results suggest that an efficient scramjet design should have the smallest possible combustor length while maximizing the nozzle expansion angle and minimizing the percent cowl of the scramjet design.

A preliminary study into the effectiveness of the exergy based method for use in the synthesis/design of a hypersonic vehicle was performed. This study used two different objective functions (energy and exergy based) in order to determine the optimum combustor length that provides the best vehicle performance.

The energy-based objective function was thrust-based engine effectiveness given by

$$\eta_{ee}(x) = \frac{\dot{m}u_e(x) + P_e(x)A_e - (\dot{m}u_0 + P_0A_0)}{\dot{m}u_{eideal} + P_{eideal}A_e - (\dot{m}u_0 + P_0A_0)} \tag{2.3}$$

where $\dot{m}u + PA$ is the stream thrust of the engine. The exergy-based objective function was the thermodynamic efficiency expressed by

$$\varepsilon(x) = 1 - \frac{T_0 s_{irr}(x)}{\delta Q_{release}(x)\left(1 - \frac{T_0}{T_t(x)}\right)} \tag{2.4}$$

As seen in Figure 2.12 the optimal combustor length and thrust predicted by the two different objective functions are effectively identical.

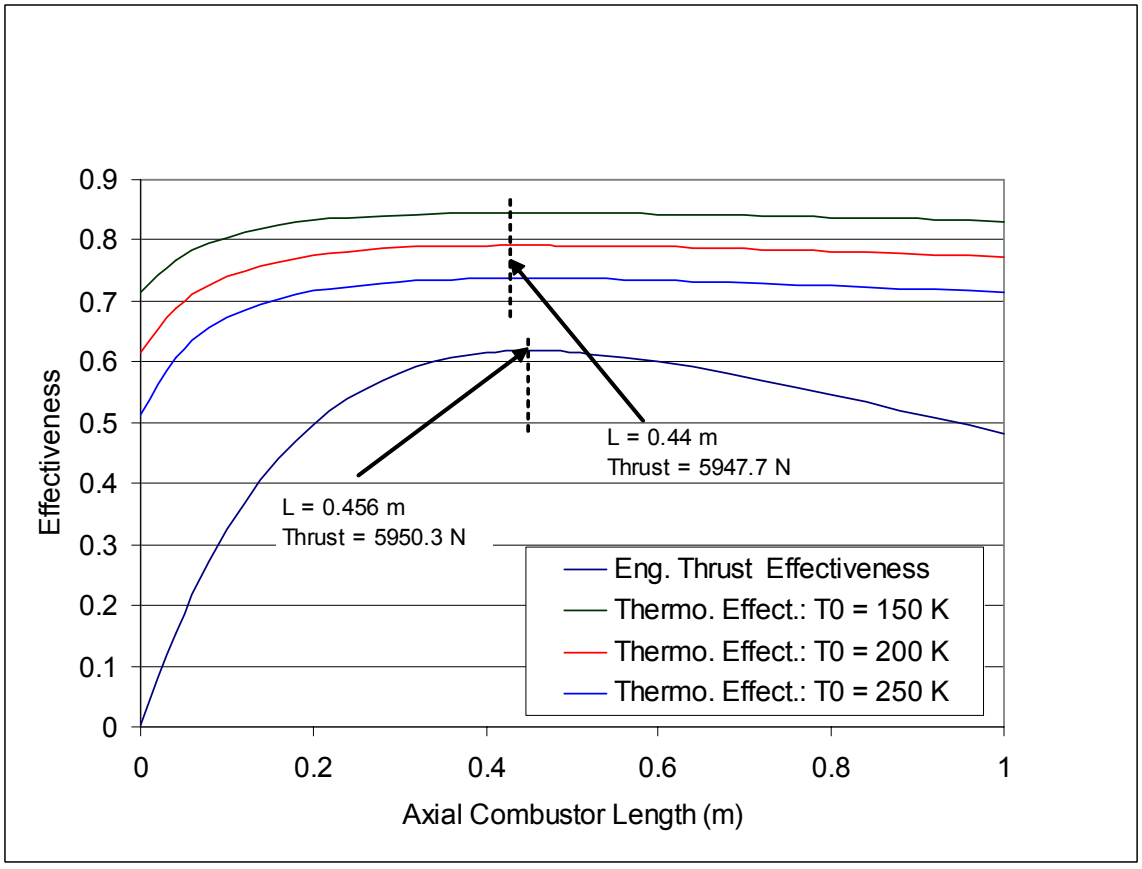

Figure 2.14: Optimal combustor lengths predicted by the thrust and thermodynamic efficiencies (Brewer, 2006).

A more detailed study of scramjet engine design for a hypersonic vehicle was also conducted by Markell (2005) in order to compare the optimal scramjet engine design determined with two different energy and exergy-based objective functions. The maximization of the overall thrust efficiency (η_o) was used as the energy-based objective and is expressed as

$$\eta_o = \frac{Tu_o}{\dot{m}_f h_{pr}} \tag{2.5}$$

The minimization of the rate of exergy destruction ($\dot{E}x_{tot}$) due to irreversibilities and exergy loss due to unburned fuel was used as the exergy-based objective function and is given by

$$\dot{E}x_{tot} = \dot{E}x_{des} + \dot{E}x_{fuel_{loss}} \tag{2.6}$$

The optimizations are performed with the ultimate goal of finding out which scramjet engine design uses the least amount of fuel for a fixed thrust setting (i.e. for a given mission segment). The optimum decision variables values are shown in Table 2.4 show that both objective functions in this case (i.e. for fixed thrust) produce similar designs and nearly identical amounts of fuel consumption during flight. These results demonstrate that the exergy-based method can be used with confidence to determine the optimal scramjet engine configuration which uses the minimum amount of fuel, but with the added benefit that the magnitude and location of the individual loses throughout the engine can be directly and proportionately tied back into this overall global optimization result.

Table 2.4: Optimization decision variable values for the energy-based and exergy-based optimal scramjet engine designs determined for a fixed thrust (Markell, 2005).

Obj. Function	X_{fb}	X_{cowl}	X_{ramp1}	θ_{fb}	θ_{nozz}
1st Law	8.6114	13.652	2.9049	4.6026	17.066
1st/2nd Law	8.4019	13.895	3.1784	4.5669	17.549
	L_{comb}	$\%_{cowl}$	$\dot{m}_f$ (kg/s)	ϕ	$\forall_{veh}$ (m^2)
1st Law	1.1148	0.0016	2.6363	0.5	26.039
1st/2nd Law	1.1523	0.0113	2.6754	0.5	26.025

2.7 Methods for Mission-Level Analysis and Optimization of Generic Hypersonic Vehicle Concepts (Brewer, 2006)

Another example of the application of exergy analysis found in aerospace research is the M.S. thesis work of Brewer (2006). This work also uses an exergy analysis method for optimization and compares it with the traditional energy-based methods for the synthesis/design and operational optimization of a quasi one-dimensional

scramjet hypersonic vehicle. Multiple optimizations are performed on the hypersonic scramjet vehicle over a defined flight mission.

In this thesis work, Brewer found that dynamics of scramjets are highly complex and are more constrained than those of conventional aircraft, and the almost indistinguishable boundary between engine and airframe results in a vehicle in which slight changes in one sub-system profoundly affect the other. Consequently, only through the integrated synthesis/design optimization routine, were mission-level solutions obtained, and the search for solutions often had to be refined before the possibility of success even appeared.

The combustor of the scramjet vehicle was the largest source for exergy destruction. It contributed to the overall loss in two ways. Not surprisingly, these two are highly related. Incomplete combustion, heat transfer, friction, and flow mixing losses are minimized for shorter combustor lengths: these are losses due to irreversibilities. Meanwhile, the mixing model, which dictates what percentage of hydrogen released into the flow utilized, is most efficient for long combustor lengths. Because of this relationship, trade-offs between fuel exergy lost in the mixing layer and combustor irreversibilities were plainly recognized.

For the three objective functions (maximized first law overall vehicle efficiency, minimized fuel consumption, and minimized exergy destruction and fuel exergy lost), the minimum fuel mass and minimum exergy destruction and fuel exergy loss proved to be able to meet the mission constraints using nearly identical amounts of fuel. The optimized minimum fuel vehicle preferred larger mixing layer losses while the exergy destruction plus fuel exergy lost minimization vehicle preferred larger combustor irreversibilities. Both consumed similar fuel masses, destroyed similar amounts of exergy, and resulted in sleek vehicle geometries of the same proportion. The optimized first law objective vehicle consumed measurably larger amounts of fuel and destroyed more exergy promoted by a broad, thrust maximizing body.

Finally, an extended mission with increased flight ceiling, gross takeoff weight, and thrust requirements was performed yielding an acceptable vehicle geometry. In addition, comparing single segment optimized vehicles to the overall mission optimized vehicles illustrated the necessity of a fully integrated synthesis/design approach, as few

geometric and performance similarities were found. Thus, for being able to predict minimum allowable fuel usage as well as illustrate dissimilar component technology trade-offs, an exergy based approach is a highly useful tool for integrated system synthesis/design.

2.8 Optimization Results from Investigation of the Effects of Different Objective Functions/Figures of Merit on the Analysis and Optimization of High Performance Aircraft System Synthesis/Design (Periannan, 2005)

This section covers the optimization results for the application of exergy analysis in aerospace applications by Periannan previously reviewed in section 2.5 of this thesis. The final optimizations were performed on the Air-to-Air Fighter (AAF) in this work with degrees of freedom for the Propulsion Subsystem (PS), the Environment Control Subsystem (ECS) and the Airframe Subsystem (AFS-A). The optimizations were originally run without degrees of freedom in the AFS-A, and then rerun with degrees of freedom in the AFS-A. For these optimizations the takeoff wing loading, W_{TO}/S, was used as the design decision variable for the AFS-A. Wing loading is the ratio between the gross takeoff weight and the wing planform area. Optimizations were run for four different objective functions; a pair of exergy based objective functions and a pair of energy based objective functions. The energy based objective functions are to minimize the gross takeoff weight of the aircraft (Objective 1) and to maximize the thrust efficiency of the aircraft (Objective 4). The exergy based objective functions minimize the total amount of exergy destroyed by the aircraft (Objective 3), and the amount of exergy destroyed by the aircraft's energy conversion systems, i.e., not including the AFS-A (Objective 2).

The results from the two different exergy based objective functions (Objectives 2 and 3) were first compared. The resulting amounts of fuel consumed and exergy destroyed and lost by the syntheses/designs of the four objective functions are shown in Figures 2.15 and 2.16, respectively. The optimum value for the objective function that allows degrees of freedom and parasitic drag considerations in the AFS-A (Objective 3) was found to provide a better solution than the optimum value found for that without degrees of freedom and parasitic drag considerations in the AFS-A (Objective 2). The

optimization results of Objective 3 produced a design that reduced the amount of fuel consumption by 8.5% when compared to those of Objective 2.

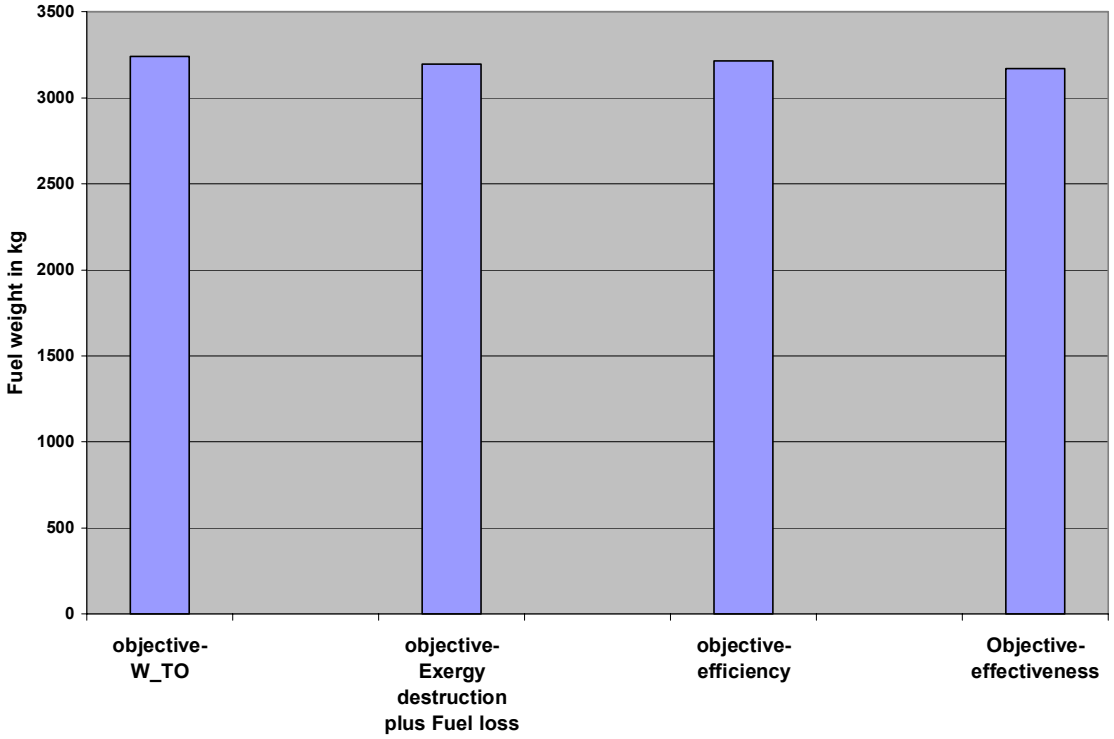

Figure 2.15: Comparison of the optimum fuel weight obtained with four different objective functions/figures of merit, i.e. with objectives 1, 2, 4, and 5, respectively.

The results of Objective 3 also reduced the amount of exergy destroyed and the gross takeoff weight of the AAF when compared to the results of Objective 2. The results of Objective 1 were also found with and without AFS-A degrees of freedom. These results show that the objective function solved with degrees of freedom in the AFS-A produces a better design than the objective function without degrees of freedom in the AFS-A since it decreased the amount of fuel consumed by 4%.

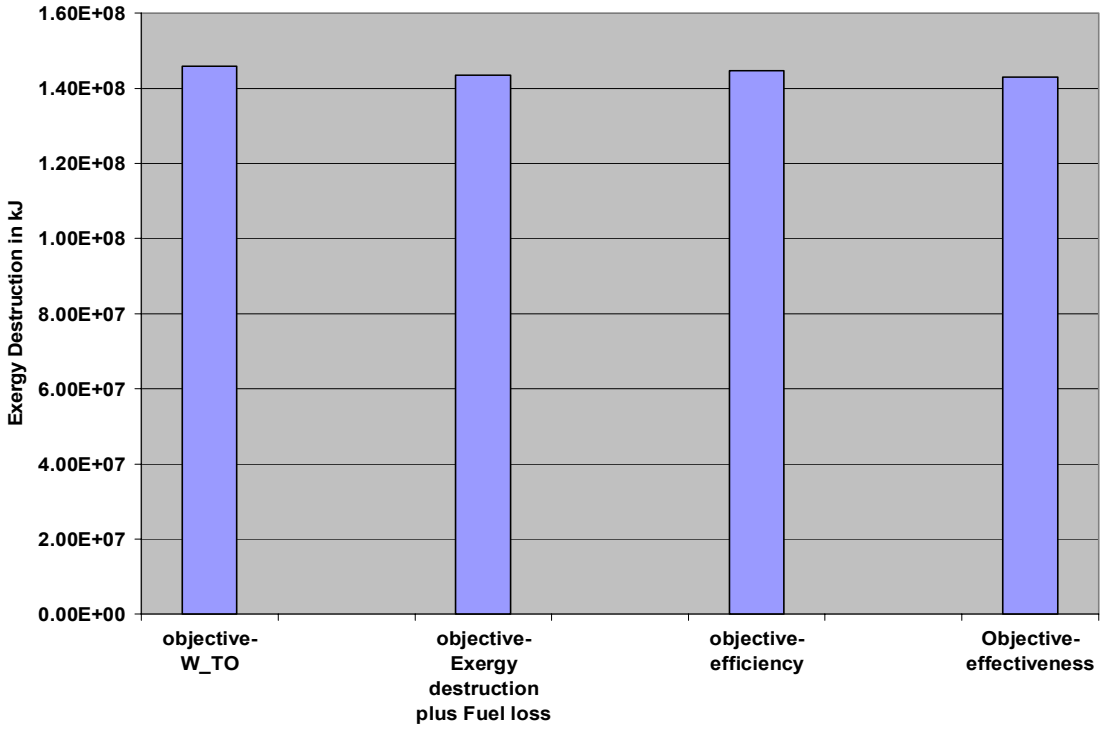

Figure 2.16: Comparison of the optimum exergy destruction obtained with four different objective functions/figures of merit, i.e. with objectives 1, 2, 4, and 5, respectively.

In a comparison between energy-based and exergy-based objective functions, the results show that the optimal solution obtained with the exergy-based objective with AFS-A degrees of freedom (Objective 3) is better than the one obtained using gross takeoff weight as the objective function (Objective 1) without degrees of freedom in the AFS-A. In this case the total fuel consumption for Objective 3 was 9.8% less than that for Objective 1 with degrees of freedom in the AFS-A. This shows a reduction in fuel consumption of more than twice the reduction obtained by Objective 1 with degrees of freedom in the AFS-A. In conclusion, the optimization of the exergy-based objective function with degrees of freedom in the AFS-A produces the best overall design of the AAF vehicle.

2.9 A Decomposition Strategy Based on Thermoeconomic Isolation Applied to the Optimal Synthesis/Design and Operation of an Advanced Fighter Aircraft System (Rancruel and von Spakovsky, 2003, 2005)

The synthesis/design of advanced fighter aircraft has been traditionally accomplished by methods such as rules-of-thumb, individual expertise, and simple trade-off analysis. However, the need for more complex, efficient, and cost effective aircraft systems calls for a more integrated, interdisciplinary approach to the synthesis/design process and optimization of these systems. Such an integrated, interdisciplinary approach to the synthesis/design process is presented in Rancruel and von Spakovsky (2003, 2005) who have developed and applied a decomposition strategy for the large-scale optimization of complex systems, ensuring that the demands made by all subsystems are accommodated in a way which results in the optimum system synthesis/design for a given set of constraints (mission, physical, environmental etc).

A number of types of decomposition, including iterative Local-Global Optimization (ILGO), were applied to the synthesis/design optimization of an advanced tactical aircraft (ATA) system with and without degrees of freedom for the airframe subsystem. The ATA system is decomposed into seven subsystems where two of the systems (the equipment and payload subsystems) are not allowed degrees of freedom. The five remaining ATA subsystems are the propulsion subsystem (PS), the airframe subsystem (AFS-A), the environmental control subsystem (ECS), and the thermal management subsystem (TMS) which itself is comprised of the fuel loop subsystem (FLS) and the vapor compression and Polyalphaonlefin loop subsystem (VC/PAOS). The synthesis/design task to be done is to perform an integrated yet decomposed optimization of these five subsystems.

The PS provides the thrust required by the ATA, while the AFS-A supplies the necessary lift for the vehicle to complete the mission and accounts for the resulting drag losses. The ECS and TMS provide the cooling necessary for the dissipation of heat generated by the aircraft during flight. The mission is defined as a set of conditions and requirements that the aircraft is synthesized/designed to accomplish. The mission for this work is defined by the request-for-proposal for an Air-to-Air Fighter (AAF) presented in Mattingly et al. (2002). The proposed mission has 14 different mission segments. The PS must provide enough power to accommodate the rates of climb and acceleration and overcome the vehicle's drag as well as provide the power required to run all of the remaining subsystems. The overall aircraft performance is significantly affected by the

thermodynamic performance of the on-board subsystems primarily through heat source interactions. The aircraft can be exposed to either internal or external sources of heat. The cooling systems in modern aircraft (ECS and TMS) face a number of challenges produced by high-speed flight and internal heat loads due to avionics and the engine (PS).

The ATA system was optimized using conceptual and time decomposition techniques along with ILGO for a total of 493 (with AFS-A degrees of freedom) or 481 (without AFS-A degrees of freedom) synthesis/design and operational decision variables. These variables consist of a combination of integer and continuous variables. The believed global optimum value for the total gross takeoff weight of the aircraft, W_{TO}, is obtained through seven iterations of ILGO for the case with AFS-A degrees of freedom. An improvement of 13.07% in the value of the gross takeoff weight is obtained between the first and second ILGO iterations. The final gross takeoff weight at the seventh ILGO iteration is lowered by 2920 kg from the result of the first iteration, which is a 28.68% decrease in W_{TO}. For the case without AFS-A degrees of freedom, a significant improvement in the gross takeoff weight is again reached between the first and second ILGO iterations. The final gross takeoff weight at the seventh ILGO iteration is lowered by 2110 kg from the result of the first iteration, which is a 23.28% decrease in W_{TO}. The final gross takeoff weights for each case are considered to be the global optimums.

The optimum values for the ATA AFS-A geometric variables for the cases with and without AFS-A degrees of freedom are compared in Table 2.6. As can be seen in this table, the optimized vehicle with AFS-A degrees of freedom has a 6.3% lower gross takeoff weight than the optimized vehicle without AFS-A degrees of freedom. Therefore, the additional degrees of freedom in the AFS-A improve the overall optimum of the W_{TO} objective function, and provide a more optimal AFS-A geometry.

In the work done by Mattingly et al. (2002) the best gross takeoff weight for the AAF where only the engine design was optimized is given as 23,800 lb_f. In Rancruel and von Spakovsky (2003, 2005) where the entire vehicle is optimized an optimum gross takeoff weight of 22,396 lb_f was found, which is 1404 lb_f (5.9%) lighter. Rancruel and von Spakovsky attribute this result to the integrated optimization of all of the subsystems of the aircraft (AFS-A, PS, ECS, and TMS) as well as the large number of degrees of freedom (491/483) which were employed. The optimum solution they found also had an

11% lighter fuel weight and a 6.7% lower thrust-to-weight ratio at takeoff in comparison to the results found in Mattingly et al. (2002).

Table 2.6: AFS-A optimum geometries with and without AFS-A degrees of freedom (Rancruel and von Spakovsky, 2003, 2005).

	Optimum with AFS-A optimization	**Optimum without AFS-A optimization**
W_{TO}/S_{ref}	61.49	64.3
T_{SL}/W_{TO}	1.13	1.27
W_{TO}, kg	10180 (22396 lbf)	10818 (23800 lbf)
S_{ref} (ft^2)	364.2	378.87
T_{SL}, kg	11503 (25306 lbf)	13045 (28700 lbf)
W_{fuel} (kg)	3270 (7194 lbf)	3580 (7876 lbf)
W_{AFS} (kg)	3100	3348
Wing AR	3.046072	2.80
Wing t/c	0.077494	0.11
Wing λ	0.240061	0.3
Wing Λ	31.05784	39.06
Wing	0.75	0.75
Wing	0.5	0.6
Tail	5.004859	4.5
Tail T_t/c	0.12	0.1
Tail T_λ	0.461185	0.4

The significance of the work of Rancruel and von Spakovsky is that it shows that in addition to exergy-based methods, the use of large-scale optimization for the integration aircraft system synthesis/design is desirable and possible through the use of intelligently developed and applied decomposition strategies such as ILGO.

Chapter 3

Overall Model Description and Synthesis/Design Problem Definition

3.1 Problem Definition

The problem of synthesis/design for an advanced military fighter aircraft system consists of developing a set of thermodynamic, kinetic, geometric and aerodynamic models of varying fidelity which can be used to simulate, analyze and optimize the aircraft system as a whole as well as its subsystems and components as individual entities. Two separate fighter aircraft system models will were developed in this thesis work: a morphing-wing aircraft model and a fixed-wing aircraft model. These system models consist of the two major subsystems which comprise the aircraft: a turbojet engine Propulsion Subsystem (PS) and an Airframe Subsystem-Aerodynamics (AFS-A). These subsystems for each of the system models are identical except for the feature incorporated in the morphing-wing aircraft system model that allows the wing geometries to change as flight conditions change during the aircraft mission.

The AFS-A provides the required amount of lift to carry out the mission which, of course, results in an associated drag. The PS provides the thrust necessary for overcoming the aircraft's drag and the accelerations or changes in altitude required by the mission. The mission is the set of specified flight conditions, maneuvers, and associated requirements for which the vehicle is to be synthesized/designed. The models presented in this report are flown computationally through the Request for Proposal (RFP) mission for an Air-to-Air Fighter (AAF) presented in Mattingly et al. (2002). The mission consists of 13 different segments each with its own unique set of flight conditions and requirements. A detailed description of the mission is presented in Figure 3.1 and Tables 3.1 and 3.2.

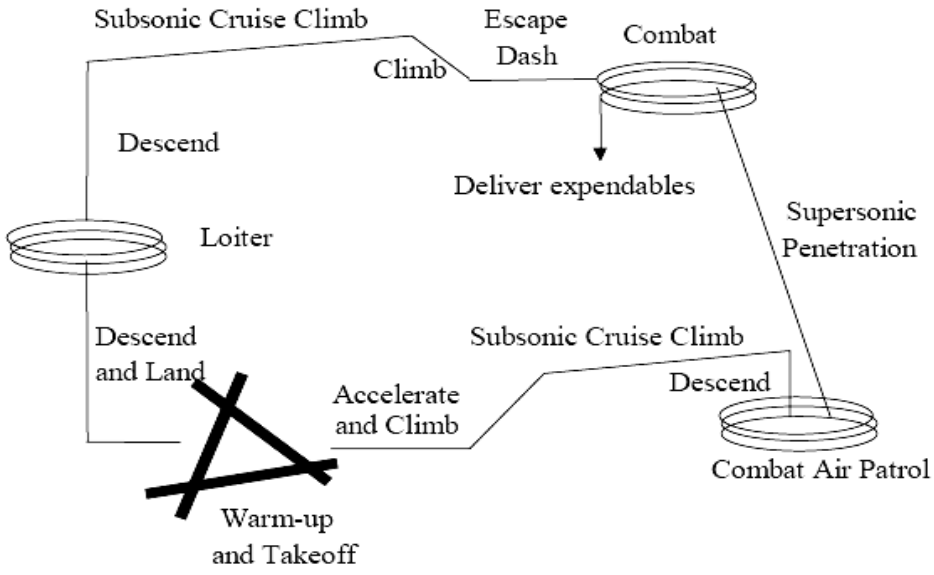

Figure 3.1: Mission profile by phases (Mattingly et al., 2002).

.

Table 3.1: Performance requirements/constraints (Mattingly et al., 2002).

Item	Requirements/Constraints
Payload	• 2 AMRAAM missiles (148 kg each) • 2 AIM-9L missiles (87 kg each) • 500 rounds of 25 mm ammo (522 kg fixed weight (cannon, ammunition casings, etc.), 125 kg spent ammunition)
Performance	• Max. Mach number: 2.0 @ 12,200 m altitude • Acceleration: 0.8 to 1.6 M/9150m at less than 5 sec • Sustained g level: n = 5 at 0.9 M/9150m
Crew	One 90 kg pilot plus equipment
Fuel	JP-4
Engine	One engine - Turbojet

Table 3.2: AAF mission specifications (Mattingly et al., 2002).

Phase	Description
1	Warm-up and take-off at 600 m pressure altitude and T = 310 K. The fuel allowance is 5 min at idle power for taxi and 1 min at military power for warm-up. Take-off roll plus rotation must be = 450 m on the surface with a friction coefficient of 0.05. $V_{TO} = 1.2V_{STALL}$
2	Accelerate to climb speed and perform a minimum time to climb at military power to best cruise mach number and best cruise altitude (BCM/BCA).
3	Subsonic cruise/climb at BCM/BCA until total range for cruise climb is 280 km.
4	Descend to 9150 m .
5	Perform combat air patrol loiter for 20 min at 9150 m and Mach number for best endurance.
6	Supersonic penetration at altitude 9150 m and M = 1.5 for 185 km.
7	Combat segment model: • Combat Turn 1: M = 1.6, one 360 degree 5g turn at maximum power • Combat Turn 2: M = 0.9, two 360 degree 5g turns at maximum power • Accelerate from M = 0.8 to M = 1.6 at maximum power and t < 50s • Deliver expendables: 2 AMRAAM missiles, 2 AIM-9L missils and ½ ammunition Conditions at end of combat are M = 1.5 at 9150 m.
8	Escape dash at M = 1.5 and altitude 9150 m for 46 km.
9	Minimum time climb from 1.5M at 9150m to BCM/BCA.
10	Subsonic cruise climb at BCM/BCA for a range of 278 km.
11	Descend to 3000 m.
12	Loiter at 9150 m for 20 min at Mach number for best endurance.
13	Descend and land at 600 m pressure altitude and T = 310K. Free roll and breaking must be < 450 m on surface with coefficient of friction = 0.18. $V_{TD} = 1.15V_{STALL}$

In order to properly define the synthesis/design problem for the specified mission, the mission presented in Figure 3.1 and Tables 3.1 and 3.2 must be divided into a number of mission segments. These mission segments are presented in order in Table 3.3. It is these mission segments which are used to simulate the flight of both the fixed-wing aircraft system with fixed AFS-A geometry and the morphing-wing aircraft system with variable AFS-A geometry for each of the syntheses/designs considered in arriving at the final optimal synthesis/design for each type of aircraft.

Table 3.3: AAF mission segments (Mattingly et al., 2002).

Mission Segments		
No.	**Name**	**Abbreviation**
1	Warm up	WARM
2	Take off	TO
3	Subsonic Acceleration 1	SUBA1
4	Subsonic Acceleration/Climb	SUBACL1
5	Subsonic Cruise 1	SUBC1
6	Combat Air Patrol/Loiter	LOI1
7	Subsonic Acceleration 2	SUBA2
8	Transonic Acceleration 1	TRANA1
9	Supersonic Acceleration 1	SUPA1
10	Supersonic Penetration	SUPC1
11	Combat Turn 1	CT1
12	Combat Turn 2	CT2
13	Subsonic Acceleration 3	SUBA3
14	Transonic Acceleration 2	TRANA2
15	Supersonic Acceleration 2	SUPA2
16	Deliver Expendables	DEL
17	Escape Dash	SUPC2
18	Supersonic Climb	SUPCL1
19	Transonic Climb	TRANCL1
20	Subsonic Cruise 2	SUBC2
21	Loiter	LOI2
22	Landing	LAND

3.2 Airframe Subsystem – Aerodynamic (AFS-A) Model

The AFS-A is that portion of the empty aircraft, which includes the wings, fuselage, tail, landing gear, etc. The AFS-A does not include cargo weights such as fuel, the pilot, equipment, or the payload, which are all taken into accounted for separately. This subsystem has two primary characteristics of interest, namely, its shape/geometry and its resulting weight. The AFS-A must be shaped in such a way that the lift it produces counter-balances the weight of the aircraft and must furthermore be coupled to

the PS in such a way that the aerodynamic drag of the AFS-A contributes to the performance requirements or constraints of the PS.

3.2.1 Aerodynamics

The first step in understanding the aerodynamics of an aircraft is to perform a force balance on the vehicle. In general, the aircraft is subject to four body forces during flight, which are thrust, drag, lift, and weight as shown in Figure 3.2.

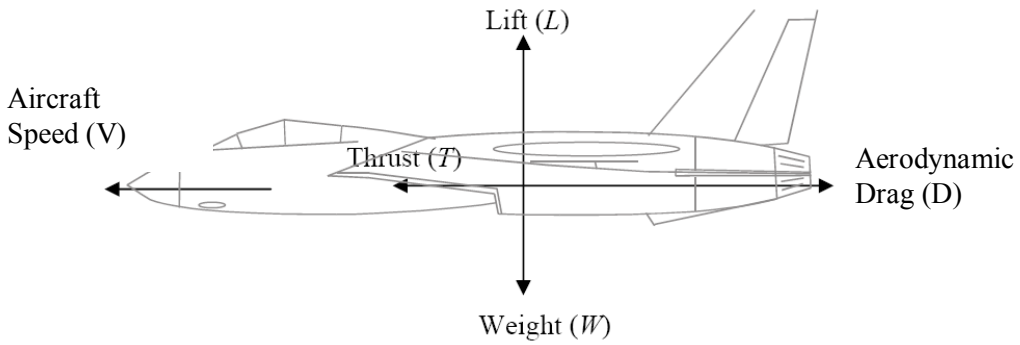

Figure 3.2: Aircraft force balance diagram (Mattingly et al., 2002).

An energy rate balance on the aircraft yields the following expression:

$$(T - D)V = W\frac{d}{dt}\left(h + \frac{V^2}{2g}\right) \tag{3.1}$$

where h is the altitude and g is the acceleration due to gravity. This equation shows that the thrust required to fly the aircraft must equal the drag forces experienced by the aircraft plus the rates of change of potential and kinetic energies. Note that the aerodynamic drag, D, represents both the induced drag due to aircraft lift and the parasitic drag due to skin friction and other residual effects. Since the weight of the aircraft is subject to change during flight due to fuel burned and payload deployed, it is redefined as $W = \beta W_{TO}$, where W_{TO} is the gross take-off weight of the aircraft and β is the weight fraction of the aircraft with respect to the gross take-off weight. The value of the thrust force, T, also changes during flight due to changing mission requirements and aircraft weight as well as the surrounding air properties as the aircraft changes altitude and speed. Thus, the thrust term is also defined by $T = \alpha T_{SL}$, where T_{SL} is the corresponding thrust

force at sea level and α is the thrust lapse term. Information for installed engine thrust lapse from existing performance data is used in Mattingly et al. (2002) to create a correlation for thrust lapse estimation. The corresponding correlation for a turbojet engine at military power is given by the following expression:

$$\alpha = 0.8\delta_o \left\{1 - 0.16\sqrt{M}\right\} \tag{3.2}$$

where δ_o is the non-dimensional total pressure at altitude given by the expression

$$\delta_o = \delta\left(1 + 0.2M^2\right)^{\frac{\gamma}{\gamma-1}} \tag{3.3}$$

Here, M is the free stream Mach number, δ is the dimensionless static pressure, and γ is the ratio of specific heats of air. Applying the expressions for thrust and weight given above to equation (3.1), the energy rate balance equation becomes

$$\frac{T_{SL}}{W_{TO}} = \frac{\beta}{\alpha}\left[\frac{D+R}{W_{TO}\beta}\right] + \frac{1}{V}\frac{d}{dt}\left(h + \frac{V^2}{2g}\right) \tag{3.4}$$

This form of the energy balance equation is more useful for aircraft flight analysis since the weight and thrust terms are defined by take-off and sea-level conditions, respectively. The lift and drag forces that are experienced by the aircraft during flight are typically defined by the following well-known relationships:

$$L = nW = qC_L S \tag{3.5}$$

and

$$D = qC_D S \tag{3.6}$$

where S is the planform area of the wing, q is the free stream dynamic pressure, and n is the load factor, which is a multiple of the acceleration perpendicular to the velocity vector of the aircraft due to gravity applied to the wing. The free stream dynamic pressure term is defined as

$$q = \frac{1}{2}\rho V^2 \tag{3.7}$$

where V is the free stream speed and ρ is the air density at a given altitude. The C_L and C_D which appear in equations (3.5) and (3.6) are the coefficients of lift and drag and are the means by which the aerodynamic properties of the aircraft are described.

Aerodynamic Coefficients

The relationship between the lift and drag coefficients is typically described by the lift-drag polar equation found, for example, in Mattingly et al. (2002), Raymer (1999), Anderson (1999), and Nicolai (1975) and defined by the following expressions:

Un-cambered $$C_D = K_1 C_L^2 + C_{D_0} \tag{3.8}$$

Cambered $$C_D = K_1 \left(C_L - C_{L\min\_drag}\right)^2 + C_{D_{\min}} \tag{3.9}$$

where

$$C_{D_0} = C_{D_{\min}} + K'' C_{L\min\_drag}^2 \tag{3.10}$$

C_{D_0} is the parasitic drag, which is the drag coefficient at zero lift. K_1 is called the induced drag factor. For high-performance uncambered aircraft, $C_{L\min\_drag} \approx 0$. For the purposes of this study, the wing is considered to be uncambered.

Parasitic (Zero-Lift) Drag

The parasitic drag term represents drag due to skin friction, form (or profile) drag, and wave drag (for supersonic flight). Skin friction occurs as air molecules move across the aircraft's surface during flight. The molecules closest to the skin act as if they are stuck to the surface, moving with the aircraft (no-slip condition). This creates a shear effect between the stationary molecules and the molecules moving with the aircraft producing a boundary layer with shear force effects. The force required to accelerate the boundary layer of air in the direction of travel is considered the drag due to skin friction. Form (or profile) drag is the resulting pressure difference that must be overcome by the aircraft due to viscous separation effects during flight. Wave drag occurs as the aircraft enters the supersonic flight regime due to the formation of shocks. These various types of parasitic drag can be collectively expressed as follows:

Subsonic $$C_{D_0} = C_{D_{\min}} = C_{fe} \frac{S_{wet}}{S_{ref}} \tag{3.11}$$

Supersonic $$C_{D_0} = C_{fe} \frac{S_{wet}}{S_{ref}} + C_{D_{wave}} \tag{3.12}$$

where C_{fe} is the coefficient of friction, S_{wet} is the wetted area of the aircraft, S_{ref} is the exposed wing area, and C_{Dwave} is the coefficient of drag due to the formation of shocks in supersonic flight.

The Equivalent Skin Friction Method in Raymer (1999) is used to calculate the parasitic drag during subsonic flight. During subsonic flight, the parasitic drag is mostly skin friction drag with a small amount of form drag due to separation. The form drag is generally a consistent percentage of the skin friction drag for different classes of aircraft. This produces the concept of an equivalent skin friction coefficient that takes into account both skin friction and form drag. Equivalent skin friction coefficients for a variety of different types of aircraft are presented in Table 3.4. The equivalent skin friction coefficient chosen for the AFS-A model here is C_{fe}= 0.0035.

Table 3.4: Equivalent skin friction coefficients (Raymer, 1999).

$C_{Do} = C_{fe} \frac{S_{wet}}{S_{ref}}$	C_{fe} -subsonic
Bomber and civil transport	0.0030
Military cargo (high upsweep fuselage)	0.0035
Air Force Fighter	0.0035
Navy Fighter	0.0040
Clean supersonic cruise aircraft	0.0025
Light aircraft-single engine	0.0055
Light aircraft-twin engine	0.0045
Prop seaplane	0.0065
Jet seaplane	0.0040

For supersonic flight, all form or pressure drag contributions are included in the wave drag coefficient term, which is determined from the aircraft's volume distribution. The skin friction contribution during supersonic flight is considered to be the skin friction coefficient of a flat plate times the wetted area ratio. The flat plate coefficient of friction, C_f, depends on the Reynolds number, Mach number, and skin roughness of the aircraft. The skin friction coefficient is most heavily influenced by whether the flow across the aircraft is laminar or turbulent. Coefficients of friction for turbulent flow cases can be up to three times higher than those in the laminar regime. The expressions used to calculate the coefficient of friction over a flat plate are given as

Laminar $$C_f = 1.328/\sqrt{\mathrm{Re}} \tag{3.13}$$

Turbulent: $$C_f = \frac{0.455}{(\log_{10} \mathrm{Re})^{2.58}(1+0.144M^2)^{0.65}} \tag{3.14}$$

where Re is the Reynolds number defined as

$$\mathrm{Re} = \rho V \ell / \mu \tag{3.15}$$

The "ℓ" term is the characteristic length, which for a fuselage is equal to the total length, while for a wing or tail is equal to the mean chord length. If the surface of the aircraft is relatively rough, the coefficient of friction may be higher than indicated by equations (3.13) and (3.14). This is taken into account by using the cut-off Reynolds number given by

Subsonic $$\mathrm{Re}_{cutoff} = 38.21\left(\frac{\ell}{k}\right)^{1.053} \tag{3.16}$$

Supersonic $$\mathrm{Re}_{cutoff} = 44.62\left(\frac{\ell}{k}\right)^{1.053} M^{1.16} \tag{3.17}$$

where k is the skin roughness factor ($k = 1.015\text{x}10^{-5}$ for a smooth painted surface). If the actual Reynolds number is greater than the cut-off Reynolds number, the cut-off Reynolds number is used in its place for the skin friction calculations.

Wave Drag

To account for the pressure drag due to shock formation at supersonic speeds, a wave drag coefficient, C_{Dwave}, is included into the parasitic drag expression in equation (3.12). The wave drag in supersonic flight is often greater than all of the other forms of drag combined and is a direct result of the aircraft's volume distribution. An ideal volume distribution is described by the Sears-Haack body as defined by

$$\frac{r}{r_{\max}} = \left[1-\left(\frac{x}{(\ell/2)}\right)^2\right]^{0.75} \tag{3.18}$$

where ℓ is the longitudinal dimension and r is the cross-sectional radius of the body, r_{max} is the maximum cross-sectional radius of the body, and x is the longitudinal position on the body. The Sears-Haack body as defined above has a wave drag value given by

$$\left(\frac{D}{q}\right)_{Sears-Haack} = \frac{9\pi}{2}\left(\frac{A_{\max}}{l}\right)^2 \tag{3.19}$$

where A_{max} is the maximum cross-sectional area of the Sears-Haack body. Wave drag at a Mach number of 1.0 is minimized when the aircraft volume distribution is identical to that of the Sears-Haack body. Thus, the wave drag of an aircraft can be reduced as the volume distribution is changed to better resemble the Sears-Haack distribution, i.e. the aircraft has a minimal amount of longitudinal curvature.

No realistic aircraft will have a volume distribution identical to that of the Sears-Haack body, but a well designed supersonic aircraft will have a theoretical wave drag value of about twice the Sears-Haack value at Mach 1.0. For preliminary wave drag analysis at Mach numbers greater than 1.2, a correlation to the Sears-Haack body wave drag can be used to estimate the wave drag, i.e.,

$$\left(\frac{D}{q}\right)_{wave} = E_{WD}\left[1 - 0.386(M-1.2)^{0.57}\left(1 - \frac{\pi\Lambda_{LE}^{0.77}}{100}\right)\right]\left(\frac{D}{q}\right)_{Sears-Haack} \tag{3.20}$$

where Λ_{LE} is the leading-edge sweep angle, E_{WD} is an empirical wave drag efficiency factor which is typically between 1.8 and 2.2 for a supersonic fighter aircraft. For supersonic flight at Mach numbers less than 1.2 the wave drag is estimated as about twice the theoretical Sears-Haack wave drag value. Note that the fineness ratio value ($A_{\max}/\ell$) is an essential geometric quantity for reducing the wave drag of the aircraft. This term is squared, which explains why reducing the maximum cross-sectional area (A_{max}) provides far better drag reduction than just smoothing the volume distribution without lowering A_{max}. The wave drag coefficient is thus given by

$$C_{D_{wave}} = \frac{(D/q)_{wave}}{S} \tag{3.21}$$

which is consistent with the lift and drag coefficient definitions provided by equations (3.5) and (3.6). Figure 3.3 illustrates the complete build up of the different parasitic drag components versus Mach number for subsonic, transonic, and supersonic flight. This

figure makes it evident that the parasitic drag increases greatly and is dominated by the wave drag component as the aircraft leaves subsonic and enters supersonic flight.

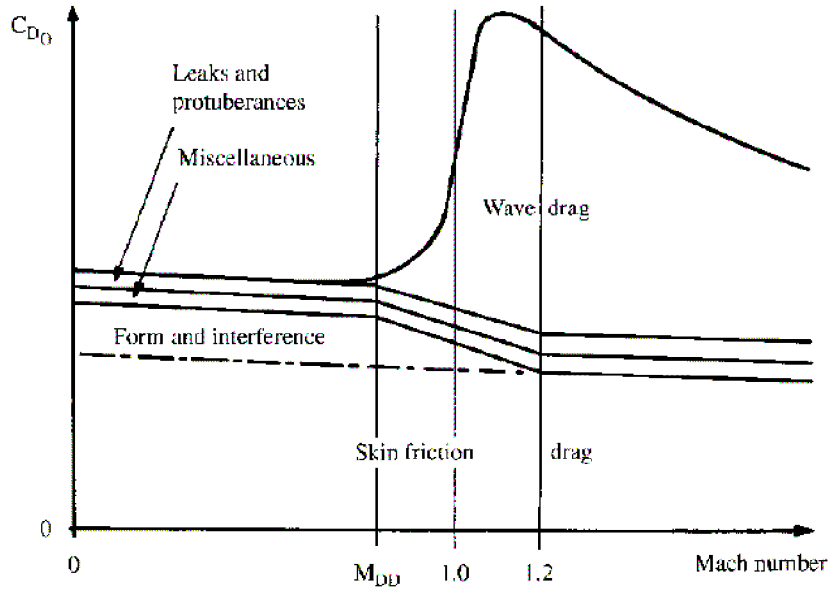

Figure 3.3: Build up of parasitic drag versus Mach number (Raymer, 1999).

Induced Drag

Induced drag is the drag component that is caused by the creation of lift due to the shape of the wings of an aircraft. At moderate angles of attack, the induced drag is proportional to the square of the lift coefficient multiplied by the induced drag factor, K_1. For subsonic flight, the induced drag factor can be estimated using the Weissinger Span Efficiency Method from Nicolai (1975) presented in equation (3.22). This method uses a span efficiency factor to predict the relationship between the lift and drag coefficients. Thus,

Subsonic $$K_1 = \frac{1}{\pi e AR} \tag{3.22}$$

where AR is the aspect ratio of the wing and e is the Weissinger span efficiency. The aspect ratio is an aerodynamic parameter defined as $AR = b^2/S$ where b is the wing span.

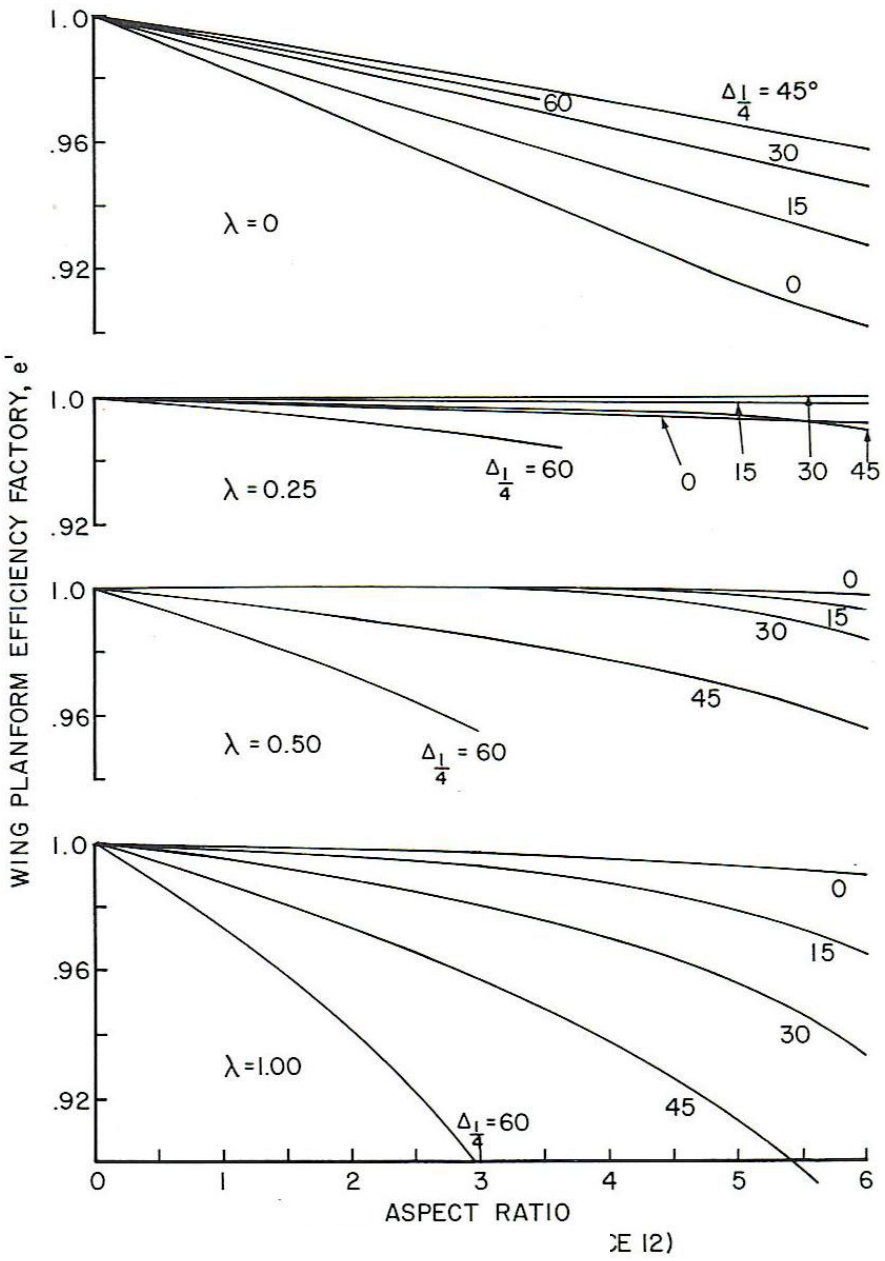

Figure 3.4: Weissinger wing planform efficiency factor (Nicolai, 1975).

The span efficiency, e, is calculated using the wing planform efficiency charts presented in Nicolai (1975) and shown in Figure 3.4. These charts can calculate the span efficiency of the wing depending on the aerodynamic parameters of the taper ratio (λ), quarter chord sweep angle ($\Delta_{1/4}$), aspect ratio, fuselage diameter, and the wing span.

It is more difficult to predict the induced drag factor during supersonic flight. For supersonic flight segments, the Leading Edge Suction Method from Raymer (1999) is

used to predict the induced drag factor. Figure 3.5 illustrates the concepts behind the Leading Edge Suction Method. The airfoil on the left is at an angle of attack below that at which substantial separation occurs. The flow stream line curves rapidly to follow the leading edge radius over the top of the wing. The rapid curvature creates

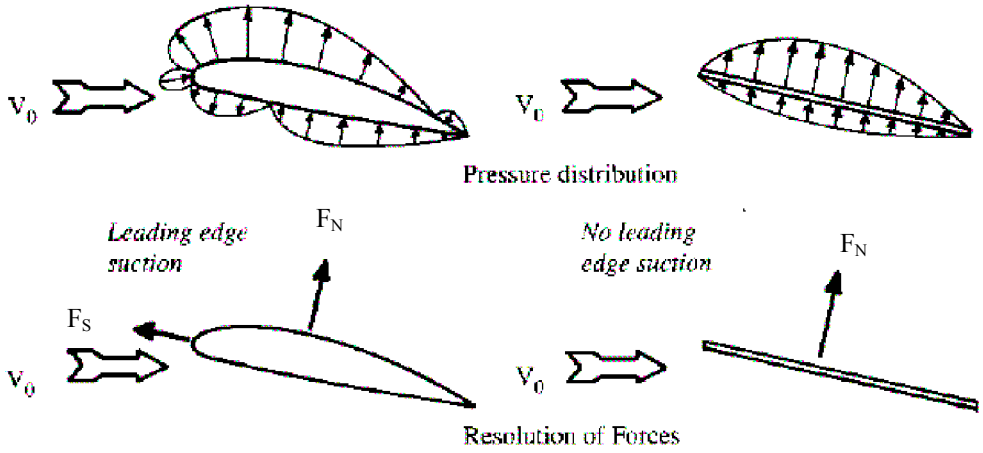

Figure 3.5: Leading edge suction definition (Raymer, 2000).

a pressure drop on the upper side of the leading edge creating a suction force. The leading edge suction force, F_S, is shown on the left side of the figure and is perpendicular to the normal force, F_N. The leading edge suction force balances the horizontal component of the normal force. This case represents 100% leading-edge suction. On the right side of Figure 3.5 there is a zero thickness flat-plate airfoil. In this case there is no leading-edge suction component to counter balance the horizontal component of the normal force. Therefore, the vertical and horizontal components of the normal force are equal to the lift and induced drag components of the wing. Thus,

$$L = F_N \cos\alpha \tag{3.23}$$

$$D_i = F_N \sin\alpha = L \tan\alpha \tag{3.24}$$

$$C_{D_i} = C_L \tan\alpha \tag{3.25}$$

and for small angles of attach α

$$C_{D_i} = K_1 C_L^2 \cong \alpha C_L \tag{3.26}$$

Thus, for supersonic flight, the induced drag factor is

Supersonic $$K_1 = \frac{\alpha C_L}{C_L^2} = \frac{\alpha}{C_L} = \frac{1}{C_{L\alpha}} \tag{3.27}$$

where $C_{L\alpha}$ is the lift curve slope, D_i is the induced drag and C_{D_i} is the induced drag coefficient. Thus, for zero leading edge suction, the induced drag factor is the inverse of the lift curve slope. This is how the induced drag factor will be determined for supersonic flight. It can be seen from equation (3.27) that higher lift curve slopes tend to give lower induced drag factors so that the overall drag experienced by the aircraft is reduced.

For a purely supersonic wing, the lift curve slope is given by

$$C_{L\alpha} = \frac{4}{\beta} \tag{3.28}$$

where $$\beta = \sqrt{M^2 - 1} \tag{3.29}$$

when $$M > \frac{1}{Cos\Lambda_{LE}} \tag{3.30}$$

Unfortunately, this is generally not the case during most flight regimes. For a mixed flow wing (i.e. supersonic and subsonic flows are present), which is generally the case for high Mach number sweep wings, it is more difficult to predict the lift curve slope. Predicting the lift curve slope in mixed flow cases can be done using a series of databases or charts. Thus, in this thesis work the lift curve slope, $C_{L\alpha}$, is determined using the supersonic normal force curve slope charts presented in Raymer (1999), Nicolai (1975), and Anderson (1999). These charts provide, for a given wing type and taper ratio, the lift curve slope given the wing's aspect ratio, taper ratio, leading-edge sweep angle, and the free stream Mach number. An example of one of these charts is presented in Figure 3.6 for a taper ratio of $\lambda = 0.20$. The term β divided by the tangent of the leading-edge sweep angle, Λ_{LE}, appears on the horizontal axis on the left-hand side of the chart. If this value is greater than 1.0, it must be inverted and the right-hand side of the chart must be used. The chart actually provides the slope of the normal force coefficient, $C_{N\alpha}$, which is the lift curve slope in a direction perpendicular to the wing. This value is approximately equal to the lift curve slope for low angles of attack, which is usually the case for supersonic flight.

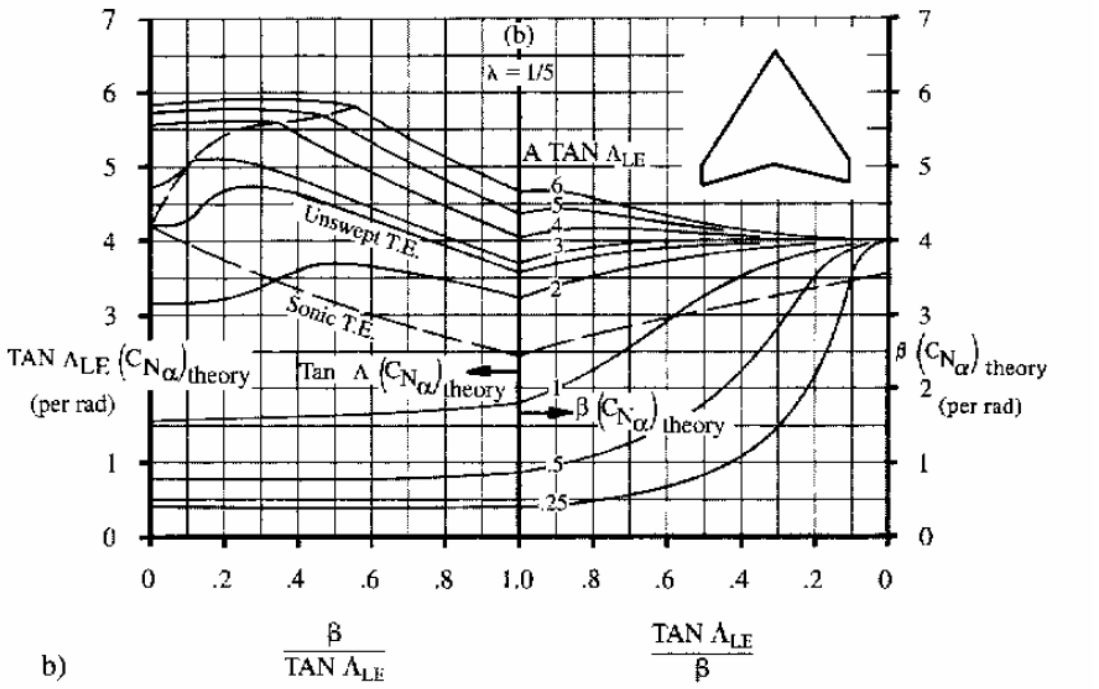

Figure 3.6 Supersonic normal force curve slope chart (Raymer, 1999).

Minimizing the induced drag created by the wing is one of the key benefits to be considered with the morphing-wing aircraft. The induced drag factor, K_1, is heavily dependent on the wing geometries (i.e. aspect ratio, taper ratio, wing span, planform area) in both the subsonic and supersonic flight realms. Allowing the wing to change to an optimum geometry on each of the different mission segments can significantly reduce any losses due to irreversibilities and dramatically affect the performance of the aircraft.

Exergy Analysis

In this thesis work, the only irreversibilities considered for the AFS-A are those due to drag losses during flight. Therefore, all of the exergy destroyed (entropy generated) by the AFS-A is a result of aerodynamic drag. In order to distinguish the types of exergy destruction the rate of exergy destroyed by the AFS-A is separated into parasitic and induced drag sources. The former is determined as follows:

$$\dot{E}x_{DES_{Parasitic}} = \frac{T_0 D_0 V}{T} \tag{3.31}$$

with

$$D_0 = qC_{Do}S \tag{3.32}$$

where T is the atmospheric temperature, and T_0 is the "dead state" temperature user in the exergy calculations. The exergy destruction rate due to induced drag is given by

$$\dot{E}x_{DES_{Induced}} = \frac{T_0 D_i V}{T} \tag{3.33}$$

where

$$D_i = qC_{Di}S \tag{3.34}$$

3.2.2 Constraint Analysis

Combining the energy rate equation (equation (3.1)) with the drag-polar equation (equation (3.8)) yields the constraint equation (equation (3.35)) or "Master Equation" as described in Mattingly et al. (2002). This equation describes the constraints of the aircraft during flight in terms of the take-off thrust loading, (T_{SL}/W_{TO}), and the takeoff wing loading, (W_{TO}/S), i.e.

$$\frac{T_{SL}}{W_{TO}} = \frac{\beta}{\alpha}\left[\frac{K_1 n^2 \beta}{q}\left(\frac{W_{TO}}{S}\right) - 2K_1 n C_{L\min} + \frac{q\left(K_1 C_{L\min}{}^2 + C_{D_o} + C_{D_{wave}}\right)}{\beta\left(\frac{W_{TO}}{S}\right)}\right] + \frac{1}{V}\frac{d}{dt}\left[h + \frac{V^2}{2g}\right] \tag{3.35}$$

The master equation changes (i.e. reduces to special cases) during flight depending on the requirements and constraints of each mission segment. A set of curves are created for each mission segment, and these curves in turn define the constraint space within which the aircraft must be synthesized/designed to meet all of the mission requirements and constraints. Since an un-cambered airfoil is assumed here, the lift coefficient at minimum drag, C_{Lmin}, is neglected, i.e. minimum drag is assumed to be at zero lift.

When initially performing the constraint analysis for a given mission, the actual weight fraction, β, is not known. An initial value for β for each mission is needed during preliminary synthesis/design and this is typically done with values based on experience (i.e. regression data from existing aircraft and new technology considerations). The actual values of β are found during the weight fraction analysis, which requires a thrust specific fuel consumption (*TSFC*) value from the PS. The constraint analysis is then

updated using the new weight fraction values, and an iterative process is used to continually update these values until they converge to on the true weight fraction for each mission segment.

The actual constraint space for synthesis/design determined for a constraint analysis that is formed by the most stringent (or constrained) mission segments that the aircraft must meet. Upon completion of the constraint analysis, an aircraft synthesis/design point can be determined for the take-off thrust loading (T_{SL}/W_{TO}) and the take-off wing loading (W_{TO}/S). An example of a complete constraint analysis for an AAF is given in Mattingly et al. (2002) shown in Figure 3.7. The feasible values for the take-off thrust loading and the take-off wing loading are located in the so-called "synthesis/design space", which is shaded gray in the constraint diagram.

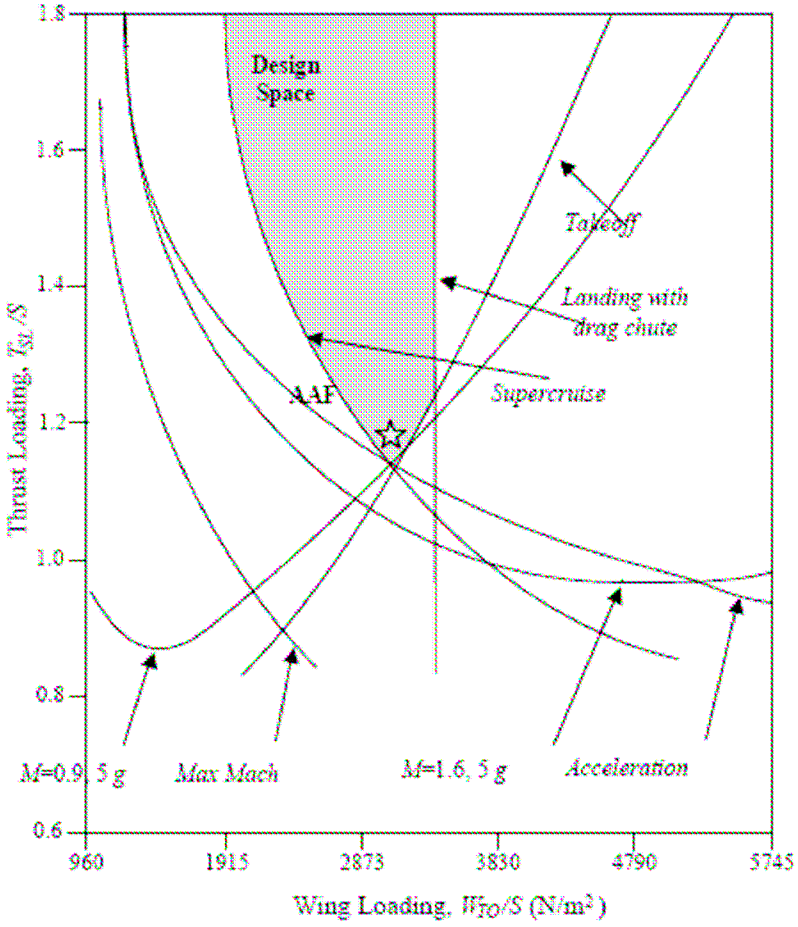

Figure 3.7: Complete air-to-air fighter constraint diagram (Mattingly et al., 2002).

To demonstrate how the constraint analysis concept works using the master equation (equation (3.35)), a supersonic turn mission segment is used as an example. Using the requirements and constraints from the AAF mission specification given earlier, the aircraft is required to perform one 360 degree 5g turn at Mach 1.6 and an altitude of 9150 m. Since there is no change in altitude or speed during the turn, the master equation reduces to

$$\frac{T_{SL}}{W_{TO}} = \frac{\beta}{\alpha}\left\{ K_1 n^2 \frac{\beta}{q}\left(\frac{W_{TO}}{S}\right) + \frac{C_{Do}}{\frac{\beta}{q}\left(\frac{W_{TO}}{S}\right)} \right\} \tag{3.36}$$

This reduced version of the master equation creates one of the curves on the constraint diagram and for this example is solved using the standard parameter values given in Table 3.5.

Table 3.5: Parameter values for the example mission segment.

β	α	n	C_{Do}	K_1	q (lb_f/in^2)
0.78	0.7481	5	0.028	0.30	1128

Substituting these parameters into the reduced master equation further reduces the equation to be solely a function of the take-off thrust loading (T_{SL}/W_{TO}) and the take-off wing loading (W_{TO}/S), i.e.

$$\frac{T_{SL}}{W_{TO}} = 5.407\times10^{-3}\left(\frac{W_{TO}}{S}\right) + \frac{42.22}{\left(\frac{W_{TO}}{S}\right)} \tag{3.37}$$

The resulting values and corresponding constraint curve for the supersonic turn mission segment can be viewed in Table 3.6 and Figure 3.8.

Table 3.6: Supersonic turn constraint analysis data.

W_{TO}/S (psf)	20	40	60	80	100	120
T_{SL}/W_{TO}	2.22	1.27	1.03	0.960	0.963	1.00

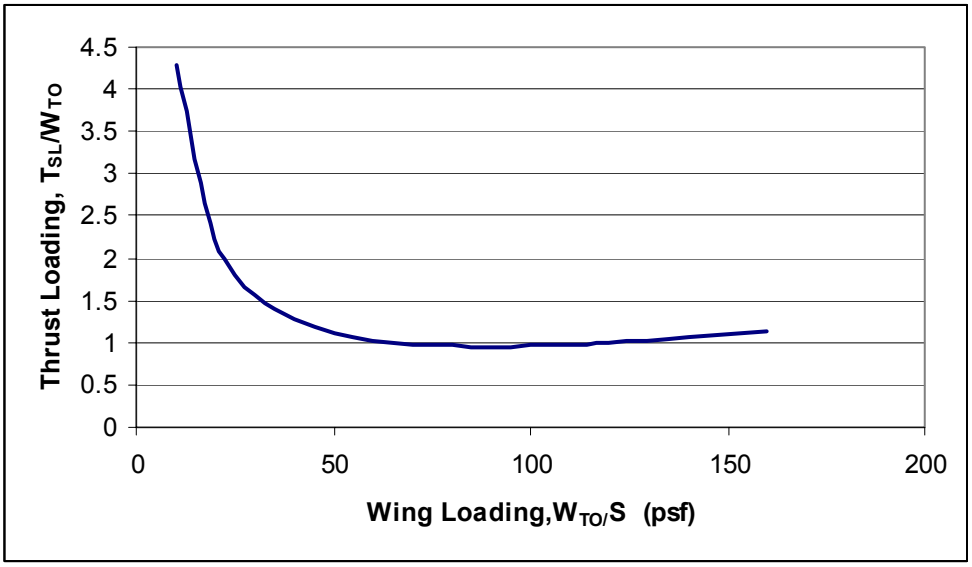

Figure 3.8: Constraint curve for supersonic turn mission segment.

Constraint analyses similar to the one presented above must be performed for every mission segment to produce a constraint diagram such as the one shown in Figure 3.7. The goal of the constraint analysis is to find the lowest possible thrust loading and corresponding wing loading. For example for the supersonic turn mission segment example shown here the smallest thrust loading values occur between wing loadings of 50 – 100 psf. Furthermore, note that as the synthesis/design of the aircraft changes during the synthesis/design process, the constraint diagram changes as well. In a conventional trade-off analysis, this may represent a few to tens of such diagrams. In an optimization process, this may represent hundreds to tens of thousands of such diagrams.

3.2.3 Morphing-Wing Considerations

The overall goal of the morphing-wing aircraft is to allow for its wings to change shape during flight to enhance performance for specific mission segments. In order to properly model the wing-morphing characteristics, geometric wing variables need to be chosen that best describe and change the aerodynamic characteristics of the wing. These geometric parameters become the synthesis/design and operational design variables of the airframe system for the synthesis/design problem.

First, the geometric parameters that directly affect the aerodynamics of the wing must be identified. The induced drag factor (equations (3.22) and (3.27)) are functions of the aspect ratio (AR), taper ratio (λ), leading edge sweep angle (Λ_{LE}), quarter chord sweep angle ($\Lambda_{1/4}$), and wing span (b) all of which are geometric parameters. The master equation is heavily dependent on the induced drag factor as well as the wing loading, which is dependent on the wing planform area (S). These geometric parameters are the basis for defining the aerodynamic qualities of the aircraft.

Unfortunately, each of these geometric parameters is coupled with at least one or more of the other geometric parameters that contribute to the aerodynamics of the wing. The aspect ratio is a direct function of the wing span and the planform area ($AR = b^2/S$). The taper ratio affects both the leading edge and quarter chord sweep angles, and the sweep angles can affect the value of the wing span. Therefore, it was decided to break these variables into more basic parameters to create uncoupled geometric parameters for the morphing-wing synthesis/design problem.

AR, λ, Λ_{LE}, $\Lambda_{1/4}$, S, and b can all be described in terms of the more basic geometric parameters of the wing sweep angle (Λ), the wing length (L), the root chord length (C_r), and the tip chord length (C_t). A visual depiction of these parameters is displayed in Figure 3.9.

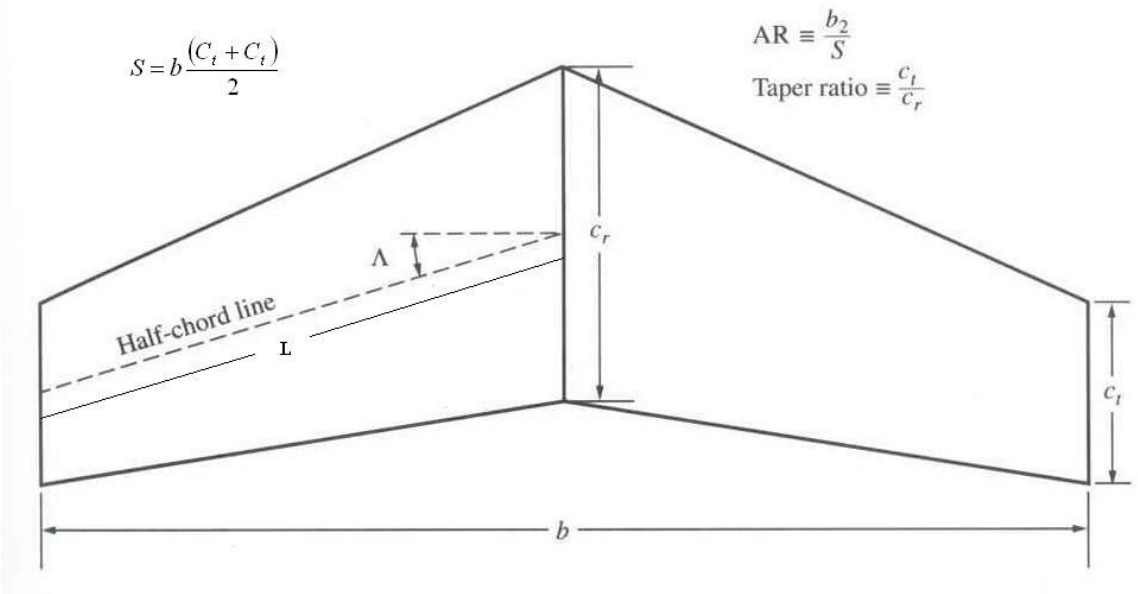

Figure 3.9: Diagram of morphing-wing basic geometric parameters (Nicolai, 1975).

In order to simplify the geometric calculations in the AFS-A model, the initial synthesis/design wing sweep angle is set to zero degrees. Therefore, a straight wing without any sweep is designed, but wing sweep allowable as an operation setting during flight. This simplification makes the planform area, leading edge sweep angle and the quarter chord sweep angle calculations straightforward. With the design sweep angle set to zero, the planform area is no longer a function of the wing span but of the wing length. The trapezoidal shaped wing has a planform area of

$$S = L(C_t + C_r) \tag{3.38}$$

Note that the planform area of the wing is calculated for both wing sections, not just one side. The taper ratio is simply the tip chord length divided by the root chord length (C_t/C_r) and is generally a value between 0 and 1. The wing span is dependent on both the wing length and the sweep angle, i.e.

$$b = 2L\cos\Lambda \tag{3.39}$$

Most aerodynamic calculations require the leading edge or quarter chord sweep angles instead of the actual wing sweep angle. The leading edge and quarter chord sweep angles are calculated as follow:

$$\Lambda_{LE} = \tan^{-1}\left(\frac{C_r - C_t}{2L}\right) + \Lambda \tag{3.40}$$

and

$$\Lambda_{1/4} = \tan^{-1}\left(\frac{C_r - C_t}{4L}\right) + \Lambda \tag{3.41}$$

Again, the aspect ratio is simply calculated as $AR = b^2/S$. Any of the geometric parameters found in literature can now be derived given the basic parameters of the wing sweep angle, the wing length, the root chord length, and the tip chord length. These are used as the synthesis/design and operational variables for the AFS-A synthesis/design optimization problem.

Finally, no reliable information is currently available for the weight and energy consumption of the actuators and other mechanical devices needed to perform in-flight wing morphing with the use of smart materials and adaptive structures. Due to this lack of information, the aircraft model uses penalty factors to account for the additional

weight and energy used, which a morphing wing requires. A 3% fuel penalty is initially used to account for the extra energy consumption and a 15% weight penalty to account for the extra wing weight due to the actuators. These fuel and weight penalties are then varied from 3% to 100% and 15% to 800%, respectively, to explore the sensitivities to the synthesis/design which the parasitic effects involved with wing morphing have.

3.2.4 Mission Analysis (Weight Fractions and Sizing Considerations)

Once a synthesis/design point for the take-off thrust loading (T_{SL}/W_{TO}) and the take-off wing loading (W_{TO}/S) have been established, the next step is to determine the scale of the aircraft by computing the gross take-off weight, W_{TO}. This is done by flying the aircraft through the AAF mission. The gross take-off weight is the sum of the weight of the empty aircraft (W_E), the payload weight (W_P), and the fuel weight (W_{FUEL}) given by

$$W_{TO} = W_E + W_P + W_{FUEL} \tag{3.42}$$

The weight of the empty aircraft consists of the airframe and the permanent equipment (i.e. engines, avionics, etc.) and can be expressed as

$$W_E = W_{AFS} + W_{PS} + W_{Other} \tag{3.43}$$

where W_{AFS} is the weight of the AFS-A (wing, fuselage, etc.), W_{PS} is the weight of the PS, and W_{Other} is the remaining weight of all the other miscellaneous equipment. Initially, an estimate of the empty aircraft weight is used to fly the mission, i.e.

$$\frac{W_E}{W_{TO}} = 2.34 W_{TO}^{-0.13} \tag{3.44}$$

The empty weight is then recalculated by flying the mission to more accurately determine the gross take-off weight.

The payload weight can be divided into two parts, the expendable payload weight, W_{PE}, (i.e. ammunition, missiles) and the permanent payload weight, W_{PP} (i.e. crew, equipment). The overall gross take-off weight equation, thus, becomes

$$W_{TO} = W_{AFS} + W_{PS} + W_{Other} + W_{PE} + W_{PP} + W_{FUEL} \tag{3.45}$$

The fuel weight, W_{FUEL}, onboard the aircraft gradually decreases during the mission since it is being consumed in the PS. With exception to the expendable payload

delivery, the decrease in the weight of the aircraft occurs at the exact rate of the decrease in the weight of the fuel. The rate of fuel consumption is determined from the required thrust, T, and the thrust specific fuel consumption, $TSFC$, of the engine. The thrust can be determined at any point using the master equation (equation (3.35)). The $TSFC$ depends on the engine settings, the flight conditions, and the performance demands.

Weight Fraction

The following discussion will cover the calculation of the weight fractions (Π) needed for each of the mission segments. The fuel consumption analysis is based on calculations that require relatively little information. It also points to the best way of flying certain mission segments for minimum fuel usage. The fuel expended in each segment is expressed as a ratio of the weight at the beginning of each segment.

Calculating the fuel consumption rate of the aircraft is done using the differential equation

$$\frac{dW}{dt} = -\frac{dW_{FUEL}}{dt} = -TSFC \times T \tag{3.46}$$

This equation can be rewritten as

$$\frac{dW}{W} = -TSFC\frac{T}{W}dt = -TSFC\frac{T}{W}\frac{ds}{V} \tag{3.47}$$

The thrust work produced by the engine (i.e. the product of the thrust and the vehicle speed, V) is consumed by the change in the mechanical energy of the aircraft (increasing or decreasing kinetic or potential energy) or is dissipated to the environment by losses due to aerodynamic drag. The differential weight equation (equation (3.47)) can now be integrated to obtain the weight fractions (W_f/W_i) for each of the mission segments. The proper integration of the equation requires knowledge of the $TSFC$ and the instantaneous thrust loading is given by

$$T/W = (\alpha/\beta)\ (T_{SL}/W_{TO}) \tag{3.48}$$

as a function of time along the flight path. The integration can be carried out by two distinct cases corresponding to the weight specific excess power, P_S, i.e. as $P_S > 0$ or $P_S = 0$.

The $P_S > 0$ case generally requires specific information regarding the amount of installed thrust applied and the total changes in altitude, h, or vehicle speed, V, that take place, but not the distance or time involved. This case includes acceleration segments, climb segments, or a combination of the two.

The $P_S = 0$ case involves constant speed and altitude flight segments and information regarding total distance or time elapsed is required. In these cases, all of the engine thrust work is consumed by dissipation to the atmosphere through aircraft drag phenomena. The $P_S = 0$ cases are generally constant-speed cruise and loiter mission segments.

The integration of each of the weight specific excess power cases produces the following weight fraction expressions

$$\frac{W_f}{W_i} = \exp\left\{ \frac{-TSFC}{V\left(1-\frac{D}{T}\right)} \Delta\left(h + \frac{V^2}{2g}\right) \right\} \qquad (P_S > 0) \tag{3.49}$$

also, $$\frac{W_f}{W_i} = \exp\left[-TSFC\left(\frac{D}{W}\right)\frac{\Delta s}{V} \right] = \exp\left[-TSFC\left(\frac{D}{W}\right)\Delta t \right] \qquad (P_S = 0) \tag{3.50}$$

where Δs is the total distance traveled for the mission segment, and Δt is the total mission segment flight time.

The engine installed *TSFC* is a complex function of altitude, speed, and throttle setting. The *TSFC* is a value communicated from the PS to the AFS-A during the flight of the vehicle. If no *TSFC* information is initially available from the PS, it can be estimated using an equation obtained from Mattingly et al. (2002), namely

$$TSFC = (1.1 + 0.30M)\sqrt{\theta} \tag{3.51}$$

where θ is the atmospheric temperature ratio based on atlitude and M is the vehicle Mach number. This equation predicts the *TSFC* for a typical turbojet engine running at the military power throttle setting. Table 3.7 shows the weight ratio equations for the different types of mission segments.

Table 3.7: Weight ratio calculations for different mission segments.

Case	$\Pi = W_{final}/W_{initial}$
Constant speed climb	$\exp\left\{\frac{-TSFC}{V}\left[\frac{\Delta h}{1-\frac{D}{T}}\right]\right\}$
Horizontal acceleration	$\exp\left\{\frac{-TSFC}{V}\left[\frac{\Delta(V^2/2g)}{1-\frac{D}{T}}\right]\right\}$
Climb and acceleration	$\exp\left\{\frac{-TSFC}{V}\left[\frac{\Delta(h+V^2/2g)}{1-\frac{D}{T}}\right]\right\}$

There is one case that does not use the typical weight ratio calculations, i.e. the delivery of expendable payload segment. If the delivery is done at some point j in the mission, the weight fraction for this segment becomes

$$\frac{W_j - W_{PE}}{W_j} = 1 - \frac{W_{PE}}{W_j} \tag{3.52}$$

In order to differential the weight fractions for each of the different mission segments, the following notation is used.

$$\frac{W_f}{W_i} = \prod_{i\_f} \leq 1, \tag{3.53}$$

Thus, the fuel consumed can be written as

$$W_{FUEL} = W_{TO}\left(1 - \prod_{i=1}^{n}\right) - W_{PE}\left(1 - \prod_{i=j}^{n}\right) \tag{3.54}$$

where n is the total number of mission segments. The weight fractions depend on the PS and AFS-A, the required thrust, ambient conditions, the aerodynamics, and additional factors, such as payload, ammunition, fuel weight, etc.

Algebraic manipulation of equation (3.54) using equation (3.42) and the definition $W_P = W_{PE} + W_{PP}$ yields the following expression for the gross take-off weight:

$$W_{TO} = \frac{W_{PP} + W_{PE}\prod_{j\_n}}{\prod_{1\_n} - \frac{W_E}{W_{TO}}} \tag{3.55}$$

Equation (3.55) allows for a straightforward calculation of the gross take-off weight. It also gives insight into the dependence of the gross take-off weight on the weight ratios, the expendable and permanent payloads, and the empty weight.

The gross take-off weight estimation of the aircraft can be improved through the use of sizing techniques. For the AFS-A, sizing calculations are done for the fuselage and wing of the aircraft. For the present model, equations found in Raymer (1999) based on applied statistical regression analysis were used to estimate the different component weights as follows:

$$W_{wing} = 0.0103 K_{dw} K_{vs} (W_{dg} N_z)^{0.5} S_w^{0.622} AR^{0.785} (t/c)_{root}^{-0.4} (1+\lambda)^{0.005} (\cos\Lambda)^{-1} S_{csw}^{0.04} \tag{3.55}$$

and

$$W_{fuselage} = 0.499 K_{dw} W_{dg}^{0.35} N_z^{0.25} L^{0.5} D^{0.849} W^{0.685} \tag{3.56}$$

where K_{dw} is the delta wing factor, K_{vs} is the sweep wing factor, W_{dg} is the gross design weight, N_z is the ultimate load factor, S_w is the trapezoidal wing area, t/c_{root} is the root thickness to chord ratio, and S_{csw} is the control surface area. After the component weights are estimated using this method, they are summed to determine the actual empty aircraft weight. This new empty weight calculation replaces the estimated empty weight calculated in equation (3.44) and better accuracy of the weight calculations is achieved.

3.3 Propulsion Subsystem (PS)

The PS used in this thesis work is a single-spool turbojet engine with an afterburner. The decision was made to use this engine instead of a more complex design (i.e. turbofan) in an effort to minimize the number of operational decision variables included in the synthesis/design process (synthesis/design and operational design variables as is total over 120 variables). Including the additional variables would introduce a number of additional degrees of freedom for a synthesis/design process that is already overburdened and may have issues reaching a truly optimized solution in a timely

manner. The single-spool turbojet engine was also chosen for the propulsion system since it gives a more conservative estimate of morphing-wing versus fixed-wing performance since fuel consumption and exergy destruction rates in comparison with the higher efficiency turbofan engine are higher.

3.3.1 Engine Layout and Component Definition

A schematic diagram of a single-spool turbojet engine with its accompanying T-s cycle is shown in Figure 3.10. Air from the atmosphere enters the engine

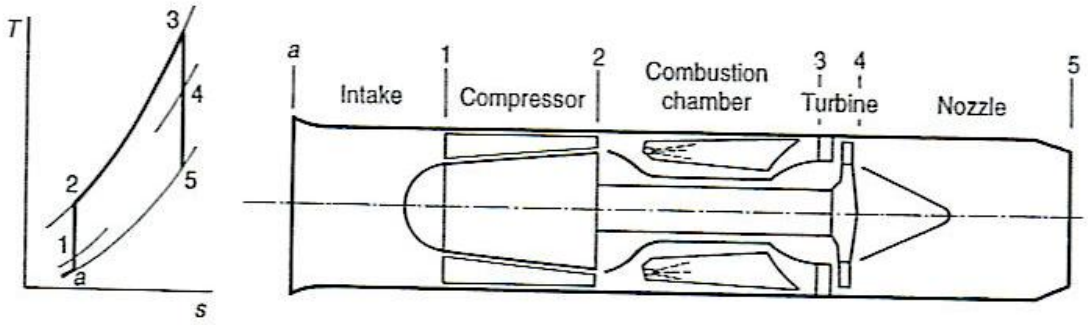

Figure 3.10: Simple turbojet engine and ideal cycle (Saravanamuttoo, Rogers, and Cohen, 2001).

through the intake and flows into the diffuser where it is decelerated to a relatively low velocity. The air from the diffuser enters the compressor where it is compressed to a very high pressure. The compressed air then enters the combustion chamber where it mixes with fuel and combusts to produce a high pressure, high temperature gas mixture. The gas mixture then enters the turbine where enough work is extracted from the gas by the turbine to operate the compressor and other on-board subsystems. The turbine and compressor are directly coupled through the spool or shaft of the turbojet. The exhaust gas exits the turbine at a high velocity and enters the afterburner (see Figure 3.11). At certain flight conditions the afterburner is used as a second combustion chamber where additional fuel is burned to create greater thrust. In essence the afterburner further increases the temperature of the exhaust gases, which increases their velocity and the engine's overall thrust. Finally, the exhaust gases enter the propulsion nozzle where the gas velocity is further increased as it exits the engine.

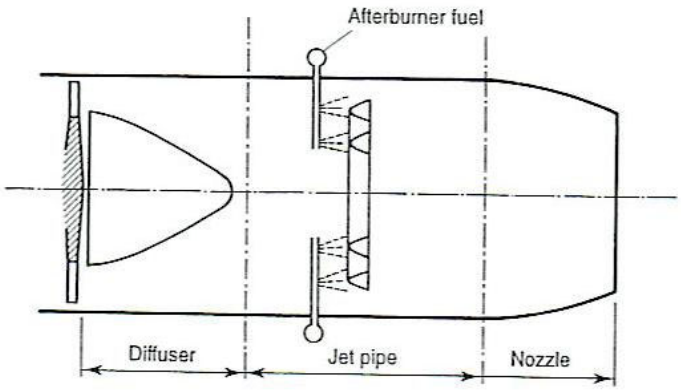

Figure 3.11: Afterburner and propelling nozzle subsystem (Saravanamuttoo, Rogers, and Cohen, 2001).

Table 3.8: Station numbering and locations for PS.

Station	Location
0	Free stream
1’	Intake/diffuser
1	Compressor inlet
2	Compressor exit/combustor inlet
3	Combustor exit/turbine inlet
4	Turbine exit
4’	Afterburner
5	Propelling nozzle

The station numbers and component locations of the engine considered are listed in Table 3.8 and Figure 3.12. The thermodynamic properties of the gas in each of the engine components are described in terms of pressure and temperature ratios of the exit vs. inlet values (e.g., P_2/P_1 and T_2/T_1). For the rotating machinery components (turbine or compressor), it is generally convenient to relate the pressure and temperature ratios using isentropic efficiency values. The isentropic efficiencies account for the component losses and real effects based on industry experience. For the components where combustion occurs, combustion efficiency is used to estimate the percentage of the fuel entering the combustion chambers which burns. These efficiencies are based on a ratio of the actual temperature rise in the component to the maximum possible thermal energy release as characterized by the lower heating value (LHV) of the fuel.

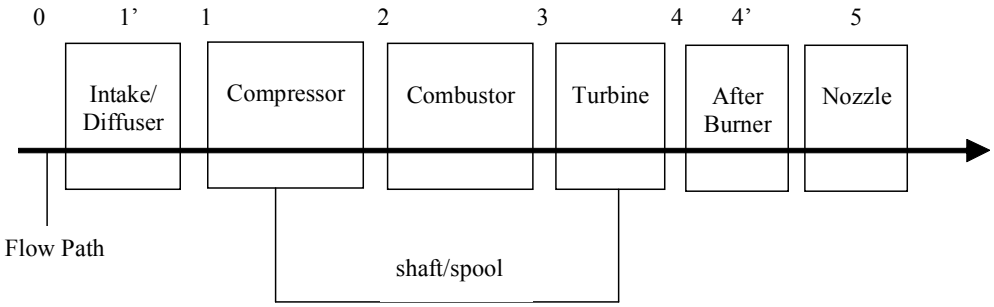

Figure 3.12: Reference stations and components of the PS.

3.3.2 Thermodynamic Model

In order to model the PS, a number of assumptions are made to simplify the analysis. They are as follow:

- The flow is steady through all engine components
- The flow is one-dimensional at the entry and exit of each component
- The compressor is driven by the turbine with the assumption of a constant mechanical efficiency
- The combustors are subject to a constant combustion efficiency
- The intake and nozzle are considered to be isentropic devices

Intake/Diffuser

Air enters the engine intake at the speed of the aircraft and at atmospheric conditions (temperature, pressure, etc.) given by the International Standard Atmosphere (ISA) tables from Saravanamuttoo, Rogers, and Cohen (2001) as a function of flight altitude. As the air passes into the diffuser, it is decelerated to a relatively low speed before it enters the compressor. The thermodynamic analysis determines the stagnation conditions for the temperature (T_{01}) and pressure (P_{01}) exiting the diffuser or at the compressor inlet as follows (it is assumed the diffuser behaves isentropically, i.e. in this case reversibly and adiabatically):

$$T_{01} = T_a + \frac{V_a^2}{2c_{pa}} \tag{3.58}$$

and

$$P_{01} = P_a \left[1 + \eta_i \frac{V_a^2}{2 c_{pa} T_a} \right]^{\gamma_a / (\gamma_a - 1)} \tag{3.59}$$

where T_a is the atmospheric temperature, P_a is the atmospheric pressure, V_a is the entry speed, c_{pa} is the specific heat of the air (c_{pa} = 1.005 kJ/kg K), γ_a is the specific heat ratio of the air (γ_a = 1.4), and η_i is the intake isentropic efficiency. For the purposes of this study, the intake is considered to behave reversibly (i.e. η_i = 1). The resulting stagnation temperature and pressure set the thermodynamic properties for the air entering the compressor.

Compressor

The compressor is the device used to increase the pressure and temperature of the air stream to properties more suitable for combustion. Given the stagnation temperature and pressure properties of the entering air stream, those for the air exiting the compressor are calculated as follow (note that it is assumed here that PR_{COMP} is known since it is an operational decision variable):

$$P_{02} = P_{01} \frac{P_2}{P_1} = P_{01} PR_{COMP} \tag{3.60}$$

and

$$T_{02} = T_{01} + \frac{T_{01}}{\eta_c} \left[(PR_{COMP})^{(\gamma_a - 1)/\gamma_a} - 1 \right] \tag{3.61}$$

where PR_{COMP} is the pressure ratio of the compressor, and η_c is the compressor isentropic efficiency.

The isentropic efficiency of a given compressor design at off-design is based on the compressor efficiency map provided in Mattingly et al. (2002) and shown in Figure 3.13. For each change in compressor design and capacity, the map is scaled accordingly. This map provides the isentropic efficiency for the compressor when operating off of its design point. The design point of the compressor efficiency map is determined by a set of synthesis/design decision variables; the design pressure ratio of the compressor

($PR_{COMP_{Design}}$) and the design corrected mass flow rate of the compressor ($\dot{m}_{c\_2_{Design}}$). The horizontal axis of the compressor map is the percentage that the operational corrected mass flow rate deviates from the design point corrected mass flow rate. The vertical axis of the compressor map is the percent difference between the operational pressure ratio and the design point pressure ratio of the compressor. The operational corrected mass flow rate for the compressor is calculated as

$$\dot{m}_{c\_2} = \frac{\dot{m}_2 \sqrt{\theta_2}}{\delta_2} \tag{3.62}$$

where $\dot{m}_2$ is the mass flow rate of air exiting the compressor, θ_2 is the ratio of the static temperature of the air exiting the compressor to standard atmospheric temperature (T_{STD} = 288 K), and δ_2 is the ratio of the static pressure of the air exiting the compressor to standard atmospheric pressure (P_{STD} = 1.01 bar).

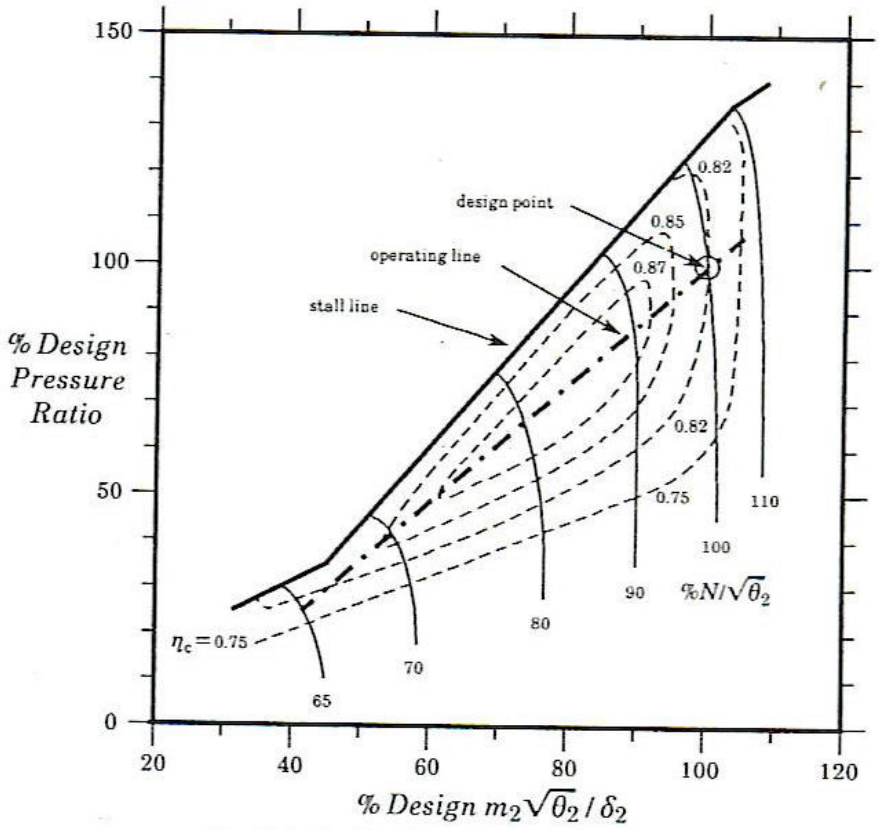

Figure 3.13: Compressor efficiency map (Mattingly et al., 2002).

Unfortunately, both compressor efficiency value and the operational corrected mass flow rate are initially unknown since the operational corrected mass flow, $\dot{m}_{c\_2}$, cannot be calculated without the compressor exit stagnation temperature, T_{02}. To overcome this obstacle an initial guess for the compressor exit stagnation temperature must be determined. This is done by calculating T_{02} first with a standard value for the compressor efficiency fixed at η_c = 0.87. The initial guess for T_{02} is used to calculate a value for $\dot{m}_{c\_2}$, which is then used to calculate a new compressor efficiency value. This process is repeated until the compressor exit stagnation temperature converges.

Finally, a limitation on compressor performance of special concern is the stall or surge line. Steady operation of the compressor above this line is impossible and entering this region even momentarily is dangerous to the engine and the aircraft.

Combustor and Afterburner

The high pressure and temperature air from the compressor enters the combustion chamber where it mixes with fuel and is burned. The amount of fuel added to the combustion process is governed by the fuel-to-air ratio (*f*) which is an operational decision variable in the synthesis/design process. The temperature rise in the combustor is calculated using the chart shown in Figure 3.14.

This figure calculates the combustion temperature rise given the fuel-to-air ratio of the combustion stream and the temperature of the air entering the combustor. The fuel-to-air ratio used in Figure 3.14 assumes that complete combustion occurs. The actual fuel-to-air ratio will be higher since combustion is not complete and it is calculated by

$$f_{act} = \frac{f}{\eta_{COMB}} \tag{3.63}$$

where η_{COMB} is the combustion efficiency. The pressure of the gas leaving the combustion chamber is considered to be the same as the pressure of the air entering it. Since the mass of the fuel added in the combustion process is negligible in comparison to

the mass of the incoming air, the entering and exiting mass flow rates of the combustor are considered to be equal.

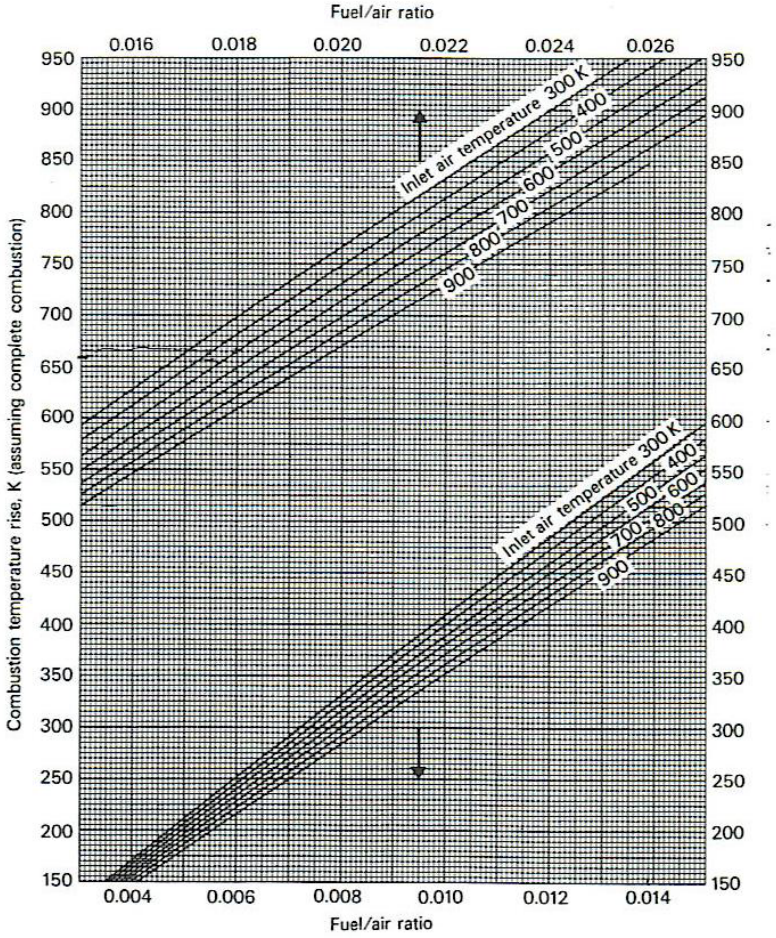

Figure 3.14: Combustor temperature rise versus fuel-to-air ratio (Saravanamuttoo, Rogers, Cohen, 2001).

A design limitation that must be imposed on the combustor is the temperature of the exiting gas. The rotating machinery of the turbine in the following engine stage cannot operate safely with entering gas temperatures about 1778 K. Thus, the temperature of the gas exiting the combustor is not allowed to exceed this value. The combustor is set to have a constant combustion efficiency of 98% ($\eta_{COMB} = 0.98$) as used in the turbojet model proposed in Saravanamuttoo, Rogers, and Cohen (2001). The remaining 2% of the fuel from the combustor is passed through the engine unburned and is lost.

The afterburner is treated as a second combustor located in the engine stage following the turbine. The afterburner is used to generate additional thrust for more demanding mission segments. Much like the primary combustor, the temperature rise in the afterburner is also calculated using Figure 3.14. Since there is no rotating machinery following the afterburner, the exiting combustion temperature is allowed to go as high as 2000 K. The afterburner is also subject to a constant combustion efficiency of 98% with the remaining fuel passing out the back of the engine unburned.

Turbine

The turbine is responsible for providing the power required by the compressor. The shaft which transfers work between the turbine and compressor is subject to a constant mechanical efficiency of 99% ($\eta_M = 0.99$). The mechanical efficiency accounts for the power transfer losses due to windage, bearing friction, and seal drag. Since all of the energy created by the turbine goes to powering the compressor, an energy balance yields

$$W_C = \eta_M W_T \tag{3.64}$$

where

$$W_C = \dot{m}\, c_{pa} (T_{02} - T_{01}) \tag{3.65}$$

and

$$W_T = \dot{m}\, c_{pg} (T_{03} - T_{04}) \tag{3.66}$$

In the equations above c_{pg} is the specific heat of the exhaust gases (c_{pg} = 1.148 kJ/kg K), T_{03} is the temperature of the gases entering the turbine, and T_{04} is the stagnation temperature of the gases exiting the turbine. Combining and rearranging equations (3.64), (3.65), and (3.66) results in an expression to find the stagnation temperature of the gases exiting the turbine, i.e.

$$T_{04} = T_{03} - \frac{c_{pa} (T_{02} - T_{01})}{c_{pg} \eta_M} \tag{3.67}$$

The isentropic stagnation temperature of the gases exiting the turbine can now be calculated using the isentropic turbine efficiency such that

$$T_{04}^{'} = T_{03} - \frac{1}{\eta_{TURB}} (T_{03} - T_{04}) \tag{3.68}$$

where η_{TURB} is the isentropic turbine efficiency. With the value of the isentropic exit temperature of the turbine, the pressure at the exit of the turbine can be calculated as:

$$P_{04} = P_{03}\left(\frac{T_{04}'}{T_{03}}\right)^{\gamma_g/(\gamma_g-1)} \tag{3.69}$$

where γ_g is the ratio of the specific heats of the exhaust gases (γ_g = 1.333).

Much like the isentropic efficiency of the compressor, the isentropic efficiency for a specific turbine design at off-design is calculated using the turbine efficiency map in Figure 3.15 from Mattingly et al. (2002). For each change in turbine design and capacity, the map is scaled accordingly. This map provides the isentropic efficiency of the turbine via the turbine pressure ratio and the degree to which the turbine operates off of the design point. The design point for the turbine efficiency map is set by the design corrected mass flow for the turbine, which is a design decision variable.

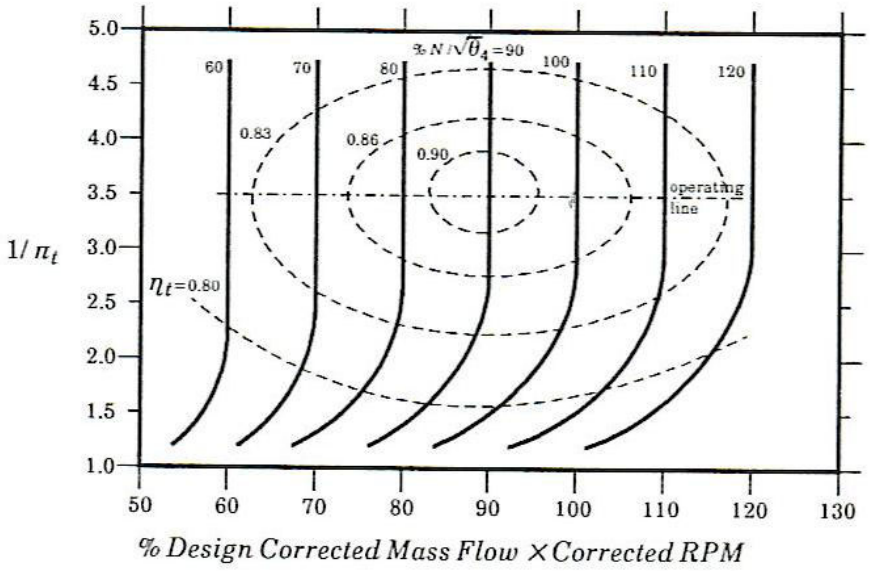

Figure 3.15: Turbine efficiency map (Mattingly et al., 2002).

The horizontal axis of the turbine map is the percentage that the operational corrected mass flow rate deviates from the design point corrected mass flow rate. The vertical axis of the turbine map is the reciprocal of the turbine pressure ratio (i.e. $1/\pi_T = P_{03}/P_{04}$). The operational value for the corrected mass flow rate for the turbine is calculated by

$$\dot{m}_{c\_4} = \frac{\dot{m}_4 \sqrt{\theta_4}}{\delta_4} \tag{3.70}$$

where $\dot{m}_4$ is the mass flow rate of the gas exiting the turbine, θ_4 is the ratio of the static temperature of the air exiting the turbine to the standard atmospheric temperature, and δ_4 is the ratio of the static pressure of the air exiting the compressor to standard atmospheric pressure. Much like the compressor efficiency map, the turbine efficiency map initially has two unknowns; the turbine efficiency value and the turbine pressure ratio, π_T. As a work around for this problem, an initial value of the isentropic turbine exit stagnation temperature, T'_{04}, must be used to calculated to find an initial value for the turbine pressure ratio, π_T. The initial guess for T'_{04} is calculated using a standard value of the turbine efficiency of $\eta_{TURB} = 0.90$. With the calculated initial value of π_T a new turbine efficiency value is found to recalculate T'_{04} and, thus, a new value for π_T. This process is repeated until the turbine pressure ratio value converges.

Exit Nozzle

After the combustion gases exit the turbine or afterburner engine stages, they enter the exit nozzle where the working fluid is expanded close to atmospheric pressure in order to generate a high velocity jet. Thus, the nozzle pressure ratio is given by ratio of the stagnation pressure entering the nozzle to the atmospheric pressure (i.e. P_{04}/P_a). An important consideration for determining the thermodynamic properties of the exit nozzle is to establish whether the flow of the gases in the nozzle is choked or unchoked. This is done by comparing the nozzle inlet stagnation pressure ratio to the critical pressure for choking ($M = 1$) as done in the following expression:

$$\frac{P_{04}}{P_c} = \frac{1}{\left[1 - \frac{1}{\eta_j}\left(\frac{\gamma_g - 1}{\gamma_g + 1}\right)\right]^{\gamma_g/(\gamma_g - 1)}} \tag{3.71}$$

where P_c is the critical pressure and η_j is the isentropic nozzle efficiency. For the purposes of this study, the exit nozzle is considered to behave reversibly (i.e. $\eta_j = 1$). If

$(P_{04}/P_a) > (P_{04}/P_c)$, then the nozzle is considered to be choked. A choked nozzle has the following thermodynamic parameters at the nozzle exit:

$$T_5 = T_c = \left(\frac{2}{\gamma_g + 1}\right) T_{04} \tag{3.72}$$

$$P_5 = P_c = P_{04}\left(\frac{1}{P_{04}/P_c}\right) \tag{3.73}$$

$$\rho_5 = \frac{P_c}{RT_c} \tag{3.74}$$

$$V_5 = \sqrt{\gamma_g RT_c} \tag{3.75}$$

$$\frac{A_5}{\dot{m}} = \frac{1}{\rho_5 V_5} \tag{3.76}$$

where A_5 is the cross-sectional area at 5. If $(P_{04}/P_a) < (P_{04}/P_c)$, then the nozzle is unchoked, and thus $P_5 = P_a$. An unchoked nozzle has the following thermodynamic parameters at the nozzle exit:

$$T_5 = T_{04} - \eta_j T_{04}\left[1 - \left(\frac{1}{P_{04}/P_a}\right)^{(\gamma_g - 1)/\gamma_g}\right] \tag{3.77}$$

$$\rho_5 = \frac{P_a}{RT_5} \tag{3.78}$$

$$V_5 = \sqrt{2c_{pg}(T_{04} - T_5)} \tag{3.79}$$

Note that the thermodynamic properties at the nozzle exit are no longer presented as stagnation properties, but are separated into static and dynamic quantities. The static and dynamic properties are needed for the thrust calculations.

3.3.3 Thrust and Fuel Consumption Calculations

The main purpose of the PS is to provide the thrust required by the AFS-A due to drag, acceleration/deceleration or change in altitude. Once the thermodynamic properties at the inlet and exit of the jet engine are known, the thrust produced by the engine can be calculated with relative ease. A simple schematic of a propulsive duct is shown in Figure 3.16.

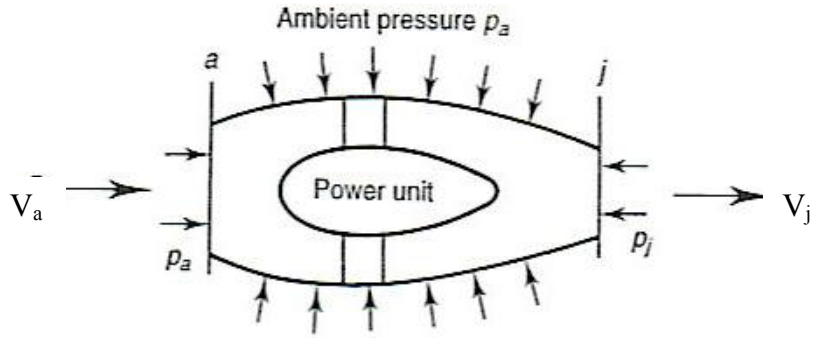

Figure 3.16: Schematic of propulsive duct (Saravanamuttoo, Rogers and Cohen, 2001).

Air enters the propulsive duct with a velocity (V_a) equal and opposite to the speed of the aircraft and the power unit accelerates the air so that it exits at the jet velocity (V_j). The net thrust due to the rate of change of momentum or momentum thrust (T_m) is

$$T_m = \dot{m}(V_j - V_a) \tag{3.80}$$

where $\dot{m}V_j$ is called the gross momentum thrust and $\dot{m}V_a$ is called the intake momentum drag. When the exhaust gases produced in the power unit do not expand completely to the ambient pressure (P_a) in the propulsive duct, the jet pressure (P_j) will be greater than the ambient pressure (i.e. the nozzle is choked). This creates a pressure thrust (T_P) exerted over the jet exit area (A_j) such that

$$T_P = A_j(P_j - P_a) \tag{3.81}$$

Combining the momentum thrust and the pressure thrust from equations (3.80) and (3.81) results in the net thrust (T) given as

$$T = \dot{m}(V_j - V_a) + A_j(P_j - P_a) \tag{3.82}$$

Another important performance parameter for jet engines is the specific thrust (T_s), which is the thrust per unit mass flow of air, i.e.

$$T_s = (V_j - V_a) + \frac{A_j}{\dot{m}}(P_j - P_a) \tag{3.83}$$

This provides an indication of the relative size of engines producing the same thrust since airflow rates generally determine engine dimensions.

The weight fraction calculations in the mission analysis require a fuel consumption rate from the engine in terms of the thrust specific fuel consumption

(*TSFC*). This value can be calculated using the specific thrust as shown in the following expression:

$$TSFC = \frac{g \times f_{act}}{T_s} \tag{3.84}$$

where g is the acceleration due to gravity and f_{act} is the actual fuel-to-air ratio (f/η_{COMB}). *TSFC* is the coupling point between the AFS-A and PS.

3.3.4 Exergy Analysis

The exergy destruction rate $\left(T_0 \dot{S}_{irr}\right)$within a particular component can be determined by performing an exergy rate balance on that component. For either reacting or non-reacting systems, the unsteady exergy rate balance on a lumped parameter basis for a well-defined control volume as shown in figure 3.17 is given by

$$\frac{dEx}{dt} = \sum_{k=0}^{\kappa}\left(1 - \frac{T_0}{T_k}\right)\dot{Q}_k - \dot{W}_S - T_0 \dot{S}_{irr} + \sum_{j=1}^{IN} \dot{m}_j (ex)_j - \sum_{j=1}^{OUT} \dot{m}_j (ex)_j \tag{3.85}$$

where $$ex = h - T_0 s - \mu_0 + \frac{\xi^2}{2} + gz \tag{3.86}$$

and $$Ex = E - T_0 S + P_0 V - \sum_{l=1}^{n} \mu_{l_0} m_l \tag{3.87}$$

In the equations about, h, s, and μ are the specific quantities for enthalpy, entropy, and chemical potential, respectively, while ζ and z represent the speed and elevation of the bulk flows entering and exiting the control volume (Gyftopoulos and Beretta, 1991).

Under steady state conditions, the rate of change of exergy within the system's boundaries $\left(dEx/dt\right)$ is zero. Thus, the amount of exergy present in the system does not change with time. The remaining terms on the right-hand-side of equation (3.85) represent the rates of exergy crossing the system boundary due to work, heat, and mass interactions and the rate of exergy destruction due to the irreversibilities occurring inside the system boundary. Equation (3.85) is, thus, written as

$$0 = \dot{E}x_Q - \dot{W} - \dot{E}x_{DES} + \dot{E}x_i - \dot{E}x_e \tag{3.88}$$

where there is a one-to-one correspondence between the terms on the right-hand-side of this equation and those on the right-hand-side of equation (3.85).

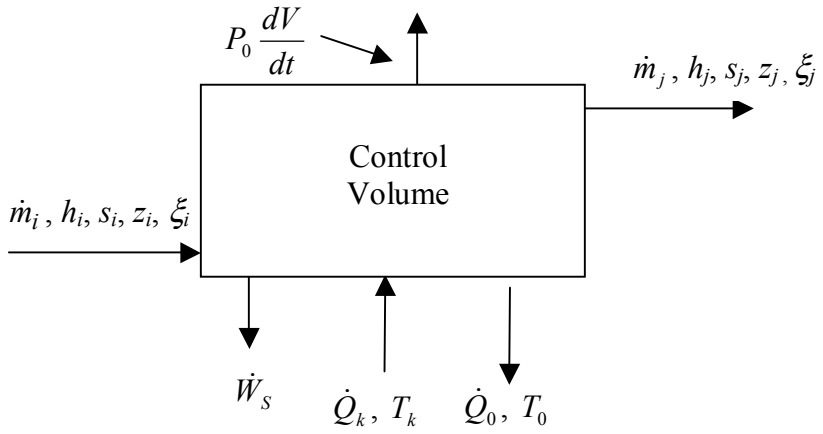

Figure 3.17: Schematic of a system under work, heat, and bulk flow interactions.

Thus, since the rate of irreversibilities occurring within the system is directly proportional to the rate of entropy generation via the "dead state" temperature (T_0), the rate of exergy destruction can be written as

$$\dot{E}x_{DES} = T_0 \dot{S}_{irr} \tag{3.89}$$

while the remaining terms are given by

$$\dot{E}x_Q = \sum_{k=0}^{n} \left(1 - \frac{T_0}{T_k} \right) \dot{Q}_k \tag{3.90}$$

$$\dot{E}x_i = \sum_{j}^{IN} \dot{m}_j \, ex_j \tag{3.91}$$

$$\dot{E}x_e = \sum_{j}^{OUT} \dot{m}_j \, ex_j \tag{3.92}$$

All subsystems and components in the aircraft synthesis/design model developed here are assumed to operate at steady state.

Compressor Exergy Model

The exergy destruction rate for the compressor can be found using the steady state exergy rate balance equation (3.88) such that

$$\dot{E}x_{DES} = \dot{E}x_Q - \dot{W} + \dot{E}x_i - \dot{E}x_e \tag{3.93}$$

Assuming perfect gas behavior and no exergy lost due to heat interactions through the compressor walls, the exergy destruction rate for the compressor reduces to

$$\dot{E}x_{DES_{COMP}} = T_0\,\dot{m}\left[c_{pa}\ln\frac{T_{02}}{T_{01}} - R\ln\frac{P_{02}}{P_{01}}\right] = T_0\,\dot{m}\left[c_{pa}\ln\frac{T_2}{T_1} - R\ln\frac{P_2}{P_1}\right] \tag{3.94}$$

Turbine Exergy Model

Using the same form of the exergy destruction rate derived for the compressor the exergy destruction rate for the turbine is written as

$$\dot{E}x_{DES_{TURB}} = T_0\,\dot{m}\left[c_{pg}\ln\frac{T_{04}}{T_{03}} - R\ln\frac{P_{04}}{P_{03}}\right] = T_0\,\dot{m}\left[c_{pg}\ln\frac{T_4}{T_3} - R\ln\frac{P_4}{P_3}\right] \tag{3.95}$$

Combustor and Afterburner Exergy Model

Since chemical reactions are occurring in these components, the combustor and afterburner exergy model differs from those of the purely mechanical components (compressor, turbine). Consider a system such as the one in Figure 3.18 where a steady state chemical reaction process takes place within the control volume. The system contains 'r' constituents and one overall chemical reaction mechanism takes place (may consist of multiple chemical reaction mechanisms) $\left(\sum_{i=1}^{r}\nu_i A_i = 0\right)$ where ν_i is the stoichiometric coefficient of the i^{th} constituent in the reaction and A_i the chemical compound or element. The bulk mixture flow into the system is denoted by the subscript 'a' while the bulk mixture flow out of the system is denoted by the subscript 'b'. The chemical reaction mechanisms are assumed to only be active within the system boundaries. The overall reaction mechanism for the JP-4 jet fuel that takes place is described as follows:

$$C_{14}H_{11}NO_3 + 16.25O_2 \rightarrow 14CO_2 + 5.5H_2O + NO_2 \tag{3.96}$$

This reaction mechanism governs the chemical combustion reaction taking place in both the combustor and afterburner.

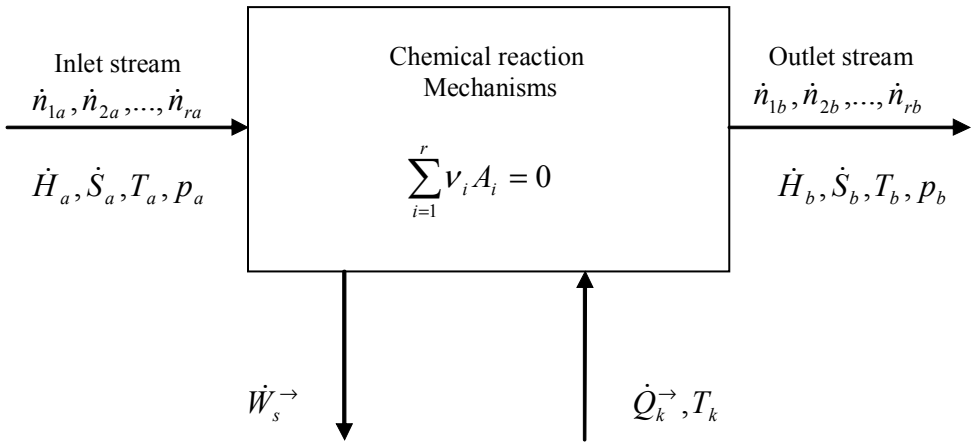

Figure 3.18: Control volume of system with a chemical reaction.

The exergy destruction per mole of reactant mixture for a chemically reacting system and no heat interactions with the surroundings is be written as

$$\dot{E}x_{DES_{Burner}}, \dot{E}x_{DES_{Aft}} = T_0\left(\dot{S}_b - \dot{S}_a\right) \tag{3.97}$$

where

$$\frac{\dot{S}_b - \dot{S}_a}{\dot{n}_a} = (1+\nu\xi)\left[\left(\sum_{i=1}^{r} y_{ib} c_{p_{ii}}\right)\ln\frac{T_b}{T} - R\ln\frac{p_b}{p_o} - R\sum_{i=1}^{r} y_{ib}\ln y_{ib}\right] \tag{3.98}$$

$$-\left[\left(\sum_{i=1}^{r} y_{ia} c_{p_{ii}}\right)\ln\frac{T_a}{T} - R\ln\frac{p_a}{p_o} - R\sum_{i=1}^{r} y_{ia}\ln y_{ia}\right] + \xi\Delta s^{\circ}(T)$$

where the specific heats at constant pressure and the entropy of reaction, Δs^o (T), are on a per mole basis, ξ is the degree of reaction, ν is the sum of the stoichiometric coefficients, the T_a and T_b values are the mixture temperatures, the P_a and P_b are the partial pressures, and T and P_0 the reference temperature and pressure.

Accounting for the Unburned Fuel Lost

The combustion process in the PS is considered have a constant efficiency of 98%. This means that 2% of the fuel introduced to both the combustor and afterburner

passes through the engine and exits through the PS unburned. The loss of unburned fuel represents a loss in exergy since the high quality energy of the fuel does not contribute to the thermal and chemical processes occurring in the PS. The amount of exergy lost due to the unburned fuel is calculated by

$$\dot{E}x_{Unburned} = (1 - \eta_{comb})\dot{m}_{Fuel}\, LHV \tag{3.99}$$

where LHV is the lower heating value of the fuel (JP-4) equal to 45,000 kJ/kg. This expression represents the amount of chemical energy and, thus, approximately the amount of chemical exergy (within a few percentage points) contained by the fuel that is being lost out the backend of the PS.

Chapter 4

System/Subsystem Synthesis/Design Problem Definition and Solution Approach

4.1 AAF System (PS and AFS-A) Synthesis/Design Optimization Problem Definition

Due to the high degree of interdependence between the PS and AFS-A any aircraft synthesis/design process whether based on a traditional trade-off analysis or on mathematical (gradient or heuristic based) optimization, must take the interactions between these two subsystems into account. Thus, determination of the "best" or the "optimal" synthesis/design for the aircraft system requires that the synthesis/design for each of the aircraft subsystems (AFS-A and PS) be accomplished in an integrated fashion.

In this thesis work, a mathematical optimization approach based on heuristics is used to determine the optimal synthesis/design of an AAF (both fixed- and morhing-wing) based on the integrated mission presented in Chapter 3. To examine the effects of different objective functions on the optimal synthesis/designs found, four different optimization objective functions are defined and the results compared. The four objective functions considered are the following:

- Minimization of fuel consumed
- Minimization of the exergy destruction in the PS, including the exergy loss due to unburnt fuel
- Minimization of the exergy destruction for the AFS-A and PS, including the exergy loss due to unburnt fuel
- Maximization of the energy-based thrust efficiency.

4.1.1 Objective Function 1: Global Optimization Problem Definition

The first system-level AAF optimization problem is based on the total amount of fuel consumed over the entire mission and is defined as follows:

Minimize: $W_{FuelBurned} = \sum_{i=1}^{n} W_{FuelBurned,i}$ (4.1a)

w.r.t $\{\vec{x}_{PS}, \vec{y}_{PS}\}, \{\vec{x}_{AFS-A}, \vec{y}_{AFS-A}\}$

subject to

$$\vec{H}_{PS} = \vec{0}, \quad \vec{G}_{PS} \leq \vec{0} \tag{4.1b}$$

$$\vec{H}_{AFS-A} = \vec{0}, \quad \vec{G}_{AFS-A} \leq \vec{0} \tag{4.1c}$$

where the equality constraint represent the thermodynamic, aerodynamic, kinetic and geometric models for each of the subsystems, and the inequality constraint the physical limits placed on the independent (decision) and dependent variables. The subscript *i* denotes a given mission segment, *n* the total number of these segments, and the $\vec{x}$ and $\vec{y}$ the synthesis/design and operational decision variables, respectively, for the PS and AFS-A.

4.1.2 Objective Function 2: Global Optimization Problem Definition

The second system-level AAF optimization problem is based on the exergy destruction and exergy lost due to unburnt fuel over the entire mission and is defined as follows:

Minimize:

$$Ex_{DES/LOSS\_PS} = Ex_{DES_{COMP}} + Ex_{DES_{COMB}} + Ex_{DES_{TURB}} + Ex_{DES_{UNBURNED}} + Ex_{DES_{AFT}} \tag{4.2a}$$

w.r.t $\{\vec{x}_{PS}, \vec{y}_{PS}\}, \{\vec{x}_{AFS-A}, \vec{y}_{AFS-A}\}$

subject to

$$\vec{H}_{PS} = \vec{0}, \quad \vec{G}_{PS} \leq \vec{0} \tag{4.2b}$$

$$\vec{H}_{AFS-A} = \vec{0}, \quad \vec{G}_{AFS-A} \leq \vec{0} \tag{4.2c}$$

4.1.3 Objective Function 3: Global Optimization Problem Definition

The third system-level AAF optimization problem is based on the exergy destruction and exergy loss due to unburnt fuel of the PS and AFS-A is defined as follows:

$$\text{Minimize: } Ex_{DES/LOSS\_TOTAL} = Ex_{DES/LOSS\_PS} + Ex_{DES\_AFS} \tag{4.3a}$$

w.r.t $\{\vec{x}_{PS}, \vec{y}_{PS}\}, \{\vec{x}_{AFS-A}, \vec{y}_{AFS-A}\}$

subject to

$$\vec{H}_{PS} = \vec{0}, \quad \vec{G}_{PS} \le \vec{0} \tag{4.3b}$$

$$\vec{H}_{AFS-A} = \vec{0}, \quad \vec{G}_{AFS-A} \le \vec{0} \tag{4.3c}$$

where $Ex_{DES/LOSS\_PS}$ and Ex_{DES_AFS} are the exergy destruction and exergy loss due to unburnt fuel for the PS and AFS-A given by

$$Ex_{DES/LOSS\_PS} = Ex_{DES_{COMP}} + Ex_{DES_{COMB}} + Ex_{DES_{TURB}} + Ex_{LOSS_{UNBURNED}} + Ex_{DES_{AFT}} \tag{4.4}$$

and $$Ex_{DES\_AFS} = Ex_{DES_{Parasitic}} + Ex_{DES_{Induced}} \tag{4.5}$$

4.1.4 Objective Function 4: Global Optimization Problem Definition

The fourth and final system-level AAF optimization is based on a times weighted average of the energy-based thrust efficiency and is defined as follows:

$$\text{Maximize: } \eta_{Thrust} = \frac{\sum_i \dot{m}_{fuel,i}\, \Delta t_i \eta_i}{\sum_i \dot{m}_{fuel,i}\, \Delta t_i} \tag{4.6a}$$

w.r.t $\{\vec{x}_{PS}, \vec{y}_{PS}\}, \{\vec{x}_{AFS-A}, \vec{y}_{AFS-A}\}$

subject to

$$\vec{H}_{PS} = \vec{0}, \quad \vec{G}_{PS} \le \vec{0} \tag{4.6b}$$

$$\vec{H}_{AFS-A} = \vec{0}, \quad \vec{G}_{AFS-A} \le \vec{0} \tag{4.6c}$$

where η_{Thrust} is the weighted average of thrust efficiency for the overall mission and η_i is the thrust efficiency for a specific mission segment given by

$$\eta_i = \frac{(TV)_i}{\dot{m}_{fuel,i}\, LHV} \tag{4.7}$$

where $(TV)_i$ is the product of the thrust and vehicle speed in a given mission segment, and $\dot{m}_{fuel,i}$ is the flow rate of fuel used for a given mission segment. Note that if either V_i or $\dot{m}_{fuel,i}$ change during a given mission segment, that segment is further subdivided to take into account these changes.

4.2 PS Optimization Decision Variables and Limits

For the optimization of the PS a number of geometric, thermodynamic and aerodynamic parameters are held fixed. These which are not are the synthesis/design and operational decision variables for the PS and these are used in this thesis work are presented in Table 4.1 with their associated constraints or limits.

Table 4.1 PS decision variables and constraints.

Component	**Synthesis/Design Decision Variable**		**Constraint**
Compressor	PR_{COMP}	Design Compressor Pressure Ratio	$10 \le PR_{COMP} \le 30$
	$\dot{m}_{COMP}$	Design Compressor Corrected Flow Rate	$10 \le \dot{m}_{COMP} \le 50$
Turbine	$\dot{m}_{TURB}$	Design Turbine Corrected Flow Rate	$50 \le \dot{m}_{TURB} \le 150$
Component	**Operational Decision Variable**		**Constraint**
Compressor	PR	Compressor Pressure Ratio	$10 \le PR \le 25$
Combustor	f	Fuel-to-air Ratio	$0.007 \le f \le 0.02$
After Burner	f_{aft}	After Burner Fuel-to-air Ratio	$0.007 \le f_{aft} \le 0.02$

4.3 AFS-A Optimization Decision Variables and Limits

As with the PS, certain geometric parameters for the AFS-A are held fixed. These which are not are the synthesis/design and operational variables for the AFS-A. They appear in Table 4.2 along with their associated constraints or limits.

Table 4.2: AFS decision variables and constraints.

Component	Synthesis/Design Decision Variable		Constraint
Wing	L	Wing Length	$30<L<50$ ft
	C_r	Root Chord Length	$5< C_r <15$ ft
	C_t	Tip Chord Length	$0< C_t <15$ ft
Component	**Operational Decision Variable**		**Constraint**
Wing	Λ_{op}	Sweep Angle	$0^o<\Lambda_{op}<60^o$
	L_{op}	Wing Length	30 ft$< L_{op}<L$
	C_{rop}	Root Chord Length	5 ft$< C_{rop}< C_r$
	C_{top}	Tip Chord Length	0 ft$< C_{top}< C_t$

4.4 Solution Approach

4.4.1 Constraint Space

A system's synthesis/design and operational characteristics are represented by a constraint space for which a number of optimization degrees of freedom, i.e. decision variables, can be defined (e.g., see Tables 4.1 and 4.2). These variables, represented by the set of vectors $\vec{x}$ and $\vec{y}$, are used along with a set of dependent variables represented by the vector $\vec{z}$ and appropriate systems of equations and limits to create the constraint space for the system, i.e.

$$\vec{H} = \begin{Bmatrix} \vec{h}_1(\vec{x},\vec{y},\vec{z}) \\ \vec{h}_2(\vec{x},\vec{y},\vec{z}) \\ \vec{h}_3(\vec{x},\vec{y},\vec{z}) \\ \vdots \\ \vec{h}_n(\vec{x},\vec{y},\vec{z}) \end{Bmatrix} = \vec{0} \tag{4.8}$$

$$\text{and} \quad \vec{G} = \begin{Bmatrix} \vec{g}_1(\vec{x},\vec{y},\vec{z}) \\ \vec{g}_2(\vec{x},\vec{y},\vec{z}) \\ \vec{g}_3(\vec{x},\vec{y},\vec{z}) \\ \vdots \\ \vec{g}_n(\vec{x},\vec{y},\vec{z}) \end{Bmatrix} \le \vec{0} \tag{4.9}$$

In equation (4.8), the vector $\vec{H}$ is composed of sub-vectors $\vec{h}_i$, each of which is formulated as an equality constraint analytically describes phenomena usually within the realm of a particular discipline. These are called the state equations or system/subsystem models. The vector $\vec{G}$ formulated as a set of inequality constraints represents the physical limitations imposed on the system. The optimization process consists of finding the optimal values of the $\vec{x}$ and $\vec{y}$ vectors that satisfy the equality constraints within the limits imposed by the inequality constraints. This is an iterative process that becomes more difficult as the sizes of the $\vec{x}$ and $\vec{y}$ vectors increase and as the system of equations (equations (4.8) and (4.9)) become ever more non-linear. Another complicating factor is if $\vec{x}$ and $\vec{y}$ are comprised of both discrete and continuous variables.

Once the system/subsystem models have been established, the optimization subject to a desired set of constraints can be performed. In general terms, the optimization problem is express as

$$\text{Minimize/Maximize } f(\vec{x},\vec{y},\vec{z}) \tag{4.10}$$

with respect to $\vec{x},\vec{y}$ and subject to the following equality and inequality constraints:

$$\vec{H}(\vec{x}) = 0 \tag{4.11}$$

$$\vec{G}(\vec{x}) \le 0 \tag{4.12}$$

All equality constraints are active be definition whereas an inequality constraint $g_j \le 0$ is active if $g_j = 0$. The function $f(\vec{x},\vec{y},\vec{z})$ is called the objective function. A number of different objective functions are used in this thesis work as listed in Section 4.1.

The morphing-wing and fixed-wing AAF's described in this thesis work can be viewed as energy conversion systems. Unfortunately, most energy conversion systems have a number of characteristics that make them difficult to optimize. For example, as presented by Leyland (2002) some of the reasons are that

1. Energy conversion systems are highly nonlinear and, therefore, require relatively robust optimization tools for proper optimization.

2. Energy conversion system models often contain integer or combinational variables, which cause the model to exhibit discontinuous or disjointed behavior. Thus, the optimal surface does not have smooth derivatives (the surface contains a number of jumps) creating several completely different feasible regions, each having its own optimum and with no easy route for passing from one region to another.
3. The optimization algorithm must view the energy conversion system models as a series of "black boxes" (a set of parameters are presented as inputs and the black box provides the outputs without any vision into the process that occurs). Therefore, derivatives of the outputs with respect to the inputs and any extra information about the form of the model are usually unavailable.

If traditional nonlinear programming techniques such as gradient-based methods (which assume continuity in the optimization surface) are used to optimize the system, they will typically be insufficient and will usually find a local optimum that is closest to the starting point.

To overcome the aforementioned difficulties, a series of methods have been developed by means of specialized search schemes. These types of algorithms specialize in performing a complete search of the entire synthesis/design space for possible solutions and are referred to as global search algorithms as mentioned in Rancruel (2002). One of the most popular and highly developed methods for global optimization are Evolutionary Algorithms (EAs), often referred to as Genetic Algorithms (GAs). A GA is utilized in this thesis work as the optimization tool. The following discussion briefly describes GAs, covers the specific GA used in this work, and goes through a simple test problem to demonstrate the GAs characteristics.

4.4.2 Genetic Algorithms (GAs)

GAs are derived from the principles of genetics and Darwin's theory of natural selection**.** The basic elements of natural genetics (crossover, mutation, and selection) are used in the genetic search procedure. The GA begins with an initial set of solutions called the population, and the initial population is used along with the aforementioned

genetic operations to create a "next generation" population that will hopefully yield better results than the previous population. This process repeats itself continuously with the ultimate goal of obtaining the global optimum or some local optimum close to it.

Leyland (2002) discusses the terminology used in GAs, which essentially describes how they operate. A population of individuals (possible solutions to the problem) is evolved toward the solution of an optimization problem by means of natural genetic operations on the population which produce a new generation of individuals and removes the unpromising or "weak" individuals form the populations. The population evolves toward a better solution by how the operators act on the population and how the individuals are removed from the population.

As previously mentioned, crossover and mutation are two natural genetic operations. Crossover involves selecting two or more individuals from a population and creating a child or children that in some way resembles the parents. The parents can be chosen from the better parts of the population to ensure that the offspring reflect the best attributes of the current population. The better parts of the population are determined from the fitness of an individual. In other words, the more suitable an individual is, the better chances the individual has of reproducing. The fitness of an individual is usually a direct reflection of that individual's objective function value. Diversity (i.e. the spread of a population in the search space) is a characteristic of the population which tries to assure that the algorithm does not converge to a local instead of the global or near-global optimum.

Generational, elitist, and steady-state GAs promote three different ways that an individual can be removed from a population. The population is processed a generation at a time in generational GAs (i.e. the number of children generated is equal to the size of the population and completely replaces the previous generation). The elitist GAs generally retain the generational structure; however, a few of the very best individuals from previous populations are retained from generation to generation. The steady-state GAs ignore the generational structure of the algorithm and individuals are added to or removed from the population as necessary; often based on some form of elitism.

Most properly developed GAs are robust optimizers that will solve most classes of problems, and will find a good solution to just about any problem given that they are

run for a long enough period of time. Also, GAs require no additional knowledge of the solution space (i.e. derivatives) and require no initial guesses of the decision variables. In contrast gradient-based optimization methods do require knowledge of derivatives and a base or initial set of decision variable values. Since GAs work with a population of potential solutions, a single optimization run can return a range of solutions, illustrating either a range of separate choices in a multi-modal problem or illustrating a trade-off between objectives in a multi-objective problem (Leyland, 2002). A drawback of GAs is that they tend to be computationally expensive, requiring long periods of time for complete convergence. Optimization problems that are not particularly difficult to solve could be solved more quickly by a gradient-based method. Another drawback to GAs is that different runs of the same optimization problem will often result in different solutions due to the random nature of the search process. This can be partially overcome by coupling the GA to a gradient-based method, which takes the solution produced by the GA and converges that solution towards the global or near-global optimum.

4.4.3 MooLENI Genetic Algorithm

The optimization utility used for this thesis work is MooLENI, also called the queuing multi-objective optimizer (QMOO). QMOO is a GA based optimizing software developed by Geoff Leyland and Adam Molyneaux at the Laboratoire d'Energetique Industrielle (Laboratory of Industrial Energy Systems, LENI) at the Ecole Polytechnique Federale de Lausanne (EPFL). QMOO was developed at LENI for the purpose of optimizing energy conversion system problems.

QMOO is a steady-state GA where individuals are added to the population when they are ready and are removed from the population when they are exposed to be 'weak'. QMOO is very elitist by having a single population that contains only the best individuals that have been discovered to that point. Therefore, QMOO rapidly converges to a solution, but requires intervention in order to preserve diversity. QMOO does this by dividing the population into groups in the parameter space, allowing these groups to evolve somewhat independently. QMOO also uses cluster analysis techniques to identify separate local optima simultaneously and to also give it a greater chance of finding the global or near-global optimum. Additionally, QMOO uses an algorithm flexible queue-

based structure that makes it simple to parallelize, and it is a robust optimizer that requires minimal tuning to the specific problem at hand.

To obtain a more detailed description about the QMOO algorithm, find more information on GAs, or to observe additional applications of the QMOO optimization program, the reader is referred to the doctoral dissertation of Geoff Leyland (2002).

4.4.4 QMOO Test Problem

In order to demonstrate the operation of QMOO, a simple test problem was conducted using a complex mathematical equation as the objective function. The test case was conducted using the Woods function. This is an appropriate function for testing both the robustness and convergence speed of this type of algorithm. The Woods function based optimization problem is defined as follows:

$$\text{Minimize: } \begin{aligned} f(\vec{x}) &= 100(x_2 - x_1^2)^2 + (1-x_1)^2 + 90(x_4 - x_3^2)^2 + (1-x_3)^2 \\ &+ 10.1\left[(x_2-1)^2 + (x_4-1)^2\right] + 19.8(x_2-1)(x_4-1) \end{aligned} \tag{4.13}$$

$$\text{where} \qquad -50 \le x_1, x_2, x_3, x_4 \le 50 \tag{4.14}$$

Through inspection of the Woods function, it is apparent that the minimum value of $f(\vec{x})$ is zero when $x_1 = x_2 = x_3 = x_4 = 1$. The QMOO optimization program was run three separate times for the Woods function test and was aborted once the objective function value became less than $f(\vec{x}) = 10^{-5}$. The results of the optimization runs are displayed in Table 4.3 and a contour plot of the Woods function is presented in Figure 4.1.

Table 4.3: Woods function optimization results.

Run	Evaluations	f(x)	x_1	x_2	x_3	x_4
1	2,900	10^{-5}	1.0002	1.0003	1.0003	1.0006
2	3,400	8×10^{-6}	1.0003	1.0005	1.0001	1.0003
3	11,700	8×10^{-6}	0.9999	0.9997	1.0000	1.0003

Although it took a varying amount of evaluations to arrive at the optimized result, the QMOO program performed quite well in optimizing the Woods function. Note that the number of evaluations are the population of 100 times the number of generations (e.g. run 1 has 29 generations of a population of 100, thus, 2,900 evaluations). The optimizations took from 1 minute to 3 minutes on a 133 MHz Pentium 2 processor with 130 MB of RAM.

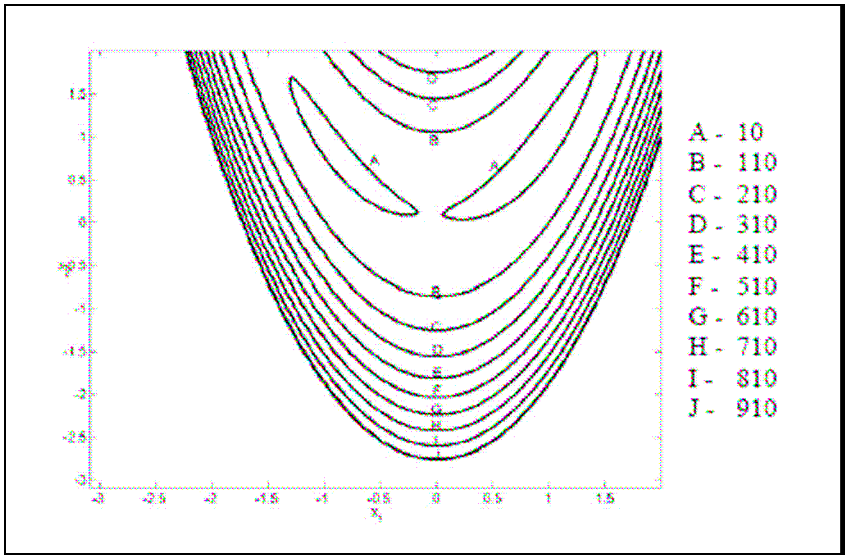

Figure 4.1: Woods function contour plot with $x_3 = x_4 = 1$ (Markell, 2005).

Chapter 5

Results and Discussion

In this chapter, the results of the optimization runs for the four different objective functions presented in Chapter 4 are discussed. These results are for both the morphing-wing and fixed-wing aircraft cases. Before sifting through these optimization results, validation results for the aircraft models with respect to typical design parameters and their expected values are presented. An exergy analysis is then presented to provide some insight into the progression of the aircraft's synthesis/design as it moves closer to its optimum and, in particular, what components and mission segments show the greatest gains in terms of decreased losses as the optimization evolves. Next, the optimal synthesis/design and operational decision variable values are presented and evaluated for both the fixed-wing and morphing-wing optimization cases for each of the four objective functions. This is then followed by a comparison of the optimal results for the four objective functions that to determine which one gives the best performance results (i.e. the lowest amount of fuel consumed or the least amount of exergy destroyed or lost). The optimization results of the morphing-wing aircraft are then compared to the baseline fixed-wing aircraft to determine if and to what extent the aircraft's performance can be enhanced by allowing the wings to morph during a mission. This is done by comparing the amount of fuel burned and the overall exergy destruction and exergy loss results of the morphing- and fixed-wing aircrafts for the objective functions that gave the best results. These results also include a component breakdown to map where the greatest destruction and loss of exergy in the aircraft system occurs as well as a breakdown of the overall mission by segment to determine where morphing produced the greatest amount of fuel savings. In the final part of this chapter, a sensitivity analysis is performed on the optimization results for objective function 1 by varying the wing actuator and fuel weight penalties used to account for the morphing wing actuation. This analysis shows the

region over which the morphing-wing aircraft design demonstrates performance advantages over the traditional fixed-wing aircraft.

5.1 Validation and Prediction of Model Results

In order to validate the results produced by the aircraft models, specific aspects of the fixed-wing aircraft model are compared to the predicted fixed-wing examples presented in Mattingly et al. (2002). In particular aerodynamic aspects (i.e. lift and drag characteristics, wing loading) of the fixed-wing aircraft synthesis/design resulting from the objective function that minimizes fuel consumption are compared to those estimated by Mattingly et al. (2002) for the supersonic penetration mission segment as shown in Table 5.1.

Table 5.1: Comparison of calculated aerodynamic values to the estimated values for the supersonic penetration mission segment.

Parameter	Predicted Value (Mattingly et al., 2002)	Optimal Value
Coefficient of Lift, C_L	0.05558	0.07482
Coefficient of Drag, C_D	0.02886	0.02903
Induced Drag Factor, K_1	0.28	0.2454
Parasitic Drag Coef., C_{Do}	0.028	0.02766
Wing Loading, W_{TO}/S	64 lb/ft^2	91.34 lb/ft^2

As can be seen from the table the values of the coefficients of drag (C_D) and parasitic drag (C_{Do}) are nearly identical and the values of the induced drag factor (K_1) vary only slightly. The optimal wing loading value (W_{TO}/S) resulting from the optimization is 43% higher than the W_{TO}/S used in Mattingly et al. (2002). Note that the W_{TO}/S value is not specific to the supersonic penetration mission segment, but rather the overall synthesis/design of the vehicle. Although this may seem like a significant difference, previously designed fighter aircraft have had takeoff wing loading values as low as 50 lb/ft^2 (e.g. the Mirage 4000, F-106A) and as high as 130 lb/ft^2 (e.g. the F-111-F) (Mattingly et al., 2002). The optimal wing loading generated here is certainly within

this range of feasible fighter aircraft takeoff wing loading. The coefficient of lift (C_L) calculated by the optimizer is also higher than the value used in Mattingly et al. (2002), but this is to be expected since C_L is directly related to the W_{TO}/S.

The PS aspect of the fixed-wing aircraft synthesis/design resulting from the objective function that minimizes AAF exergy destruction and loss are compared to those estimated by Saravanamuttoo, Rogers, and Cohen (2001) for the subsonic cruise mission segment as shown in Table 5.2.

Table 5.2: Comparison of calculated PS values to the estimated values for the subsonic cruise mission segment.

Parameter	Predicted Value (Saravanamuttoo, Rogers, and Cohen, 2001)	Optimal Value
Fuel-to-Air Ratio, *f*	0.01980	0.01999
Compressor Pressure Ratio, *PR*	10.0	10.0
Thrust Specific Fuel Consumption, *TSFC*	1.187 h^{-1}	1.010 h^{-1}

As can be seen from this comparison, predicted and optimal values for the compressor pressure ratio are identical. The PS used by Saravanamuttoo, Rogers, and Cohen (2001) runs slightly leaner on this mission segment than that of the optimal value since its fuel-to-air ratio is a slightly lower value. However, the predicted TSFC value is higher than that of the synthesis/design of the PS, making the optimal synthesis/design more fuel efficient. This is to be expected since the synthesized/designed aircraft is optimized to be a more efficient (i.e. lower loss) AAF.

5.2 Preliminary Synthesis/Design Exergy Analysis

In this section, a preliminary exergy analysis of the initial and intermediate syntheses/designs generated for the fuel consumed objective function (objective function 1) is performed in order to view the progression of the synthesis/design towards the optimum. Since the morphing-wing aircraft is expected to produce the best vehicle synthesis/designs, its preliminary results will be used to conduct the exergy analysis. The

initial and intermediate results for the amount of exergy destroyed and fuel exergy lost as well as the amount of fuel consumed for each mission segment are presented in Figures 5.1 and 5.2.

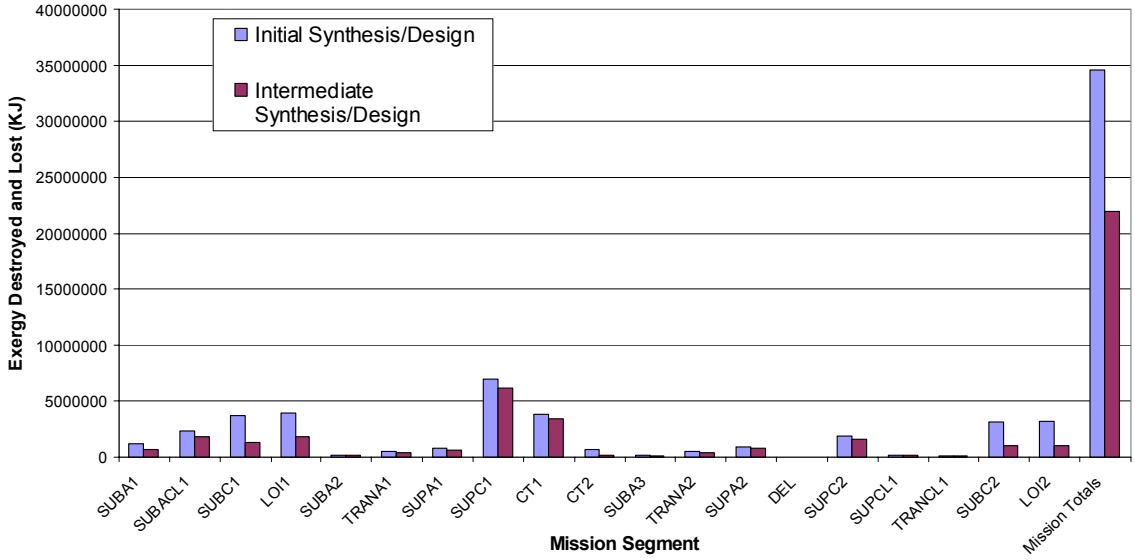

Figure 5.1: Exergy analysis of preliminary results of objective function1 by mission segment for the morphing-wing AAF.

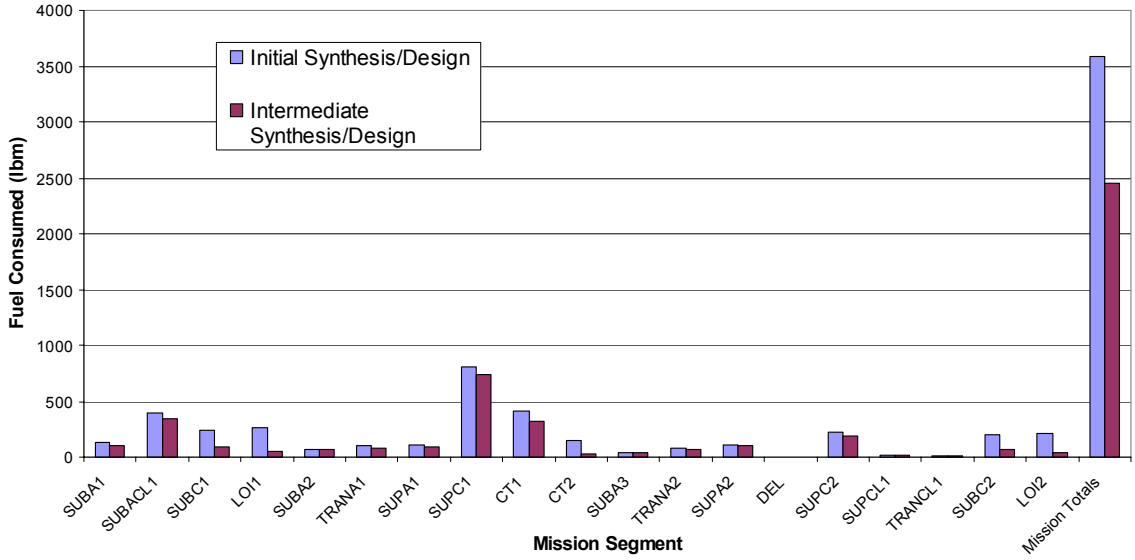

Figure 5.2: Fuel consumption analysis of preliminary results of objective function 1 by mission segment for the morphing-wing AAF.

These two figures show very similar trends between the amount of exergy destroyed/fuel exergy lost and fuel consumed for each mission segment and the mission itself. For the overall mission, the intermediate synthesis/design destroys and looses 22.0

GJ of exergy, a 36 % improvement over the initial synthesis/design, which destroys and looses 34.5 GJ of exergy. The intermediate synthesis/design also consumes 2454 lbm of fuel over the entire mission; a 32% improvement over the initial synthesis/design, which consumes 3583 lbm of fuel. Furthermore, the intermediate synthesis/design shows improvement in the exergy destruction and loss and subsequently in the fuel consumption for every mission segment, especially the subsonic mission segments where no change in kinetic or potential energy occurs (i.e. the subsonic cruse, loiter, and turn segments).

In order to determine what system/component mechanisms are contributing to the synthesis/design improvement between the initial and intermediate results and to determine their magnitude and location, the exergy analysis can be broken down by subsystem component. One of the most useful features of an exergy analysis is its ability to relate the irreversibilities in the different system components to each other through a framework of common metrics. This allows for a consistent comparison of the impact on system performance that the different system components have in terms of their thermodynamic losses. Since the greatest improvement occurrs in the subsonic mission segments, the subsonic cruise mission segment (SUBC1) is used to illustrate the component exergy analysis. The results appear in Figure 5.3.

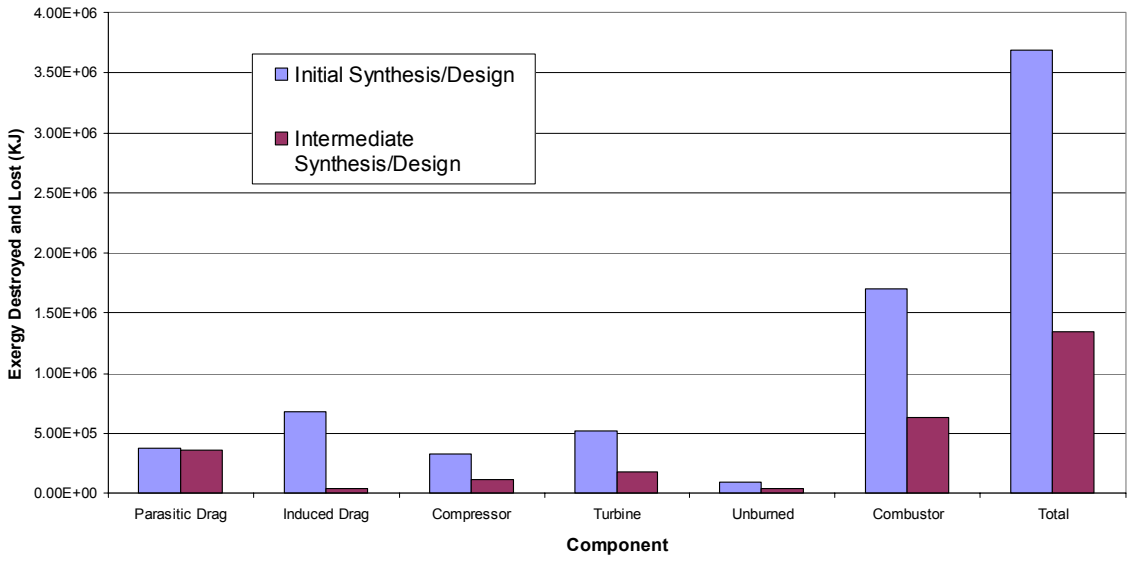

Figure 5.3: Component breakdown of exergy destruction at subsonic cruise mission segment (SUBC1) for preliminary designs for objective function 1.

This component exergy analysis shows a slight improvement in the amount of exergy destroyed due to the parasitic drag and a dramatic improvement in the amount of exergy destroyed due to the induced drag between the initial and intermediate syntheses/designs. The induced and parasitic drags are reduced as the vehicle achieves a more optimal aerodynamic design for the AFS-A by varying its geometric synthesis/design and operational decision variables. This in turn reduces the amount of exergy destroyed by both the induced and parasitic drag parameters. The outcome is a 63% reduction in overall exergy destroyed due to drag between the initial synthesis/design (1.05 GJ of exergy destroyed) and the intermediate synthesis/design (0.39 GJ of exergy destroyed).

The reduction in exergy destroyed due to drag in the AFS-A also translates into a reduction in exergy destruction for the PS components since less thrust is required to overcome the irreversibilities produced by the AFS-A. The PS components are also directly affected by its synthesis/design and operational decision variables as a more optimal configuration is reached. The progress of the optimization is shown in Figure 5.3. This figure shows a 64 % reduction in the exergy destroyed and lost by the components of the PS (compressor, turbine, and combustor) between the initial and intermediate syntheses/designs with the largest contribution in this reduction occurring in the combustor followed by the turbine and then the compressor. A similar 64% reduction occurs for the vehicle as a whole. A reduction in exergy lost due to unburned fuel is also seen as the optimization of objective function 1 progresses. A 36% reduction in overall exergy lost due to unburned fuel between the initial synthesis/design (0.81 GJ of exergy destroyed) and the intermediate synthesis/design (0.52 GJ of exergy destroyed). This reduction in exergy lost is a direct result of the vehicle burning less fuel for the overall mission since the combustor efficiency (η_{COMB}) is held fixed at 98% and is directly proportional to the mass flow rate of fuel consumed by the PS ($\dot{m}_{fuel}$).

5.3 Validation of the Optimization Results

In order to have confidence in whether or not the GA reached the global or a near-global optimum, each objective function was optimized three times to ensure

repeatability of the results. The optimized values of the four objective functions for each of the optimization runs of the morphing-wing AAF are shown in Table 5.3.

Table 5.3: Initial, intermediate and final optimization values of the four different objective functions for the morphing-wing AAF.

Optimization Result	Minimize W_{Burn}	Minimize $Ex_{DES/LOSS\_AAF}$	Minimize $Ex_{DES/LOSS\_PS}$	Maximize η_{thrust}
Initial	3583.2	44404845.45	28776233.32	0.1231
Intermediate	2453.6	25907128.21	11706145.11	0.2809
Final 1	2264.6	19536064.60	10627085.49	0.4576
Final 2	2235.1	19941853.82	10409136.07	0.4620
Final 3	2279.5	20131724.95	10909038.97	0.4601

It can be seen that the objective functions get closer to a global optimum as the optimizing GA progresses from the initial optimum, to the intermediate and final optimums. The three final optimum values for the four objective functions are all very close to one another. The optimal values for the minimization of fuel consumption objective function (objective 1) for the morphing-wing AAF vary by a maximum of 1.95%. The optimal values for the minimization of AAF exergy destruction and loss objective function (objective 2) for the morphing-wing AAF vary by a maximum of 2.96%. The optimal values for the minimization of PS exergy destruction and loss objective function (objective 3) for the morphing-wing AAF vary by a maximum of 4.58%. The optimal values for the maximization of thrust efficiency objective function (objective 4) for the morphing-wing AAF vary by a maximum of 0.952%. All of these optimal values are well within the expected deviation due to the heuristic nature of the GA and the need to search the entire solution space. It is concluded that the GA is finding global or near-global optimums for each of the four objective functions explored.

5.4 Optimum Decision Variable Values

The synthesis/design and operational variable values for the "best" case optimization results as outlined in the previous section (Section 5.3) are presented in this section for both the morphing- and fixed-wing aircraft models.

5.4.1 Optimal Fixed-wing AAF Synthesis/Design and Operational Decision Variable Results

The "best" of the optimal synthesis/design decision variable values for the fixed-wing optimal AAF for each of the four different objective functions are presented in Table 5.3 while those for the "best" of the optimal operational variable values are presented in Table 5.4. The "best" variable values in this case are defined as the variable values resulting from the most optimal objective functions determined by the optimization software. A set of 4 synthesis/design decision variables and no operational decision variables were used for the AFS-A of the fixed-wing AAF, while a set of 3 synthesis/design decision variables and 3 operational decision variables per mission segment were employed for the PS for a total of 73 degrees of freedom at the optimization level. As discussed in Section 4.1 of Chapter 4, a Genetic Algorithm (GA) was used for the optimizations.

Table 5.4: The "best" of the optimum values for the synthesis/design decision variables of the fixed-wing AAF for the four objective functions.

Subsystem		Objective Function			
		Minimize W_{Burn}	**Minimize** $Ex_{DES/LOSS\_AAF}$	**Minimize** $Ex_{DES/LOSS\_PS}$	**Maximize** η_{thrust}
AFS-A					
Wing Sweep Angle (^{o})	Λ	41.61	38.58	33.30	49.20
Wing Length (ft)	WL	41.85	38.55	34.04	50.00
Root Chord Length (ft)	r	5.13	5.27	5.36	9.99
Tip Chord Length (ft)	t	2.67	2.59	2.57	9.33
PS					
Compressor Pressure Ratio	PR_{comp}	23.91	26.87	22.12	24.25
Compressor Corrected Flow Rate (kg/s)	$\dot{m}_{COMP}$	10.24	10.01	13.58	11.01
Turbine Corrected Flow Rate (kg/s)	$\dot{m}_{TURB}$	54.89	51.80	50.00	51.50

Each of the several optimization runs made for each of the objective functions using the GA took several days to reach an acceptable optimum due to the heuristic nature of the GA and the need to search the entire solution space.

Table 5.5: The "best" of the optimum values for the operational decision variables of the PS for the fixed-wing AAF.

Mission Segment		Objective Function			
		Minimize W_{burn}	**Minimize** $Ex_{DES/LOSS\_AAF}$	**Minimize** $Ex_{DES/LOSS\_PS}$	**Maximize** η_{thrust}
Takeoff/Acceleration					
PR	Compressor Pressure Ratio	14.21	14.79	10.91	13.76
f	Combustor Fuel-to-Air Ratio	0.011209	0.011555	0.012331	0.012939
f_{aft}	Afterburner Fuel-to-Air Ratio	0	0	0	0
Acceleration/Climb					
PR	Compressor Pressure Ratio	13.86	10.14	10.25	14.23
f	Combustor Fuel-to-Air Ratio	0.008681	0.019698	0.009904	0.011446
f_{aft}	Afterburner Fuel-to-Air Ratio	0	0	0	0
Subsonic Cruise					
PR	Compressor Pressure Ratio	21.88	10.00	10.00	13.73
f	Combustor Fuel-to-Air Ratio	0.017714	0.019998	0.019998	0.007621
f_{aft}	Afterburner Fuel-to-Air Ratio	0	0	0	0
Combat Air Patrol					
PR	Compressor Pressure Ratio	24.74	10.01	10.00	24.87
f	Combustor Fuel-to-Air Ratio	0.017904	0.020000	0.019997	0.018180
f_{aft}	Afterburner Fuel-to-Air Ratio	0	0	0	0
Acceleration					
PR	Compressor Pressure Ratio	14.60	15.02	11.03	15.02
f	Combustor Fuel-to-Air Ratio	0.009150	0.009555	0.010792	0.012380
f_{aft}	Afterburner Fuel-to-Air Ratio	0.007025	0.007002	0.007000	0.007021
Transonic Acceleration					
PR	Compressor Pressure Ratio	15.56	16.24	11.98	16.35
f	Combustor Fuel-to-Air Ratio	0.010960	0.012023	0.013615	0.015012
f_{aft}	Afterburner Fuel-to-Air Ratio	0.008784	0.007013	0.007000	0.007023
Supersonic Acceleration					
PR	Compressor Pressure Ratio	18.54	17.27	12.66	17.10
f	Combustor Fuel-to-Air Ratio	0.014293	0.015333	0.017490	0.018120
f_{aft}	Afterburner Fuel-to-Air Ratio	0.007778	0.007547	0.007022	0.007002
Supersonic Penetration					
PR	Compressor Pressure Ratio	10.20	10.00	10.00	11.89
f	Combustor Fuel-to-Air Ratio	0.019027	0.020000	0.019999	0.007683
f_{aft}	Afterburner Fuel-to-Air Ratio	0	0	0	0
Combat Turn (Supersonic)					
PR	Compressor Pressure Ratio	12.66	10.00	10.39	13.90
f	Combustor Fuel-to-Air Ratio	0.007253	0.017022	0.008470	0.012279
f_{aft}	Afterburner Fuel-to-Air Ratio	0.007293	0.007011	0.007001	0.007004
Combat Turn (Subsonic)					
PR	Compressor Pressure Ratio	24.63	10.00	10.01	24.96
f	Combustor Fuel-to-Air Ratio	0.019697	0.019898	0.020000	0.019895
f_{aft}	Afterburner Fuel-to-Air Ratio	0.007013	0.007079	0.007003	0.007026
Acceleration					
PR	Compressor Pressure Ratio	13.56	10.66	10.20	13.55

Mission Segment		Objective Function			
		Minimize W_{burn}	Minimize $Ex_{DES/LOSS\_AAF}$	Minimize $Ex_{DES/LOSS\_PS}$	Maximize η_{thrust}
f	Combustor Fuel-to-Air Ratio	0.007731	0.019423	0.008855	0.011097
f_{aft}	Afterburner Fuel-to-Air Ratio	0.007028	0.007044	0.007078	0.007023
Transonic Acceleration					
PR	Compressor Pressure Ratio	15.46	16.09	10.58	15.65
f	Combustor Fuel-to-Air Ratio	0.011472	0.012057	0.013063	0.015672
f_{aft}	Afterburner Fuel-to-Air Ratio	0.007012	0.007010	0.007001	0.007021
Supersonic Acceleration					
PR	Compressor Pressure Ratio	17.71	18.21	13.85	18.67
f	Combustor Fuel-to-Air Ratio	0.018177	0.018532	0.018592	0.019572
f_{aft}	Afterburner Fuel-to-Air Ratio	0.007049	0.007918	0.007002	0.007030
Escape Dash					
PR	Compressor Pressure Ratio	10.62	10.00	10.01	11.26
f	Combustor Fuel-to-Air Ratio	0.019261	0.019999	0.019996	0.007659
f_{aft}	Afterburner Fuel-to-Air Ratio	0	0	0	0
Supersonic Climb					
PR	Compressor Pressure Ratio	12.63	10.00	10.01	12.59
f	Combustor Fuel-to-Air Ratio	0.018742	0.019982	0.019990	0.011336
f_{aft}	Afterburner Fuel-to-Air Ratio	0	0	0	0
Transonic Climb					
PR	Compressor Pressure Ratio	13.64	14.15	10.65	14.81
f	Combustor Fuel-to-Air Ratio	0.010830	0.011469	0.011905	0.013662
f_{aft}	Afterburner Fuel-to-Air Ratio	0	0	0	0
Subsonic Cruise					
PR	Compressor Pressure Ratio	22.09	10.00	10.04	13.15
f	Combustor Fuel-to-Air Ratio	0.017970	0.019997	0.019999	0.007682
f_{aft}	Afterburner Fuel-to-Air Ratio	0	0	0	0
Loiter					
PR	Compressor Pressure Ratio	24.82	10.24	10.06	23.58
f	Combustor Fuel-to-Air Ratio	0.019951	0.019999	0.020000	0.019992
f_{aft}	Afterburner Fuel-to-Air Ratio	0	0	0	0

The optimum synthesis/design decision variables for the four objective functions shown in Table 5.4 all show differences in the synthesis/design. The differences in these synthesis/design decision variable values range from slight to extreme. For example, all of the optimum synthesis/design variable values for the PS in the fixed-wing AAF (the compressor pressure ratio, compressor corrected mass flow rate and the turbine corrected mass flow rate) are close in value for all of the objective functions. The optimal synthesis/design variable values of the four objectives for the PS range from 22.12 to 26.87 compressor pressure ratios, 10.01 to 13.58 kg/s for the compressor corrected mass flow rates and 50.00 to 54.89 kg/s for the turbine corrected mass flow rates. However,

the optimum synthesis/design variable values for the AFS-A varied by large margins. The optimal synthesis/design variable values of the four objectives for the AFS-A range from 33.3^{o} to 49.2^{o} for the sweep angle, 34.04 to 50.00 ft for the wing length, 5.13 to 9.99 ft for the root chord length, and 2.57 to 9.33 ft for the tip chord length. It appears that the optimized synthesis/design variable values for objective 4 are the most different in comparison to the other objective functions. The optimized synthesis/design of objective 4 creates an AFS-A with a wider, longer, and more swept wing than all of the other objective functions.

The optimal operational decision variable values for each of the different syntheses/designs of the fixed-wing AAF produced by the four different objective functions shown in Table 5.5 are compared and analyzed for a number of different mission segments. First, the optimal operational decision variable values produced by the different objectives for the escape dash mission segment are examined. All of the operational variable values are close in values for the compressor pressure ratio. The operational variable values for the combustor fuel-to-air ratio are also close for objectives 1, 2 and 3, but that of objective 4 runs over twice as lean for this mission segment.

Next, the optimal operational decision variable values produced by the different objectives for the subsonic cruise mission segment are compared. In this mission segment the operational variable values for the compressor pressure ratio are relatively close for objectives 2, 3, and 4, but that for objective 1 is about twice as high as the others. As in the previous mission segment examined, the operational decision variable values for the combustor fuel-to-air ratio are close for objectives 1, 2 and 3 with objective 4 again having a value that is over twice as lean as the others. From the optimal synthesis/design decision variable values and the operational decision variable values presented above, it appears that the optimization of the four objective functions have produced relatively close syntheses/designs for objectives 1, 2, and 3, and a drastically different synthesis/design for objective 4.

5.4.2 Morphing wing operational and design variable results

The “best” of the optimal synthesis/design decision variable values for the morphing-wing AAF for each of the four different objective functions are presented in

Table 5.6 while those for the "best" of the optimal operational decision variable values are presented in Table 5.7. The "best" variable values in this case are defined as the variable values resulting from the most optimal objective functions determined by the optimization software.

Table 5.6: The "best" of the optimum values for the design decision variables of the morphing-wing AAF for the four objective functions.

Subsystem		Objective Function			
		Minimize W_{burn}	**Minimize** $Ex_{DES/LOSS\_AAF}$	**Minimize** $Ex_{DES/LOSS\_PS}$	**Maximize** η_{thrust}
AFS-A					
Wing Length (ft)	WL	44.05	42.51	38.14	33.40
Root Chord Length (ft)	r	8.26	8.04	8.94	7.72
Tip Chord Length (ft)	t	7.53	7.42	8.84	7.54
PS					
Compressor Pressure Ratio	PR_{comp}	24.70	22.54	27.78	25.12
Compressor Corrected Flow Rate (kg/s)	$\dot{m}_{COMP}$	10.81	13.73	12.48	30.81
Turbine Corrected Flow Rate (kg/s)	$\dot{m}_{TURB}$	52.74	63.14	56.85	72.20

Just as for the fixed-wing model, the same set of decision variables was used for each of these four optimizations, except that an additional set of 4 operational decision variables per mission segment were used for the AFS-A for a total of 160 degrees of freedom at the optimization level. The four additional decision variables per mission segment include the wing sweep, wing lenth, and root and tip chord lengths.

Table 5.7: The "best" of the optimum values for the operational decision variables for the PS and AFS-A for the morphing-wing AAF for the four objective functions.

Mission Segment		Objective Function			
		Minimize W_{burn}	**Minimize** $Ex_{DES/LOSS\_AAF}$	**Minimize** $Ex_{DES/LOSS\_PS}$	**Maximize** η_{thrust}
Takeoff/Acceleration					
PS					
PR	Compressor Pressure Ratio	13.49	12.46	12.38	13.39
f	Combustor Fuel-to-Air Ratio	0.011541	0.010062	0.010897	0.009388
f_{aft}	Afterburner Fuel-to-Air Ratio	0	0	0	0
AFS-A					
Λ	Wing Sweep Angle (^{o})	15.68	22.05	8.42	22.51

Mission Segment		Objective Function			
		Minimize W_{burn}	Minimize $Ex_{DES/LOSS\_AAF}$	Minimize $Ex_{DES/LOSS\_PS}$	Maximize η_{thrust}
WL	Wing Length (ft)	36.94	25.26	32.14	22.56
r	Root Chord Length (ft)	5.54	4.38	4.02	7.61
t	Tip Chord Length (ft)	0.19	0.34	1.63	0.77
Acceleration/Climb					
PS					
PR	Compressor Pressure Ratio	13.38	10.67	11.69	18.79
f	Combustor Fuel-to-Air Ratio	0.008518	0.007758	0.009145	0.017213
f_{aft}	Afterburner Fuel-to-Air Ratio	0	0	0	0
AFS-A					
Λ	Wing Sweep Angle (^{o})	21.19	17.07	10.78	22.35
WL	Wing Length (ft)	34.21	32.12	31.23	24.83
r	Root Chord Length (ft)	4.58	4.00	4.03	5.24
t	Tip Chord Length (ft)	0.52	1.33	1.12	0.19
Subsonic Cruise					
PS					
PR	Compressor Pressure Ratio	21.31	10.02	10.09	23.67
f	Combustor Fuel-to-Air Ratio	0.017604	0.019998	0.019962	0.017423
f_{aft}	Afterburner Fuel-to-Air Ratio	0	0	0	0
AFS-A					
Λ	Wing Sweep Angle (^{o})	12.71	12.82	10.84	11.74
WL	Wing Length (ft)	35.68	35.50	34.11	31.22
r	Root Chord Length (ft)	4.00	4.00	4.00	4.06
t	Tip Chord Length (ft)	1.66	1.63	1.49	2.04
Combat Air Patrol					
PS					
PR	Compressor Pressure Ratio	24.00	10.05	10.00	19.81
f	Combustor Fuel-to-Air Ratio	0.017475	0.019997	0.019998	0.016054
f_{aft}	Afterburner Fuel-to-Air Ratio	0	0	0	0
AFS-A					
Λ	Wing Sweep Angle (^{o})	12.27	12.68	12.48	53.86
WL	Wing Length (ft)	37.61	35.31	34.52	13.40
r	Root Chord Length (ft)	4.03	4.00	4.00	4.01
t	Tip Chord Length (ft)	1.95	1.63	1.48	1.77
Acceleration					
PS					
PR	Compressor Pressure Ratio	13.31	11.52	11.49	20.25
f	Combustor Fuel-to-Air Ratio	0.008965	0.007866	0.009547	0.016606
f_{aft}	Afterburner Fuel-to-Air Ratio	0.007017	0.007009	0.007027	0.011316
AFS-A					
Λ	Wing Sweep Angle (^{o})	12.40	13.20	11.12	17.20
WL	Wing Length (ft)	33.21	34.05	33.77	18.68
r	Root Chord Length (ft)	4.06	4.12	5.34	5.57
t	Tip Chord Length (ft)	1.51	1.36	0.79	1.76
Transonic Acceleration					
PS					
PR	Compressor Pressure Ratio	14.97	12.74	13.79	12.90

Mission Segment		Objective Function			
		Minimize W_{burn}	Minimize $Ex_{DES/LOSS\_AAF}$	Minimize $Ex_{DES/LOSS\_PS}$	Maximize η_{thrust}
f	Combustor Fuel-to-Air Ratio	0.012140	0.010017	0.009320	0.009264
f_{aft}	Afterburner Fuel-to-Air Ratio	0.007042	0.009052	0.015062	0.011585
AFS-A					
Λ	Wing Sweep Angle (^{o})	41.49	41.23	45.74	46.33
WL	Wing Length (ft)	38.20	34.84	33.28	19.58
r	Root Chord Length (ft)	4.10	4.08	4.93	4.77
t	Tip Chord Length (ft)	3.17	2.50	2.90	2.03
Supersonic Acceleration					
PS					
PR	Compressor Pressure Ratio	15.97	13.26	15.36	13.76
f	Combustor Fuel-to-Air Ratio	0.015812	0.012001	0.014323	0.011399
f_{aft}	Afterburner Fuel-to-Air Ratio	0.007023	0.012284	0.008457	0.011412
AFS-A					
Λ	Wing Sweep Angle (^{o})	37.88	42.06	40.11	43.71
WL	Wing Length (ft)	31.36	33.21	31.22	18.88
r	Root Chord Length (ft)	5.35	4.01	4.33	5.23
t	Tip Chord Length (ft)	1.32	2.19	1.89	3.50
Supersonic Penetration					
PS					
PR	Compressor Pressure Ratio	10.14	10.00	10.01	13.19
f	Combustor Fuel-to-Air Ratio	0.019141	0.019998	0.019999	0.018383
f_{aft}	Afterburner Fuel-to-Air Ratio	0	0	0	0
AFS-A					
Λ	Wing Sweep Angle (^{o})	43.34	40.02	37.46	46.20
WL	Wing Length (ft)	28.48	27.29	27.65	25.92
r	Root Chord Length (ft)	4.02	4.94	5.81	4.31
t	Tip Chord Length (ft)	1.60	1.02	0.65	1.65
Combat Turn (Supersonic)					
PS					
PR	Compressor Pressure Ratio	10.81	10.77	11.46	12.87
f	Combustor Fuel-to-Air Ratio	0.009177	0.007000	0.007000	0.015489
f_{aft}	Afterburner Fuel-to-Air Ratio	0.007048	0.007000	0.007000	0.008608
AFS-A					
Λ	Wing Sweep Angle (^{o})	44.30	44.38	37.20	39.19
WL	Wing Length (ft)	43.94	42.51	21.79	32.38
r	Root Chord Length (ft)	6.81	4.87	4.11	7.17
t	Tip Chord Length (ft)	4.67	4.87	0.82	6.25
Combat Turn (Subsonic)					
PS					
PR	Compressor Pressure Ratio	17.96	10.19	13.03	18.87
f	Combustor Fuel-to-Air Ratio	0.017712	0.019974	0.019316	0.015400
f_{aft}	Afterburner Fuel-to-Air Ratio	0.007083	0.007117	0.008806	0.010028
AFS-A					
Λ	Wing Sweep Angle (^{o})	12.28	14.56	9.63	10.98
WL	Wing Length (ft)	41.91	38.95	30.60	33.40
r	Root Chord Length (ft)	4.49	4.14	4.03	4.01

Mission Segment		Objective Function			
		Minimize W_{burn}	Minimize $Ex_{DES/LOSS\_AAF}$	Minimize $Ex_{DES/LOSS\_PS}$	Maximize η_{thrust}
t	Tip Chord Length (ft)	2.19	1.94	1.38	2.00
Acceleration					
PS					
PR	Compressor Pressure Ratio	12.96	10.17	10.16	18.10
f	Combustor Fuel-to-Air Ratio	0.007534	0.008462	0.019694	0.018596
f_{aft}	Afterburner Fuel-to-Air Ratio	0.007031	0.007010	0.007943	0.015708
AFS-A					
Λ	Wing Sweep Angle (^{o})	12.30	20.46	11.35	42.18
WL	Wing Length (ft)	30.39	32.74	30.53	27.17
r	Root Chord Length (ft)	4.81	4.57	4.11	5.27
t	Tip Chord Length (ft)	0.18	0.45	1.44	1.80
Transonic Acceleration					
PS					
PR	Compressor Pressure Ratio	14.81	12.92	13.43	19.02
f	Combustor Fuel-to-Air Ratio	0.011985	0.010499	0.011196	0.016258
f_{aft}	Afterburner Fuel-to-Air Ratio	0.007016	0.007001	0.008597	0.010161
AFS-A					
Λ	Wing Sweep Angle (^{o})	40.35	40.21	34.55	43.24
WL	Wing Length (ft)	33.85	31.44	27.93	22.43
r	Root Chord Length (ft)	4.53	4.16	4.68	4.97
t	Tip Chord Length (ft)	2.04	1.96	2.08	3.13
Supersonic Acceleration					
PS					
PR	Compressor Pressure Ratio	17.19	14.88	16.15	18.62
f	Combustor Fuel-to-Air Ratio	0.017442	0.015978	0.017077	0.013287
f_{aft}	Afterburner Fuel-to-Air Ratio	0.014921	0.009874	0.012363	0.010773
AFS-A					
Λ	Wing Sweep Angle (^{o})	41.89	42.62	40.99	30.51
WL	Wing Length (ft)	33.01	29.86	27.81	15.89
r	Root Chord Length (ft)	4.02	4.01	4.58	6.07
t	Tip Chord Length (ft)	2.17	1.81	1.83	1.78
Escape Dash					
PS					
PR	Compressor Pressure Ratio	10.07	10.00	10.02	11.09
f	Combustor Fuel-to-Air Ratio	0.018543	0.019992	0.019985	0.016442
f_{aft}	Afterburner Fuel-to-Air Ratio	0	0	0	0
AFS-A					
Λ	Wing Sweep Angle (^{o})	42.85	39.83	41.94	38.37
WL	Wing Length (ft)	27.36	25.11	27.72	15.63
r	Root Chord Length (ft)	4.00	4.58	4.42	5.02
t	Tip Chord Length (ft)	1.48	0.93	1.35	2.76
Supersonic Climb					
PS					
PR	Compressor Pressure Ratio	11.54	10.10	10.54	19.02
f	Combustor Fuel-to-Air Ratio	0.017611	0.019961	0.019469	0.015530
f_{aft}	Afterburner Fuel-to-Air Ratio	0	0	0	0

Mission Segment		Objective Function			
		Minimize W_{burn}	Minimize $Ex_{DES/LOSS\_AAF}$	Minimize $Ex_{DES/LOSS\_PS}$	Maximize η_{thrust}
AFS-A					
Λ	Wing Sweep Angle (^{o})	42.17	36.52	38.04	46.95
WL	Wing Length (ft)	33.46	26.83	25.30	22.93
r	Root Chord Length (ft)	4.56	4.04	4.04	4.41
t	Tip Chord Length (ft)	1.98	1.77	1.89	3.43
Transonic Climb					
PS					
PR	Compressor Pressure Ratio	13.99	11.43	14.24	17.05
f	Combustor Fuel-to-Air Ratio	0.010845	0.010850	0.011063	0.012474
f_{aft}	Afterburner Fuel-to-Air Ratio	0	0	0	0
AFS-A					
Λ	Wing Sweep Angle (^{o})	37.65	37.64	38.36	46.44
WL	Wing Length (ft)	39.46	39.58	36.60	23.94
r	Root Chord Length (ft)	6.30	6.33	6.41	5.93
t	Tip Chord Length (ft)	2.14	1.95	3.81	1.27
Subsonic Cruise					
PS					
PR	Compressor Pressure Ratio	21.41	10.03	10.01	19.25
f	Combustor Fuel-to-Air Ratio	0.017618	0.019975	0.019843	0.014444
f_{aft}	Afterburner Fuel-to-Air Ratio	0	0	0	0
AFS-A					
Λ	Wing Sweep Angle (^{o})	12.41	13.05	13.00	11.31
WL	Wing Length (ft)	36.87	35.70	35.68	29.85
r	Root Chord Length (ft)	4.00	4.01	4.01	4.10
t	Tip Chord Length (ft)	1.89	1.63	1.64	1.49
Loiter					
PS					
PR	Compressor Pressure Ratio	22.83	10.18	11.40	18.15
f	Combustor Fuel-to-Air Ratio	0.019486	0.019998	0.019990	0.010932
f_{aft}	Afterburner Fuel-to-Air Ratio	0	0	0	0
AFS-A					
Λ	Wing Sweep Angle (^{o})	12.08	15.02	12.34	50.56
WL	Wing Length (ft)	41.01	36.67	34.89	13.40
r	Root Chord Length (ft)	4.60	4.15	4.00	4.04
t	Tip Chord Length (ft)	1.93	1.55	1.56	0.52

The optimum synthesis/design decision variables for the four objective functions shown in Table 5.6 all show differences in the synthesis/design. The differences in these synthesis/design decision variable values range from slight to extreme. For example, the root and tip chord lengths of the AFS-A produced by all of the objective functions are relatively close in value with variations of no more than 13 % and 16%, respectively, in the extreme cases. However, the wing lengths of the AFS-A produced by the four

objective functions show a much larger variation, especially for that produced by objective 4, which is 24.2% shorter than that of objective one. Large differences between the synthesis/design decision variables produced by objective 4 and those of the other objectives also exist in the PS with the compressor corrected mass flow rate, which is nearly 3 times greater than any of the other values. It appears from these results that the optimization of objective function 4 has synthesized/designed an AAF with a much narrower AFS-A and more powerful PS than any of the other objective functions.

The optimal operational decision variable values for each of the different syntheses/designs of the morphing-wing AAF produced by the four different objective functions are compared and analyzed for a number of different mission segments. First, the optimal operational decision variable values produced by the different objectives for the combat air patrol mission segment shown in Table 5.7 are examined. The different objectives seem to produce very similar values for the combustor fuel-to-air ratios, root chord lengths and tip chord lengths. However, they produce drastically different optimal operational values for the compressor pressure ratios, wing sweep angles, and wing length. Again, objective 4 produces drastically different values than all of the other objectives.

The optimal operational decision variable values produced by the four objective functions are now compared for the escape dash mission segment shown in Table 5.7 since it has very different flight conditions from that of the previously examined combat air patrol mission segment. In this mission segment, the optimal operational decision variable values of the four objective functions for compressor pressure ratios, combustor fuel-to-air ratios, and wing sweeps are all close in value. Conversely, the wing lengths, and root and tip chord lengths show very drastic differences between the results produced by the four objective functions. Once again, many of the values produced by objective 4 are drastically different from the values of the other three objectives.

5.5 Analysis and Comparison of the Optimal AAF Syntheses/Designs

Results for the four different objective functions are compared in this section in order to identify what, if any, differences exist between the various optimized syntheses/designs predicted for the AAF.

The amount of fuel consumed by the morphing-wing aircraft over the entire mission for each of the four optimized objective functions is presented in Figure 5.4. The objective function that minimizes the fuel consumed only uses 2235 lbm of fuel over the entire mission. This is the lowest amount of fuel consumed for all of the four objective functions. The objective function that minimizes the total amount of exergy destroyed and losst for the AAF (PS and AFS-A combined) uses 2274 lbm of fuel over the mission. Comparatively, the results of these two objective functions for the amount of fuel consumed during the mission are extremely close varying by less than 1.74% and well within the variation which might be expected when using a heuristic approach such as a GA for the optimization. The objective function that minimizes the amount of exergy destroyed and lost by the PS only uses 2634 lbm of fuel during the mission; about 17.9 % more fuel than that used by the fuel consumed objective function used. The objective function that maximizes the thrust efficiency of the aircraft consumes the greatest amount of fuel (3995 lbs) during the mission. The reasons for these differences are discussed below following figure 5.7.

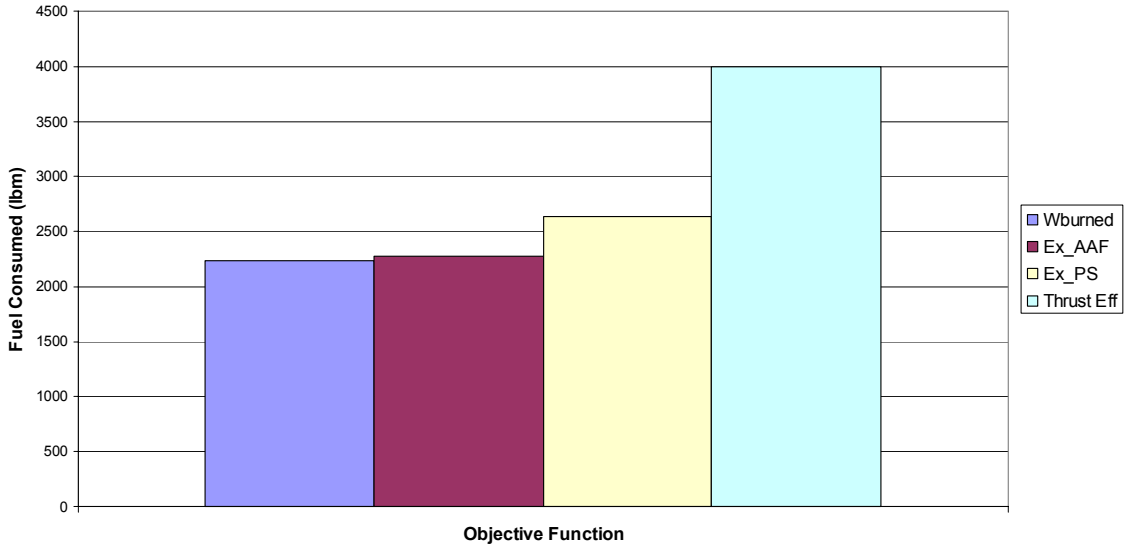

Figure 5.4: Amount of fuel consumed during the mission by each of the optimized synthesis/designs predicted by the different objective function design (morphing-wing case).

The total amount of exergy destroyed by the morphing-wing aircraft over the mission for each of the four optimized objective functions is presented in Figure 5.5. The objective function that minimizes the total amount of exergy destroyed and lost has an optimal value of 19.536 GJ of exergy during the mission, which is the lowest value of all of the objective function optimizations. The objective function that minimizes the amount of fuel consumed destroys 20.834 GJ of exergy during the mission. Once again, these two objective functions produced very close results with their total amounts of exergy destroyed and lost varying by 6.6%. The objective function that minimizes the amount of exergy destroyed and lost by the PS alone destroys 21.866 GJ of exergy during the mission; about 11.9% more than that for the exergy destroyed and lost objective function. The objective function that maximizes the vehicle's thrust efficiency destroys 205.35 GJ of exergy, which is by far the highest amount of exergy destruction and loss during the mission out of all of the objective functions optimized.

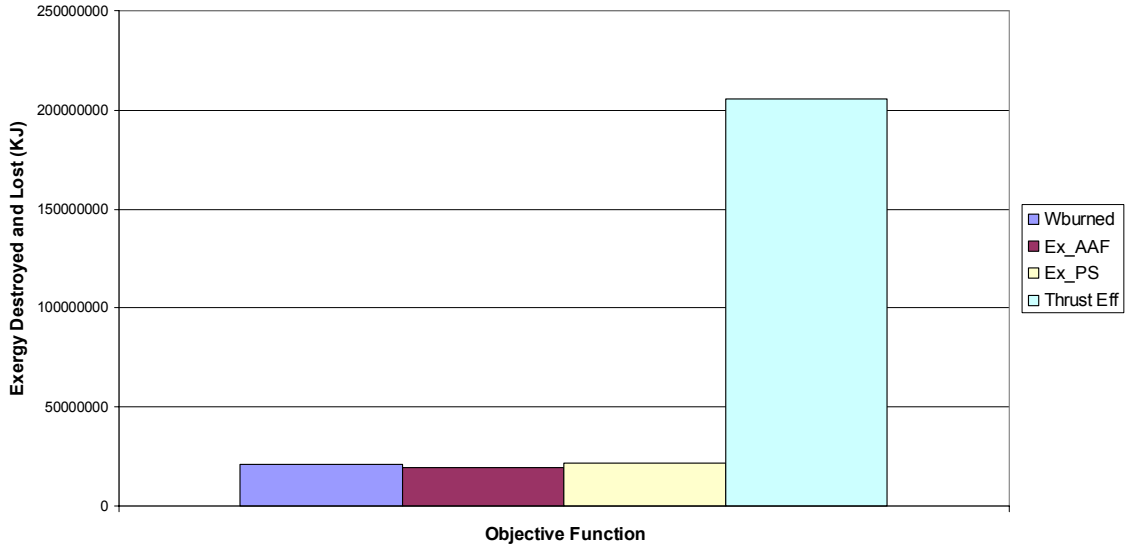

Figure 5.5: Total amount of exergy destroyed and lost during the mission by each of the optimized syntheses/designs predicted by the different objective functions design (morphing-wing case).

The optimization results for the four different objective functions for the fixed-wing aircraft model produced results similar to those for the morphing-wing case as shown in Figures 5.6 and 5.7. Figure 5.6 shows the amount of fuel consumed for each of the designs produced by the different objective functions. Just as in the morphing case,

the minimization of fuel consumption objective function used the least amount of fuel at 3140 lbm, followed by the minimization of AAF exergy destroyed and lost at 3210 lbs (a 2.2% difference with the first objective), the minimization of the PS only exergy destroyed and lost at 3260 lbs (a 3.8% difference), and the maximization of the thrust efficiency at 3908 lbs, (a 24.5% difference). Similarly, Figure 5.7 shows the total amount of exergy destroyed and lost during the mission for each of the syntheses/designs produced by the different objective functions. As expected, the minimization of total exergy destruction destroyed and lost results in the least amount of exergy destroyed and lost at 29.25 GJ, followed by the minimization of PS only exergy destruction and lost at 29.44 GJ (a 0.5% difference with the first objective), the minimization of fuel consumed at 30.56 GJ (a 4.5% difference), and the maximization of the thrust efficiency at 46.61 GJ (a 59.4% difference).

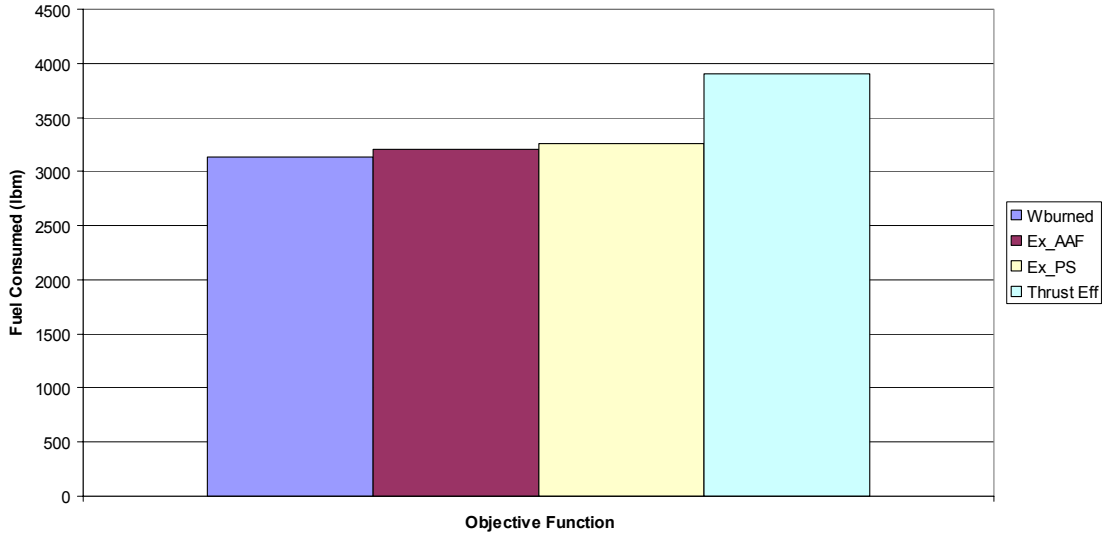

Figure 5.6: Amount of fuel consumed during the mission by each of the optimized syntheses/designs predicted by the different objective functions (fixed-wing case).

It is obvious from Figures 5.3 to 5.7 that the objective function that maximizes the vehicle's thrust efficiency produces the worst. The reasons for this can be uncovered by examining the equation that defines this objective function. In section 4.1.4 of Chapter 4 the vehicle's thrust efficiency for each mission segment is defined as follows:

$$\eta_i = \frac{(TV)_i}{\dot{m}_{fuel,i} LHV} \tag{4.7}$$

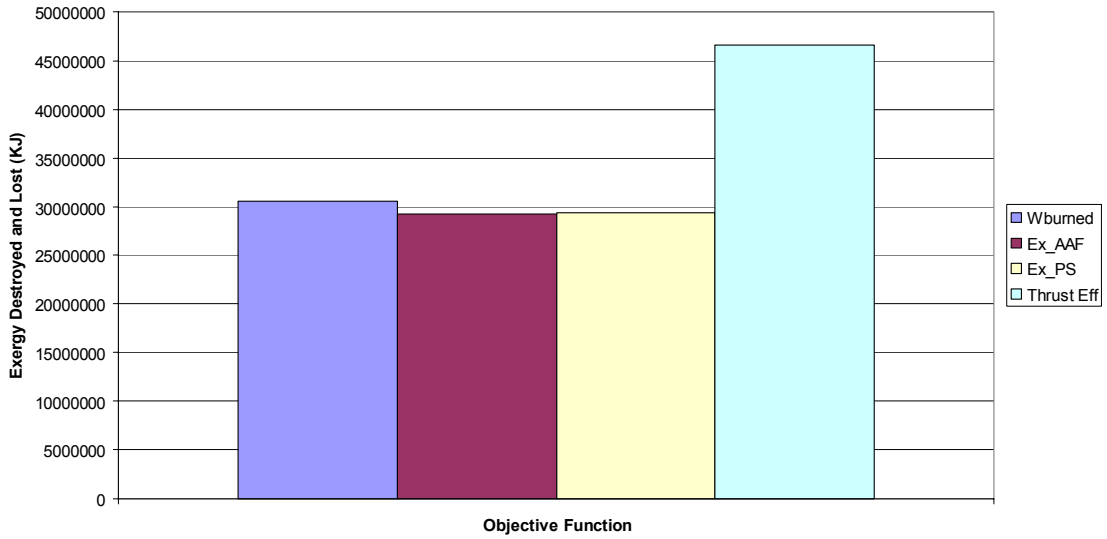

Figure 5.7: Total amount of exergy destroyed during the mission by each of the optimized syntheses/designs predicted by the different objective functions (fixed-wing case).

Obviously, in order to maximize the thrust efficiency value the optimization algorithm varies the values of decision variables to increase the values of the numerator of equation (4.7) and decrease the values denominator.

The numerator is the product of the vehicle's thrust and velocity. The latter is set by the demands and requirements of the mission and is, thus, not affected by the decision variables. The vehicle's thrust, on the other hand, is affected by two different aspects of the model: the change in kinetic and potential energies of the aircraft and the overall drag of the aircraft. As with the vehicle velocity, the change in the kinetic and potential energies of the aircraft is determined by the conditions of the mission and is, therefore, not affected by the decision variables. However, the aircraft's drag is a direct result of the synthesis/design and operational decision variables for the AFS-A.

As to the denominator of equation (4.7), it is a product of the fuel flow rate and the fuel's lower heating value, which is a constant. The fuel flow rate is a complex function of the vehicle's required thrust and the operational settings of the PS. The optimizer chooses decision variable values that increase the thrust by increasing the vehicle's drag in order to maximize the value of the numerator. The optimizer also chooses synthesis/design and operational decision variable values that minimize the fuel flow rate by creating a PS that operates at these higher thrust values. The result is that

the optimization creates a high drag aircraft with an oversized jet engine that consumes nearly all of its fuel during the mission, i.e. 3994 lbs of the 4000 lbs of fuel available. This objective, thus, does not prove to be a very useful one for optimizing the synthesis/design of the proposed morphing-wing AAF. These results are backed up by the fact that the synthesis/design and operational decision variable values produced by the optimization of the maximization of thrust efficiency objective for both the fixed- and morphing-wing AAFs were quite different from their counterparts produced by the other three objective functions as shown in Section 5.4 of this chapter.

The remaining three objective functions all result in much better syntheses/designs both for the morphing- and fixed-wing AAFs. For the objective functions that minimize the amount of fuel consumed and the amount of exergy destroyed and lost for the AAF during the mission, it can be seen that by inspecting the optimal synthesis/design and operational decision variable values presented in Tables 5.2 and 5.5, that the syntheses/designs produced for the fixed-wing AAF are very similar as are those for the morphing-wing AAF, especially with regards to the AFS-A. This, of course, is a reflection of the relative closeness in optimal values of fuel consumed (1.7% and 2.2% difference, respectively, for the fixed- and morning-wing cases) and the total amount of exergy destroyed and lost (6.6% and 4.5% difference, respectively, for the fixed- and morphing-wing cases) by both during the mission. For the morphing-wing case, the objective function that minimizes the amount of exergy destroyed and lost by the PS only posts a respectable synthesis/design, but is bested by the first two objective function syntheses/designs primarily because this last objective function contains no information of the exergy destroyed by the AFS-A via the induced and parasitic drags. In the case of the fixed-wing, the objective function that minimizes the amount of exergy destroyed and lost by the PS created an optimal synthesis/design that is much closer to those of the first two objective function syntheses/designs.

The objective function that minimizes the amount of exergy destroyed and lost in the PS only doesn't produce as good of a synthesis/design as objectives 1 and 2 because it lacks information of the exergy destroyed by the AFS-A. This deficiency is intensified when you include the operational variables of the morphing-wing AFS-A into the optimization because they provide an even greater ability to reduce the amount of exergy

destroyed by the AFS-A during flight. The AAF synthesis/design for the objective that minimizes the exergy destroyed and lost by the PS only for the fixed-wing case, thus, does not exhibit a significantly poorer synthesis/design as it does for the morphing-wing case.

The reason that the minimization of fuel consumption and the minimization of AAF exergy destruction and loss objective functions give nearly identical optimal synthesis/designs is because minimizing the later is thermodynamically equivalent to flying the mission using the least amount of fuel. Exergy destruction occurs in a system when thermodynamic irreversibilities occur within that system. In order for the system to overcome these irreversibilities, it must use additional exergy which for the AAF is only available from the fuel. In addition the exergy of the fuel that is unburned and expelled via the exhaust gases must be replaced with additional fuel. Thus, minimization of the AAF amount of exergy destroyed and lost by the aircraft in effect minimizes the amount of fuel consumed during the mission. However, the exergy minimization approach retains the advantage over that of fuel minimization in that the former has the means of easily distributing the internal losses associated with the minimization processes to each of the components in the system and, thus, a way of accurately pinpointing where the losses occur and why the optimization is able to arrive at the optimal synthesis/design that it does.

5.6 Further Comparison of the Optimized Morphing- and Fixed-Wing AAF Syntheses/Designs

A further comparison of the morphing-wing AAF to the fixed-wing AAF based on the minimization of fuel consumption and the minimization of AAF exergy destruction and loss are presented in Figures 5.8 and 5.9.

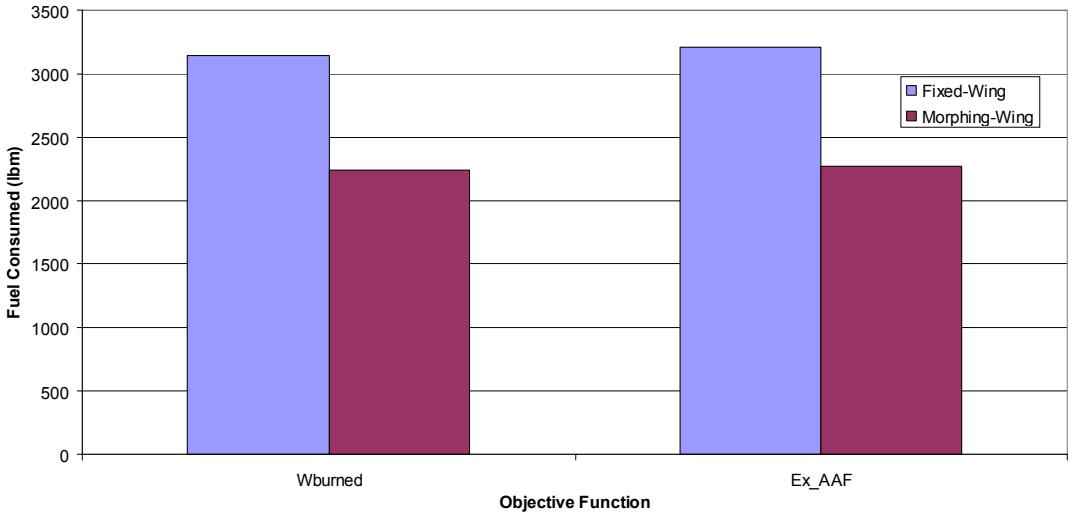

Figure 5.8: Comparison of the optimal fuel consumption results for the fixed-wing and morphing-wing models for two of the four objective functions used.

In order to make certain that the comparisons made are valid, the two aircraft models were held to the exact same synthesis/design process for both the PS and AFS-A and the same fixed designs and weights for all other subsystems (fuselage, cargo, fuel, payload, etc.).

The results presented in Figure 5.8 show a dramatic improvement in fuel consumption between the morphing- and fixed-wing cases for the two objective functions considered. The morphing-wing aircraft synthesis/design produced by the minimization of the fuel consumption objective function (Wburned) consumes 2235 lbm of fuel over the entire mission: a 29% savings over that for the fixed-wing aircraft synthesis/design, which consumes 3140 lbs of fuel. Likewise with respect to the minimization of the AAF exergy destruction objective function (Ex_AAF) the synthesis/design consumes 2274 lbm of fuel over the entire mission; also a 29% savings over the fixed-wing aircraft synthesis/design, which consumes 3210 lbm of fuel.

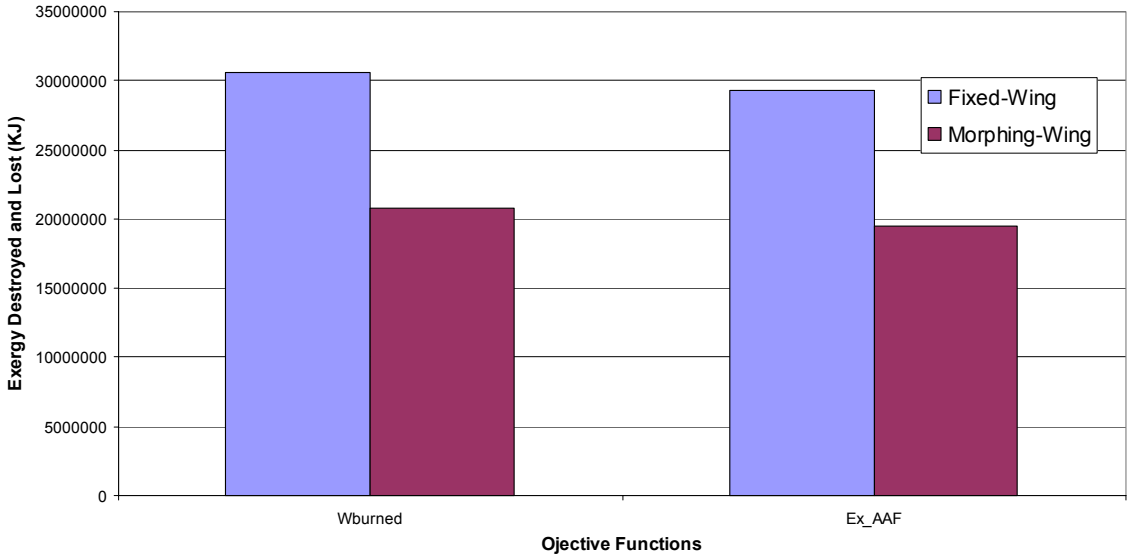

Figure 5.9: Comparison of the optimal exergy destruction results for the fixed-wing and morphing-wing models for two of the four objective functions used.

In a similar fashion, the results presented in Figure 5.9 also show a sizeable improvement in total exergy destroyed and lost between the morphing- and fixed-wing AAF syntheses/designs for the two objective functions considered. The morphing wing synthesis/design resulting from the Wburned objective destroys and looses 20.8 GJ of exergy over the entire mission: a 32% savings over the fixed-wing synthesis/design, which destroys and looses 30.6 GJ of exergy. The morphing-wing synthesis/design produced by resulting from the Ex_AAF objective destroys and looses 19.5 GJ of exergy: a 33.4% savings over the fixed-wing synthesis/design, which destroys and looses 29.3 GJ of exergy.

In order to better understand these savings, it is of interest to examine how different mission segments benefit from morphing the aircraft's wing during flight. This should show for which flight regimes morphing is the most advantageous. The amounts of fuel consumed and exergy destroyed and lost for each mission segment for the morphing- and fixed-wing aircraft synthesized/designed with the minimization of the fuel consumed objective function are displayed in Figures 5.10 and 5.11, respectively. The same general trends for fuel consumption and exergy destruction and loss with the morphing and fixed-wing models appear in each mission segment varying only in degree.

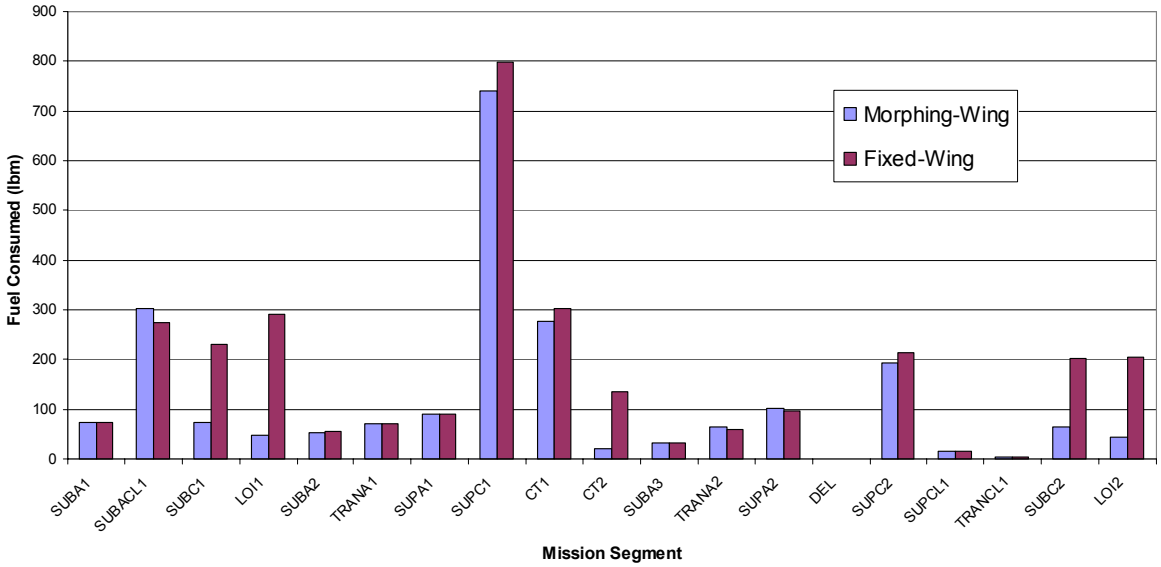

Figure 5.10: Fuel consumption breakdown for the optimal morphing-wing and fixed-wing aircraft syntheses/designs by mission segment.

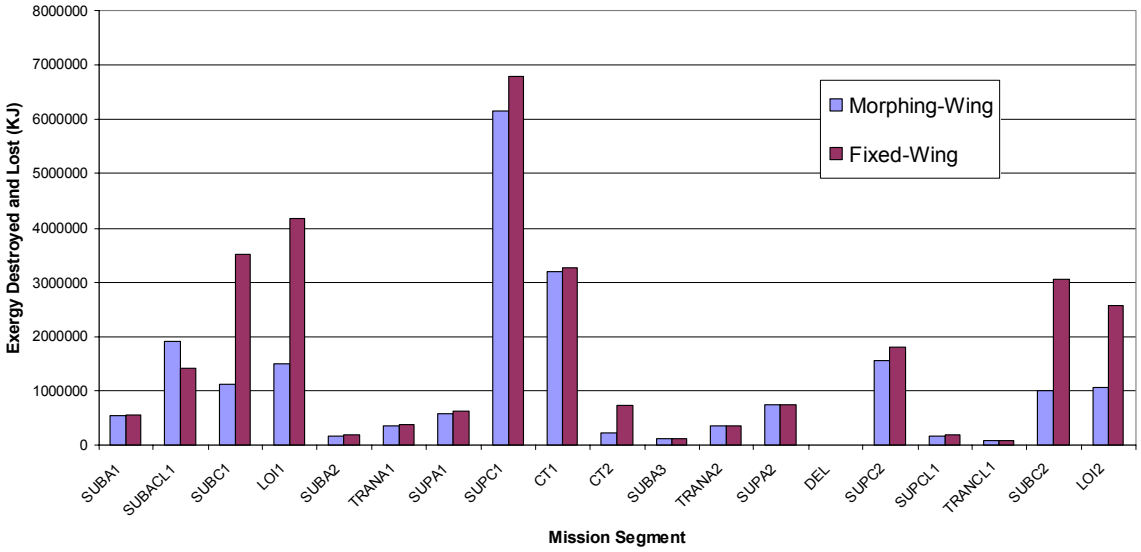

Figure 5.11: Exergy destruction and loss in the optimal morphing-wing and fixed-wing aircraft syntheses/designs by mission segment.

The morphing-wing aircraft shows tremendous gains over the fixed-wing synthesis/design in mission segments that are subsonic and require no changes in kinetic or potential energies such as the subsonic cruise (SUBC1,2), loiter (LOI1,2), and turn segments (CT2). The morphing-wing aircraft also boasts modest improvements over the fixed-wing aircraft in supersonic cruise segments (SUPC1,2). For all other segments the

morphing-wing aircraft shows little to no improvement over the fixed-wing aircraft in mission segments requiring acceleration or climb at either subsonic or supersonic speeds.

A typical fixed-wing aircraft is synthesized/designed to be able to accomplish the entire mission, which usually results in the aircraft being synthesized/designed so that it can accomplish the most constrained and demanding mission segments. For the mission used in this research, the most constrained and demanding mission segments are the segments that require acceleration, especially in the supersonic flight regime. The reason the morphing-wing aircraft shows little to no improvement over the most constrained mission segments is because the fixed-wing aircraft is optimally synthesized/designed to perform these mission segments. On the other hand, since the fixed-wing aircraft is synthesized/designed to fly the most constrained mission segments, it must fly the least constrained ones (cruise, loiter, etc.) with a less than optimal airframe configuration. In these less constrained mission segments, the morphing-wing aircraft shows the most improvement over the fixed-wing aircraft since during the mission, the morphing wing aircraft is able to adapt to a more optimal airframe configuration.

One of the most beneficial aspects of an exergy analysis is that it allows for quantitative assessment of thermodynamic irreversibilities (internal and external losses) that occur in the different subsystems and their components. This technique creates reliable basis for comparison between the losses of the different subsystems and components and shows where the most improvements could be made in order to improve the overall system by means of new technology or redesign. An exergy analysis on the different subsystem components for the optimal morphing-wing and fixed-wing aircraft syntheses/designs is presented in Figure 5.12. This exergy analysis shows which subsystem components and to what degree they contribute to the performance improvements that the morphing-wing synthesis/design provides.

In both the optimal morphing-wing and fixed-wing aircraft syntheses/designs, the majority of the exergy destruction for the AAF occurs in the combustor of the PS and due to the parasitic drag of the AFS-A. The large amount of exergy destruction in the combustion chamber is expected and is due to the large inherent thermodynamic losses involved in the transformation of chemical energy into heat and work energies during a combustion process. Furthermore, the large amount of exergy destroyed by parasitic

drag is also not surprising and is due to the high drag occurring in supersonic flight due to shock formation.

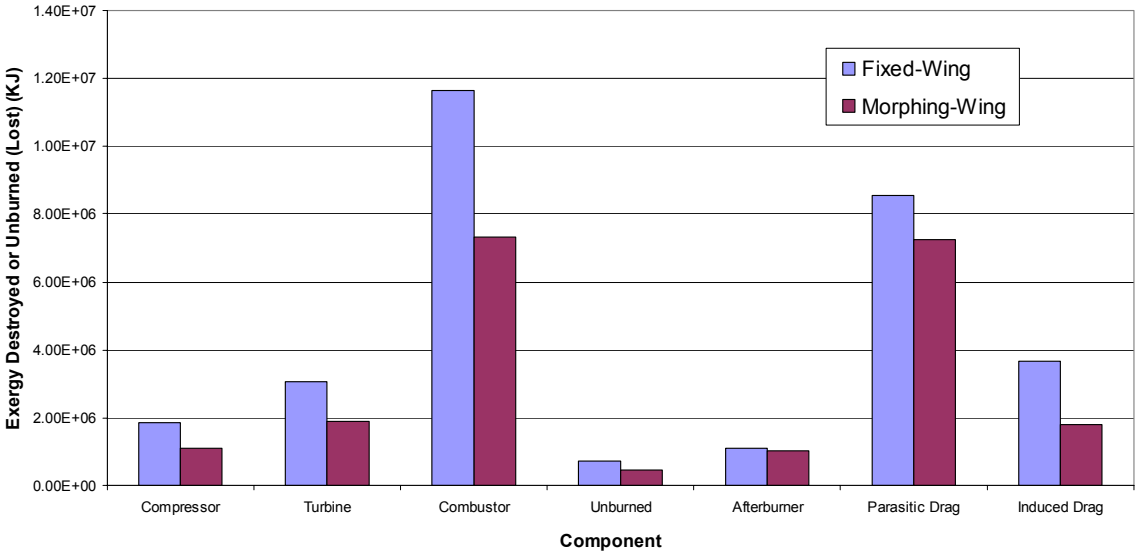

Figure 5.12: Exergy unburned and exergy destruction within each subsystem components for the optimal morphing-wing and fixed-wing syntheses/designs (case of the minimization of fuel consumed objective).

In general, the exergy analysis presented in Figure 5.12 shows component exergy and, thus, fuel savings across the board between the optimized fixed-wing and morphing-wing aircraft syntheses/designs. The amount of exergy destroyed by parasitic drag in the AFS-A drops from 8.53 GJ to 7.24 GJ between the fixed-wing and morphing wing designs: a savings of 15%. The amount of exergy destroyed by induced drag in the AFS-A is nearly cut in half, dropping from 3.56 GJ to 1.79 GJ: a 50% reduction. Overall, the morphing-wing design allows the AFS-A to reduce its exergy destruction over the mission by 25.3% due a reduction in vehicle drag.

The dramatic improvement in the morphing-wing synthesis/design results from the ability of the morphing-wing aircraft to change the shape of it's airframe during flight. This allows the morphing-wing aircraft to form a better overall aerodynamic shape during off-design flight conditions, which in turn reduces the amount of losses due to drag in the AFS-A (both parasitic and induced). A reduction in the drag losses in turn reduces the amount of thrust required to propel the aircraft, which allows the PS to operate at less demanding and exergy expensive settings. The final result is an overall reduction in the amount of exergy destroyed across all subsystems and components of the

optimized AAF. As seen in Figure 5.12 the components of the PS for the fixed-wing aircraft destroy and loose a total of 18.4 GJ of exergy, while those for the morphing-wing aircraft destroy and loose a total 11.8 GJ of exergy: a reduction of 35.9%.

5.7 Sensitivity Analysis of the Penalty Effects on the Optimal Morphing Wing Synthesis/Design

Since there is no reliable information available on the weights and energy consumption rates associated with the materials and actuation mechanisms involved with morphing an aircraft's wing, penalty factors are used instead in order to evaluate the effects of the additional weight and energy used by the morphing-wing aircraft. The optimal morphing-wing results presented in the previous sections assumed a 15% increase in wing weight and a 3% increase in fuel weight due to actuation. A sensitivity analysis is conducted on these penalties in order to determine to what extent the optimal morphing-wing aircraft synthesis/design holds its advantage over the optimal fixed-wing synthesis/design.

The fuel consumption results for the different wing and fuel weight penalties are presented in Figure 5.13. The figure is based on changing the optimal morphing-wing synthesis/design generated with the minimization of fuel consumption objective function to account for the increased penalties and then flying the modified synthesis/design over the entire mission. As denoted by the pink-shaded region in the figure, the optimal morphing-wing aircraft has a performance advantage in terms of fuel consumption over that for the optimal fixed-wing aircraft for broad range of wing and fuel weight penalty factors. Keeping the wing weight penalty fixed at 15%, the optimal morphing-wing aircraft boasts fuel savings even up to fuel weight penalties as high as 100%. At a constant fuel weight penalty of 3%, the optimal morphing-wing aircraft shows fuel savings even for wing weight penalties of up to 7 times the wing weight.

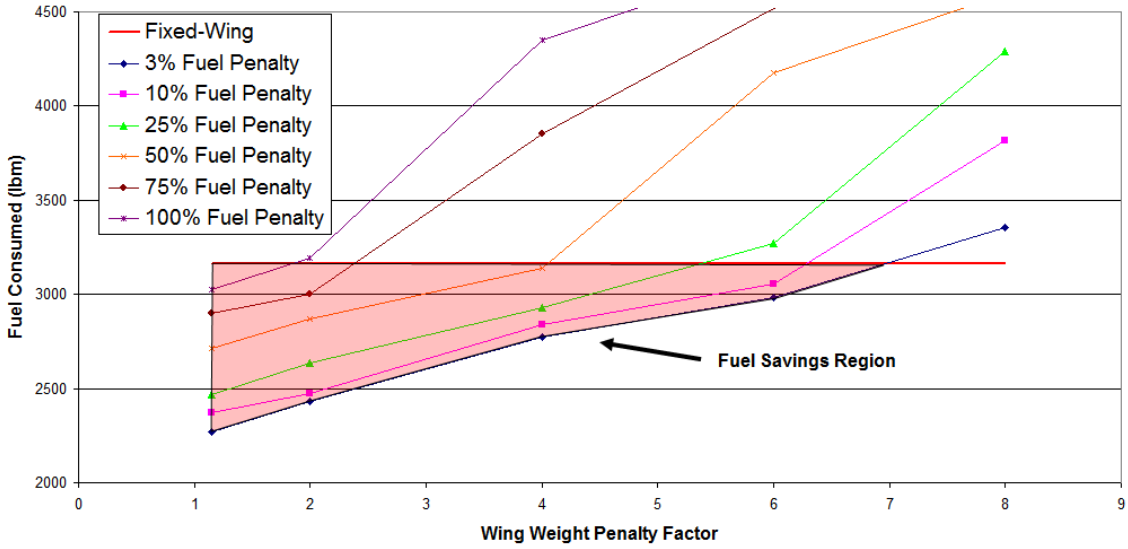

Figure 5.13: Sensitivity analysis of morphing-wing effectiveness for different actuator wing and fuel weight penalties. The analysis is based on the optimal synthesis/design found using the minimization of fuel consumption objective.

Thus, it can be concluded that the optimal morphing-wing aircraft synthesis/design is beneficial even when the wing and fuel weight penalties are at unrealistically high values.

Chapter 6

Conclusions

A number of conclusions can be drawn from the optimization runs performed on both the morphing-wing and fixed-wing aircraft models. The fuel consumption and exergy destruction analyses of the optimization runs discussed in Chapter 5 of this report present metrics by which the morphing- and fixed-wing aircraft performances can be compared and conclusions can be drawn. These conclusions are summarized as follow:

1. The morphing-wing aircraft model shows dramatic improvements in performance over the traditional fixed-wing aircraft by consuming about 29% less fuel and destroying about 32% less exergy over the same flight mission. Mission segment analysis shows that the bulk of the fuel and exergy savings due to the morphing-wing were actualized in the least constrained (subsonic) flight segments of the mission since the morphing-wing aircraft was able to create a more optimized synthesis/design at these flight conditions. Little to no performance benefits occurred with the morphing-wing aircraft during the most constrained flight segments (supersonic, maneuvering, etc.) since the fixed-wing aircraft is essentially optimally synthesized/designed for these mission segments. Therefore, a morphing wing aircraft proves most beneficial for missions with diverse flight conditions were different wing configurations are required to achieve optimal performance in every segment.
2. The morphing-wing and fixed-wing aircraft models were optimized using four different objective functions: the minimization of fuel consumed, the minimization of total exergy destroyed and lost, the minimization of the exergy destroyed and lost by the propulsion subsystem (PS) and the maximization of the thrust efficiency. Out of these four objective functions, the minimization of fuel

consumption and total amount of exergy destroyed and lost produced the best performance results from the optimization runs. This is due to the fact that both of these objective functions in essence are seeking to minimize the use of the highest quality energy present on board the aircraft, i.e., the fuel exergy.

3. The genetic algorithm (GA) optimization software used in this thesis work proved to have a number of benefits and drawbacks. The MOOLENI optimization software required no initial guesses for the synthesis/design and operational decision variables and was able to optimize the highly non-linear, multi-subsystem morphing-wing and fixed-wing fighter aircraft \ over the entire flight mission. However, long computational times, which are the nature of the GA optimization approach, occurred on all of the optimization runs that were performed (some runs took up to a week to converge). The long computational times were further complicated by the number of variables fed into the GA optimizer (the morphing-wing model had 160 decision variables) This suggests that more computational power would be needed in the future for GA optimizations of this nature, or perhaps a decomposition strategy (see, e.g., Rancruel and von Spakovsky (2003, 2005)) could be used instead. Additionally, re-optimizing the same problems did not exactly reproduce previous results. This particular problem could be eliminated if a combination of GA and gradient-based optimization software were used where the final solution of the GA software were fed to the gradient-based program as its initial solution point. This would allow the gradient-based method to hone in on the true global or near-global optimal solution.
4. The sources of the larges inefficiencies or thermodynamic losses are the combustor in the PS and the parasitic drag of the AFS-A. By being able to pinpoint the areas of high inefficiency, specific decision variables can be intelligently added or changed in order to attempt to reduce the inefficiencies in these particular components through re-optimizations. This is one of the main advantages of using an exergy-based analysis as opposed to the energy-based analysis which is not able to provide specific information on the location and severity of thermodynamic losses in the system.

5. A sensitivity analysis was conducted on the morphing-wing aircraft by varying the fuel and wing weight penalty factors and comparing the aircraft's performance to the standard fixed-wing aircraft. The results of the sensitivity analysis show that the morphing-wing aircraft outperformed the fixed-wing aircraft even with unreasonable penalty factors for the wing and fuel weights (7x the wing weight penalty and 2x the fuel weight penalty). This demonstrates that the morphing-wing can improve aircraft performance regardless of the penalties associated with the wing-morphing mechanisms and actuation.

References

[1] Anderson, J.D. Jr., 1999, *Aircraft Performance and Design*, WCB/McGraw-Hill, New York.

[2] Bejan, A., 1996, *Entropy Generation Minimization: The Method of Thermodynamic Optimization of Finite-Sized Systems and Finite-Time Processes*, CRC Press, Inc., Boca Raton, FL.

[3] Bowman, J., 2004, *An Examination of Morphing Sensitivities and Benefits for Subsonic Flight Speeds*, AFRL/VASA, WPAFB, OH.

[4] Bowman, J., 2003, "Affordability Comparison of Current and Adaptive and Multifunctional air Vehicle Systems" AIAA Paper 2003-1713.

[5] Bowman, J., Sanders, B., Weisshaar, T., 2002, "Evaluating the Impact of Morphing Technologies on Aircraft Performance", AIAA Paper 2002-1631.

[6] Brewer, K.M., 2006, *Exergy Methods for Mission-Level Analysis and Optimization of Generic Hypersonic Vehicle Concepts*, Department of Mechanical Engineering, Virginia Polytechnic Institute and State University, M.S. Thesis

[7] Camberos, J.A., Moorhouse, J.D., "Modeling Aerospace Vehicle Systems Based on Minimum Exergy Destruction", First International Conference on Grand Challenges for Modeling and Simulation, draft version.

[8] Figliola, R.S., Tipton, R., Li, H., "Exergy Approach to Decision-Based Design of Integrated Aircraft Thermal Systems", *Journal of Aircraft*, Vol. 40, No.1, January-February 2003.

[9] Figliola, R.S., Stewart, J., Nomura, S., Camberos, J.A., "An Exergy Based Methodology for Aircraft Systems Integration: Wing Aerodynamics Assessment", Summer Research Presentation at Air Force Research Laboratories, July 2004.

[10] Greene, G. C., "Viscous Induced Drag" AIAA Paper 1988-2550 Applied Aerodynamics Conference, 6th, Williamsburg, VA, June 6-8, 1988.

[11] Gyftopoulos, E. P., and Beretta, G. P., 1991, *Thermodynamics: Foundations and Applications*, Macmillan Publishing Co., New York.

[12] Joshi, S.P., Tidwell, Z., Crossley, W.A., Ramakrishnan, S., 2004, "Comparison of Morphing Wing Strategies Based Upon Aircraft Performance Impacts", AIAA Paper 2004-1722

[13] Kroo, I., "Drag Due to Lift: Concepts for Prediction and Reduction", *Annual Review of Fluid Mechanics*, 2001, 33:587-617.

[14] Leyland, G.B., 2002, *Multi-Objective Optimization Applied to Industrial Energy Problems*, Department of Mechanical Engineering, University of Auckland, M.S. Thesis.

[15] Markell, K. C., 2005, *Exergy Methods for the Generic Analysis and Optimization of Hypersonic Vehicle Concepts*, Department of Mechanical Engineering, Virginia Polytechnic Institute and State University, M.S. Thesis.

[16] Mattingly, Jack D., Heiser, William H., Pratt, David T., 2002, *Aircraft Engine Design*, AIAA Education Series, Washington, DC.

[17] Moorhouse, D.J., "Proposed System-Level Multidisciplinary Analysis Technique Based on Exergy Methods", *Journal of Aircraft*, Vol. 40, No.1, January-February 2003.

[18] Moorhouse, D.J., Sanders, B., von Spakovsky, M., Butt, J., "Benefits and Design Challenges of Adaptive Structures for Morphing Aircraft" International Forum on Aeroelasticity and Structural Dynamics, 28 June – 1 July 2005, Munich, Germany.

[19] Muñoz, J.R., von Spakovsky, M.R., 2001, "The Application of Decomposition to the Large Scale Synthesis/Design Optimization of Aircraft Energy Systems", *International Journal of Applied Thermodynamics*, June, vol. 4, no.2.

[20] Muñoz, J.R., von Spakovsky, M.R., 2001, "A Decomposition Approach for the Large Scale Synthesis/Design Optimization of Highly Coupled, Highly Dynamic Energy Systems", *International Journal of Applied Thermodynamics*, March, vol. 4, no. 1.

[21] Nicolai, Leland M., 1975, *Fundamentals of Aircraft Design*, School of Engineering, University of Dayton.

[22] Nikolic, V., Jumper, E., 2004, "Zero-Lift Wave Drag Calculation using Supersonic Area Rule and its Modifications" AIAA Paper 2004-217.

[23] Oyarzabal, B., Ellis, M. W., von Spakovsky, 2003, "Development of Thermodynamic and Economic Models for the Optimal Synthesis/Design of a PEM Fuel Cell Cogeneration System for Multi-Unit Residential Applications", *Journal of Energy Resources Technology*, ASME transactions, vol. 126, pp 21-29, March, N.Y., N.Y.

[24] Oyarzabal, B., von Spakovsky, Ellis, M. W., 2003, "Application of a Decomposition Strategy to the Optimal Synthesis/Design of a PEM Fuel Cell Cogeneration System for Multi-Unit Residential Applications", *Journal of Energy Resources Technology*, ASME transactions, vol. 126, pp 30-39, March, N.Y., N.Y.

[25] Periannan, V., 2005, *Investigation of the Effects of Different Objective Functions/Figures of Merit on the Analysis and Optimization of High Performance Aircraft System Synthesis/Design*, Department of Mechanical Engineering, Virginia Polytechnic Institute and State University, M.S. Thesis

[26] Rancruel, D. F., von Spakovsky, M. R., 2004, *Use of a Unique Decomposition Strategy for the Optimal Synthesis/Design and Operation of an Advanced Fighter Aircraft System,* 10th AIAA/ISSMO Multi- disciplinary Analysis and Optimization Conference, Aug. 30 - Sept. 1, Albany, New York.

[27] Rancruel, D. F., von Spakovsky, M. R., 2004, *A Decomposition Strategy based on Thermoeconomic Isolation Applied to the Optimal Synthesis/Design and Operation of an Advanced Tactical Aircraft System*, Efficiency, Costs, Optimization, Simulation and Environmental Aspects of Energy Systems (ECOS'04), Guanajuato, Mexico, ASME, July.

[28] Rancruel, D. F., von Spakovsky, M. R., 2003, "Decomposition with Thermoeconomic Isolation Applied to the Optimal Synthesis/Design of an Advanced Fighter Aircraft System, International Journal of Thermodynamics", ICAT, Istanbul, Turkey, September, vol. 6, no. 3.

[29] Rancruel, D. F., von Spakovsky, M. R., 2003, "A Decomposition Strategy Applied to the Optimal Synthesis/Design and Operation of an Advanced Figther Aircraft System: A Comparison with and without Airframe Degrees of Freedom", International Mechanical Engineering Congress and Exposition – IMECE'2003, ASME Paper No. 44402, N.Y., N.Y., November, accepted for publication.

[30] Rancruel, D. F., 2002, *A Decomposition Strategy Based on Thermoeconomic Isolation Applied to the Optimal Synthesis/Design and Operation of an Advanced Fighter Aircraft System*, Department of Mechanical Engineering, Virginia Polytechnic Institute and State University, M.S. Thesis.

[31] Rancruel, D., 2005, *Dynamic Synthesis/Design and Operation/Control Optimization Approach Applied to a Solid Oxide Fuel Cell based Auxiliary Power Unit under Transient Conditions*, Department of Mechanical Engineering, Virginia Polytechnic Institute and State University, Ph.D. Dissertation.

[32] Rancruel, D. F., von Spakovsky, M. R., 2005, "Development and Application of a Dynamic Decomposition Strategy for the Optimal Synthesis/Design and Operation/Control of a SOFC Based APU under Transient Conditions", International Mechanical Engineering Congress and Exposition – IMECE'2005, ASME Paper No. xxxxx, N.Y., N.Y., November, in preparation.

[33] Raymer, Daniel P., 1999, *Aircraft Design: A Conceptual Approach*, AIAA Education Series, Reston, VA.

[34] Riggins, D. 2003, The Thermodynamic Continuum of Jet Engine Performance: The Principle of Lost Work due to Irreversibility in Aerospace Systems, *International Journal of Thermodynamics*, ICAT, Istanbul Turkey, vol. 6, no. 3.

[35] Roth, Brian D., Crossley, William A., 2003, "Application of Optimization Techniques in the Conceptual Design of Morphing Aircraft" AIAA Paper 2003-6733

[36] Roth, B.A., Mavris, D.N., 2000, "A Method for Propulsion Technology Impact Evaluation via Thermodynamic Work Potential" AIAA Paper 2000-4854.

[37] Roth, B.A., 2001, "A Work Potential Perspective of Engine Component Performance", AIAA Paper 2001-3300.

[38] Roth, B.A., Mavris, D.N., "Generalized Model for Vehicle Thermodynamic Loss Management", *Journal of Aircraft*, Vol. 40, January-February 2003.

[39] Samoylovitch, O., Strelets, D., 2000, "Determination of the Oswald efficiency factor at the aeroplane design preliminary stage", *Aircraft Design*, Vol. 3, Issue 3.

[40] Saravanamuttoo, H.I.H., Rogers, G.F.C, Cohen, H., 2001, *Gas Turbine Theory*, Pearson Education Limited, Harlow, England.

[41] Young, T.M., "Fuel Sensitivity Analysis for Active Drag Reduction Systems", *The Aeronautical Journal*, Vol. 108, No. 1082, April 2004.

Vitae

Jeffrey Robert Butt was born one glorious day in Richmond, VA on January 26, 1980. As a graduate of Benedictine High School (Class of '98), he began his long and electrifying college career in August of 1998 at Virginia Polytechnic Institute and State University, aka, Virginia Tech. During his undergraduate studies at Virginia Tech, Jeffrey worked as a co-op engineer for the Tyvek Division of E.I. Dupont de Nemours in Richmond, VA where he spearheaded a new product development effort in anti-allergenic bedding that recently went to market in Asia. He graduated from Virginia Tech in May 2003 with a Bachelors of Science in Mechanical Engineering and ventured north to Baltimore, MD where he worked as a design engineer for RMF Engineering, a HVAC consultant firm. After a brief stint in industry, Jeffrey returned to Virginia Tech to pursue a Master's of Science in Mechanical Engineering and quickly realized that graduate school is very different from the undergraduate experience. During his graduate studies at Virginia Tech, he had the opportunity to work for the Air Force Research Laboratories at the Wright Patterson Air Force Base in Dayton, OH during two summer internships. Currently, Jeffrey has rejoined the American workforce as an employee of Deloitte and Touche, LLP in Washington, DC where he is a member of their technology integration service area of their federal government business consulting practice.